APPLIED COMPUTATIONAL ELECTROMAGNETICS SOCIETY JOURNAL

January 2018
Vol. 33 No. 1
ISSN 1054-4887

The ACES Journal is abstracted in INSPEC, in Engineering Index, DTIC, Science Citation Index Expanded, the Research Alert, and to Current Contents/Engineering, Computing & Technology.

The illustrations on the front cover have been obtained from the research groups at the Department of Electrical Engineering, The University of Mississippi.

EMERITUS ASSOCIATE EDITORS-IN-CHIEF

EMERITUS EDITORIAL ASSISTANTS

JANUARY 2018 REVIEWERS: REGULAR PAPERS

Ahmad Khedher Agha
Mousa Hussein
Mohamed Arbi Khlifi
Jean-Fu Kiang
Junqing Lan
Jean-Daniel Lan Sun Luk
Liang Lang
Chao Liu
Jen-Wei Liu
Jian Liu
Qiang Liu
Xiang Liu
Tian Hong Loh
Wang Long
Mahdi Moosazadeh
Andrea Morabito
Kingsford Obeng Kwakye
Bogdan-Loan Popa
Javad Pourahmadazar
Mohammd Pourbagher
Shishir Punjala
Lingyun Ren
Qiang Ren
Junwu Tao
Chang-Ying Wu
Xuan Hui Wu

JANUARY 2018 REVIEWERS: EXPRESS PAPERS

Saad Alhossin
William Coburn
Claudio Curcio
Francesco Dagostino
Vinh Dang
Ibrahim Elshafiey
Lars Foged
Claudio Gennarelli
Mang He
George Kyriacou
Ivor Morrow
Gokhan Mumcu
Quang Nguyen
Shinichiro Ohnuki
Vladimir Okhmatovski
Giuseppe Pelosi
Vince Rodriguez
Luca Salghetti Drioli
Nitin Saluja
Kubilay Sertel
Katherine Siakavara
Kagan Topalli
Georgios Trichopoulos
Christopher Trueman
Chao-Fu Wang

THE APPLIED COMPUTATIONAL ELECTROMAGNETICS SOCIETY JOURNAL

Vol. 33 No. 1 January 2018

TABLE OF CONTENTS – REGULAR PAPERS

TABLE OF CONTENTS – EXPRESS PAPERS

A Convolutional Perfectly Matched Layer (CPML) for the Fourth-Order One-Step Leapfrog HIE-FDTD Method

Mian Dong, Juan Chen, and Anxue Zhang

School of Electrical and Information Engineering
Xi'an Jiaotong University, Xi'an 710049, People's Republic of China
Chen.juan.0201@mail.xjtu.edu.cn

Abstract ─ A new convolutional perfectly matched layer (CPML) for the fourth-order one-step leapfrog hybrid implicit explicit finite-difference time-domain (HIE-FDTD) method for the TE case has been proposed in this paper. When the time step size satisfies with the time stability condition, the maximum reflection error of the proposed method is below -72dB, which demonstrates good absorbing performance of the CPML method. To verify the accuracy and efficiency of the proposed method, we compare the results of the traditional FDTD method and the HIE-FDTD method. Numerical examples demonstrate that the proposed method consumes about 60.13% less CPU time than the traditional FDTD method and 41.60% less CPU time than the existing HIE-FDTD method.

Index Terms ─ Accuracy, computational efficiency, convolutional perfectly matched layer (CPML), fourth order one-step leapfrog, hybrid implicit and explicit-FDTD (HIE-FDTD), relative reflection error.

I. INTRODUCTION

The finite-difference time-domain (FDTD) [1] method has been proven to be an effective means that provides accurate predictions of field behaviours for varieties of electromagnetic iteration problems. However, as it is based on an explicit finite-difference algorithm, the Courant-Friedrich-Levy (CFL) condition [2] must be satisfied when this method is used. In order to remove the CFL limit, many improved methods have been developed.

In 1999, the alternating direction implicit FDTD (ADI-FDTD) method was proposed in [3-5]. The time-step size in the ADI-FDTD technique was no longer constrained by the CFL limit and could be any value theoretically. However, the accuracy of the ADI-FDTD method is constrained by the numerical dispersion [6] and the splitting error associated with the square of the time step size [7-8]. Besides, it must solve six tridiagonal matrices and six explicit updates for one whole update cycle, which makes the ADI-FDTD method computationally inefficient. In 2005, a locally-one-dimension FDTD (LOD-FDTD) method was proposed in [9], [10]. The LOD-FDTD method requires less arithmetic operations than the ADI-FDTD method while providing comparable accuracy [10]. In 2006, a hybrid implicit and explicit-FDTD (HIE-FDTD) method was proposed in [11-14]. The time-step size of the HIE-FDTD method is determined by two space discretization. The HIE-FDTD method is weakly conditionally stable and is extremely useful for problems with very fine structures in one direction. Afterwards, a one-step leapfrog HIE-FDTD scheme has been proposed in [15] with its field updated in the same manner as that of the traditional FDTD method. Recently, a fourth-order leapfrog HIE-FDTD method was proposed in [16]. The method not only has the second-order accurate in time and the fourth-order accurate in space, but also has the one-step leapfrog schemes. Therefore, the method spend much less computational time and got better accuracy. However, up to now, such an efficient fourth-order one-step leapfrog HIE-FDTD method with absorbing boundary conditions (ABCs) hasn't been studied systematically.

In this paper a new convolutional perfectly matched layer (CPML) for the fourth-order one-step leapfrog HIE-FDTD method [17] is proposed. The time stability of the proposed method is $\Delta t = 6\Delta x/7c$ [18]. Numerical examples demonstrate that the proposed method has very high accuracy and efficiency. What's more, when the time step size satisfies with the time stability condition, the maximum reflection error of the proposed method is below -72dB, which demonstrates good absorbing performance of the CPML method. For simplicity, the two-dimensional (2-D) fourth-order one-step leapfrog HIE-CPML update equations are discussed in this paper. The formulations for a 3-D fourth-order HIE-FDTD method can be developed following a similar procedure.

The organization of this paper is as follows. In Section 2, the formulations of proposed algorithm are presented. The absorbing performance with CPML of proposed method is presented in Section 3. The numerical results applied to validate the efficiency and the accuracy of the proposed method, the traditional

Submitted On: February 18, 2017
Accepted On: August 12, 2017

FDTD method and the existing HIE-FDTD method are presented in Section 4.

II. FORMULATION

The numerical formulations of the two-dimensional fourth-order one-step leapfrog HIE-FDTD method proposed in [16] are presented as follows:

$$\begin{cases} E_{\mathrm{x}}^{n} = E_{\mathrm{x}}^{n-\frac{1}{2}} + \dfrac{\Delta t}{2\varepsilon}\delta_y H_z^{n-\frac{1}{2}} \\ E_{\mathrm{y}}^{n} = E_{\mathrm{y}}^{n-\frac{1}{2}} - \dfrac{\Delta t}{2\varepsilon}\delta_x H_z^{n-\frac{1}{2}} \\ H_z^{n} = H_z^{n-\frac{1}{2}} + \dfrac{\Delta t}{2\mu}\left(\delta_y E_x^{n-\frac{1}{2}} - \delta_x E_y^{n}\right) \end{cases}, \quad (1)$$

$$\begin{cases} E_{\mathrm{x}}^{n+\frac{1}{2}} = E_{\mathrm{x}}^{n} + \dfrac{\Delta t}{2\varepsilon}\delta_y H_z^{n+\frac{1}{2}} \\ E_{\mathrm{y}}^{n+\frac{1}{2}} = E_{y}^{n} - \dfrac{\Delta t}{2\varepsilon}\delta_x H_z^{n+\frac{1}{2}} \\ H_z^{n+\frac{1}{2}} = H_z^{n} + \dfrac{\Delta t}{2\mu}\left(\delta_y E_x^{n+\frac{1}{2}} - \delta_x E_y^{n}\right) \end{cases}, \quad (2)$$

$$\begin{cases} E_{\mathrm{x}}^{n+1} = E_{\mathrm{x}}^{n+\frac{1}{2}} + \dfrac{\Delta t}{2\varepsilon}\delta_y H_z^{n+\frac{1}{2}} \\ E_{\mathrm{y}}^{n+1} = E_{y}^{n+\frac{1}{2}} - \dfrac{\Delta t}{2\varepsilon}\delta_x H_z^{n+\frac{1}{2}} \\ H_z^{n+1} = H_z^{n+\frac{1}{2}} + \dfrac{\Delta t}{2\mu}\left(\delta_y E_x^{n+\frac{1}{2}} - \delta_x E_y^{n+1}\right) \end{cases}. \quad (3)$$

The CPML [18] is an efficient implementation of the complex frequency-shifted (CFS) constitutive PML parameters, originally proposed by Kuzuoglu and Mittra to introduce a strictly causal form of the PML. The modified Maxwell's equations in the CPML region can be written as [18-19]:

$$\begin{cases} \dfrac{\partial E_{\mathrm{x}}}{\partial t} = \dfrac{1}{\varepsilon}\left(\dfrac{1}{k_y}\dfrac{\partial H_z}{\partial y} + \psi_{exy}\right) \\ \dfrac{\partial E_{\mathrm{y}}}{\partial t} = \dfrac{1}{\varepsilon}\left(\dfrac{1}{k_x}\dfrac{\partial H_z}{\partial x} + \psi_{eyx}\right) \\ \dfrac{\partial H_z}{\partial t} = \dfrac{1}{\varepsilon}\left(\dfrac{1}{k_y}\dfrac{\partial E_x}{\partial y} - \dfrac{1}{k_x}\dfrac{\partial E_y}{\partial X} + \psi_{hzy} - \psi_{hzx}\right) \end{cases}, \quad (4)$$

where ψ is the auxiliary term related to the field quantities in the CPML, and k_x, k_y are nonnegative real numbers, respectively.

Here,

$$\psi_{\mathrm{exy}}^{n+1/2} = b_y\psi_{\mathrm{exy}}^{n-1/2} + a_y\delta_y H_z^{n+1/2},$$
$$\psi_{\mathrm{eyx}}^{n+1/2} = b_x\psi_{\mathrm{eyx}}^{n-1/2} + a_x\delta_x H_z^{n+1/2},$$
$$\psi_{\mathrm{hzy}}^{n+1} = b_y\psi_{\mathrm{hzy}}^{n+1} + a_y\delta_y E_x^{n},$$
$$\psi_{\mathrm{hzx}}^{n+1} = b_x\psi_{\mathrm{hzx}}^{n+1} + a_x\delta_x E_y^{n},$$

$$b_\xi = e^{-\left(\frac{\sigma_\xi}{k_\xi}+\alpha\right)\left(\frac{\Delta t}{\xi}\right)},\ a_\xi = \frac{\sigma_\xi}{\sigma_\xi k_\xi + k_\xi^2\alpha}\left(b_\xi - 1\right),$$

$$\sigma_\xi = \frac{\sigma_{\max}\left|\xi-\xi_0\right|^m}{d^m},\ \sigma_{\max} = \left(m+1\right)\Big/\left(150\pi\Delta_\xi\right),$$

$$k_\xi = 1+\left(k_{\max}-1\right)\frac{\left|\xi-\xi_0\right|^m}{d^m},\ \xi=\mathrm{x,y}.$$

Here α and a_ξ are assumed to be nonnegative real number and ξ_0 is the position of the CPML layer. d and $\sigma_{\max}$ are the thickness of the CPML in x and y directions and the maximum conductivity, respectively. m and Δ_ξ are the cell size and the order of polynomial scaling, respectively. For these simulations, the value of m is chosen as 4.

By applying the CPML layer to (1)-(3), a set of time marching equations is derived and expressed as follows:

$$E_{\mathrm{x}}^{n} = E_{\mathrm{x}}^{n-\frac{1}{2}} + \frac{\Delta t}{2\varepsilon}\left\{\frac{\delta_y}{k_y}H_z^{n-\frac{1}{2}} + \psi_{exy}^{n-\frac{1}{2}}\right\}, \quad (5\text{-}1)$$

$$E_{\mathrm{y}}^{n} = E_{\mathrm{y}}^{n-\frac{1}{2}} - \frac{\Delta t}{2\varepsilon}\left\{\frac{\delta_x}{k_x}H_z^{n-\frac{1}{2}} + \psi_{eyx}^{n-\frac{1}{2}}\right\}, \quad (5\text{-}2)$$

$$H_z^{n} = H_z^{n-\frac{1}{2}} - \frac{\Delta t}{2\mu}\left\{\frac{\delta_y}{k_y}E_x^{n-\frac{1}{2}} - \frac{\delta_x}{k_x}E_y^{n-\frac{1}{2}} + \psi_{hzy}^{n-\frac{1}{2}} - \psi_{hzx}^{n}\right\}, \quad (5\text{-}3)$$

$$E_{\mathrm{x}}^{n+\frac{1}{2}} = E_{\mathrm{x}}^{n} - \frac{\Delta t}{2\varepsilon}\left\{\frac{\delta_y}{k_y}H_z^{n+\frac{1}{2}} + \psi_{exy}^{n+\frac{1}{2}}\right\}, \quad (6\text{-}1)$$

$$E_{\mathrm{y}}^{n+\frac{1}{2}} = E_{\mathrm{y}}^{n} - \frac{\Delta t}{2\varepsilon}\left\{\frac{\delta_x}{k_x}H_z^{n+\frac{1}{2}} + \psi_{eyx}^{n+\frac{1}{2}}\right\}, \quad (6\text{-}2)$$

$$H_z^{n+\frac{1}{2}} = H_z^{n} - \frac{\Delta t}{2\mu}\left\{\frac{\delta_y}{k_y}E_x^{n+\frac{1}{2}} - \frac{\delta_x}{k_x}E_y^{n} + \psi_{hzy}^{n+\frac{1}{2}} - \psi_{hzx}^{n}\right\}, \quad (6\text{-}3)$$

$$E_{\mathrm{x}}^{n+1} = E_{\mathrm{x}}^{n+\frac{1}{2}} + \frac{\Delta t}{2\varepsilon}\left\{\frac{\delta_y}{k_y}H_z^{n+\frac{1}{2}} + \psi_{exy}^{n+\frac{1}{2}}\right\}, \quad (7\text{-}1)$$

$$E_{\mathrm{y}}^{n+1} = E_{\mathrm{y}}^{n+\frac{1}{2}} - \frac{\Delta t}{2\varepsilon}\left\{\frac{\delta_x}{k_x}H_z^{n+\frac{1}{2}} + \psi_{eyx}^{n+\frac{1}{2}}\right\}, \quad (7\text{-}2)$$

$$H_z^{n+1} = H_z^{n} - \frac{\Delta t}{2\mu}\left\{\frac{\delta_y}{k_y}E_x^{n+\frac{1}{2}} - \frac{\delta_x}{k_x}E_y^{n} + \psi_{hzy}^{n+\frac{1}{2}} - \psi_{hzx}^{n}\right\}. \quad (7\text{-}3)$$

Substituting (5-3) into (5-1), we have:

$$E_{\mathrm{x}}^{n} = \left(1-\frac{\Delta t^2\delta_y^2}{4\varepsilon\mu k_y^2}\right)E_{\mathrm{x}}^{n-\frac{1}{2}} + \frac{\Delta t^2}{4\varepsilon\mu}\frac{\delta_x\delta_y}{k_x k_y}E_{\mathrm{y}}^{n} + \frac{\Delta t^2\delta_y}{4\varepsilon\mu k_y}\left(\psi_{hzx}^{n} - \psi_{hzy}^{n-\frac{1}{2}}\right) + \frac{\Delta t}{2\varepsilon}\left(\frac{\delta_y}{k_y}H_z^{n} + \psi_{exy}^{n-\frac{1}{2}}\right). \quad (8)$$

By substituting (6-3) and (8) into (6-1), the updating equation for E_x^n is obtained as follows:

$$\left(1-\frac{\Delta t^2\delta_y^2}{4\varepsilon\mu k_y^2}\right)\left(E_x^{n+\frac{1}{2}}-E_x^{n-\frac{1}{2}}\right) = \frac{\Delta t\delta_y}{2\varepsilon k_y}H_z^n+\frac{\Delta t}{2\varepsilon}\left(\psi_{exy}^{n+\frac{1}{2}}+\psi_{exy}^{n-\frac{1}{2}}\right). \quad (9)$$

In Eq. (9), it often uses the finite difference to approximate the spatial derivate [20], [21]. For example:

$$\left.\frac{\partial f(x,y,t)}{\partial x}\right|_{x=i\Delta x}^{n+\frac{1}{2}} \approx \frac{1}{\Delta x}\sum_{h=0}^{H-1}\alpha(h)\left[f\left|_{i+h+\frac{1}{2},j}^{n+\frac{1}{2}}-f\right|_{i-h-\frac{1}{2},j}^{n+\frac{1}{2}}\right], \quad (10)$$

where $\alpha(h)$ can be obtained as follows [22]:

$$\alpha(h)=\frac{(-1)^h}{2\left(h+\frac{1}{h}\right)^2}\frac{\left((2H\text{-}1)!!\right)^2}{(2H\text{-}2\text{-}2h)!!(2H+2h)!!}.$$

When H is equal to 2, the order of the algorithm is equal to 4. According to the definition of the constant $\alpha(h)$ and by substituting (10) into (9), then introducing the auxiliary variable *e* and *h* as indicated in [23], i.e.,

$$e_m^{n+1/2}=E_m^{n+1/2}\text{-}E_m^{n-1/2} \quad \ldots \text{m=x, y},$$
$$e_m^{n+1}=H_m^{n+1}\text{-}H_m^n \quad \ldots \text{m=x, y}.$$

The final updating equations of $E_x^{n+1/2}$ of the proposed method can be finally obtained as follows,

$$\begin{aligned} &c_1 e_x\left|_{i+1/2,j}^{n+1/2}-c_2\left(e_x\right|_{i+1/2,j+1}^{n+1/2}-e_x\left|_{i+1/2,j-1}^{n+1/2}\right.\right)\\ &-c_3\left(e_x\left|_{i+1/2,j+2}^{n+1/2}-e_x\right|_{i+1/2,j-2}^{n+1/2}\right)\\ &-c_4\left(e_x\left|_{i+1/2,j+3}^{n+1/2}-e_x\right|_{i+1/2,j-3}^{n+1/2}\right)\\ &=c_5\left(H_z\left|_{i+1/2,j+1/2}^{n}-H_z\right|_{i+1/2,j-1/2}^{n}\right)\\ &-c_6\left(H_z\left|_{i+1/2,j+\frac{3}{2}}^{n}-H_z\right|_{i+1/2,j-3/2}^{n}\right)\\ &+c_7\left(\psi_{exy}\left|_{i+1/2,j}^{n+1/2}-\psi_{exy}\right|_{i+1/2,j}^{n-1/2}\right) \end{aligned} \quad (11)$$

where

$$c_1=\frac{365\Delta t^2}{576\varepsilon\mu\Delta y^2},\ c_2=\frac{87\Delta t^2}{256\varepsilon\mu\Delta y^2},$$
$$c_3=\frac{3\Delta t^2}{128\varepsilon\mu\Delta y^2},\ c_4=\frac{\Delta t^2}{2304\varepsilon\mu\Delta y^2},$$
$$c_5=\frac{9\Delta t}{8\varepsilon\mu\Delta y},\ c_6=\frac{\Delta t}{24\varepsilon\mu\Delta y},\ c_7=\frac{\Delta t}{2\varepsilon}.$$

The other updating equations of the proposed method can be obtained similarly and are not shown here for simplicity.

III. ABSORBING PERFORMANCE

In order to study the absorbing performance of the CPML absorbing boundary, the relative reflection error of the fourth-order one-step leapfrog HIE-CPML method is discussed. A simulation of sinusoidally modulated Gaussian pulse as an input electric current profile is studied. The time dependence of the excitation function is as follows:

$$s(t)=\exp\left(-\frac{(t-t_0)^2}{\tau^2}\right)\sin\left(2\pi f_0(t-t_0)\right), \quad (12)$$

where f_0, t_0 and τ are constants. Here, we choose $f_0=5GHz$, and $t_0=\tau=6\times10^{-10}s$. This excitation source is used throughout the paper A 3.0GHz i5 professor PC with 8GHz memory is used to calculate the results. A In the all simulation, the relative reflection error is defined as follows:

$$E_{rror}=20\log_{10}\left|\frac{E_y(t)-E_{y,ref}(t)}{E_y(t)}\right|. \quad (13)$$

where $E_y(t)$ is the time-dependent electric field at the observation point calculated by using the proposed method truncated by the CPML. $E_{y,ref}(t)$ represents the reference electric field and is measured at the same observation point by extending the dimensions of the computation domain to 500×500 grids so that the reflected wave does not return at the observation point before the simulation was not terminated. It can almost avoid any possible reflection effect from boundaries. The CPML constructive parameters for these simulations are $k_{\max}=12$, $\alpha=0.07$ [24].

The relation between the relative reflection errors of the proposed method and the variable α is presented in Fig.1. The spatial step sizes in this simulation are $\Delta_x=0.006$ and $\Delta_y=0.0006$. The time step size of the proposed method is $\Delta t=6\Delta x/7c=17.14ps$. It can be seen from the Fig. 1 that the proposed method with CPML absorbing boundary has different relative reflection errors as α takes different values. When the value of α is larger than 0.07, the maximum relative reflection error is less than -72dB. However, when the value of α is less than 0.07, the relative errors deteriorate so that the maximum relative reflection error would reach to -51dB. Therefore, the optimal value of α is equal to 0.07. With this value, the relative reflection error of the HIE-FDTD method is below -72.52dB in the entire simulation history.

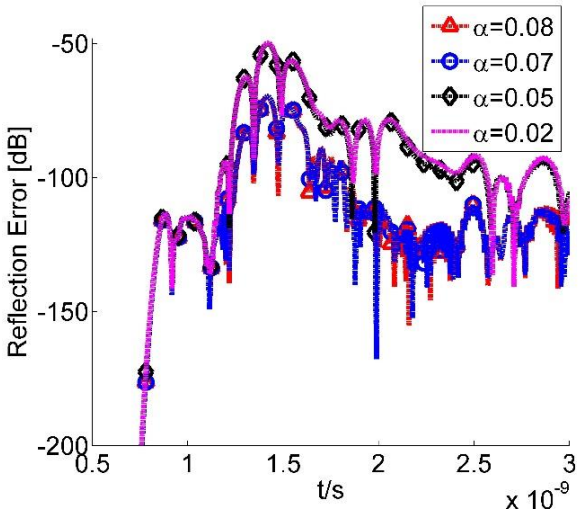

Fig. 1. The relation between the relative reflection errors and the order of the polynomial α.

In order to present relations between the relative reflection error and the time step size of the proposed method, the variation of the relative reflection error with respect to different CFLN values is presented in Fig. 2. Here, the value of the α is equal to 0.07. Figure 2 shows that as the increase of the CFLN, the relative reflection error of the proposed method increases gradually. Even when CFLN takes its maximum value, namely, CFLN=8.657, the relative reflection error still can reach to -51.45dB, which shows excellent absorbing performance of the CPML.

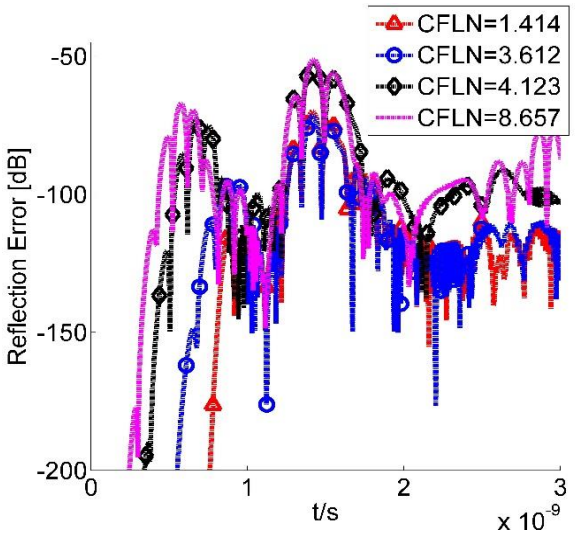

Fig. 2. The relation between the relative reflection errors and the CFLN value.

Next, it is instructive to observe the relation between the maximum reflection error and the CPML constructive parameters $k_{\max}$, $\sigma_{\max}$. Figure 3 illustrates the contour curves of the maximum relative reflection error against $k_{\max}$, $\sigma_{\max}$ at the observation point. It is demonstrated from the Fig. 3 that the best absorbing performance can be achieved in a larger range by selected the values of $k_{\max}$ and $\sigma_{\max}$ effectively. That makes it easy to predict the optimal values. Obviously, when $k_{\max}=12$ and $\sigma_{\max}=\sigma_{opt}=1$, the maximum errors of the proposed method can reach to -72dB.

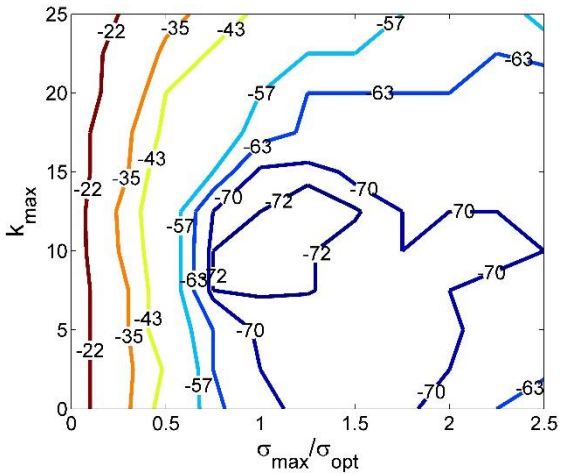

Fig. 3. The maximum relative reflection error at observation point as a function.

IV. ACCURACY AND EFFICIENCY

To validate the accuracy and efficiency of presented algorithm, a simulation of sinusoidally modulated Gaussian pulse as an input electric current profile is studied. A 2-D computational domain with the dimension $84cm\times 8.4cm$ is shown in Fig. 4. The computational domain is free space and is discretized with $\Delta_x = 0.006$ and $\Delta_y = 0.0006$ respectively. The total lattice dimension is 140×140. The current source is placed at the centre of the domain and the observation point $p1$ is placed 30cm away from the source. Ten cell-thick CPML layers are used to terminate the computational domain [23].

Applied the traditional FDTD method, the HIE-FDTD method [24-25] and the proposed method to compute the field components at the observation point, the results are shown in Fig. 5. The time-step sizes in the three methods are $\Delta t = 1\Big/\left(c\sqrt{1/\Delta x^2+1/\Delta y^2}\right)=1.99\,ps$, $\Delta t = 1\Big/\left(c\sqrt{1/\Delta x^2}\right)=20.10\,ps$ and $\Delta t = 6\Delta x/7c = 17.14\,ps$, respectively. They are the maximum time-step size of each method to satisfy the time stability condition. It can be seen from the Fig. 5 that the component calculated by

using the proposed method agrees very well with the results calculated by using the traditional FDTD method and the HIE-FDTD method, which demonstrates the proposed method has a high accuracy.

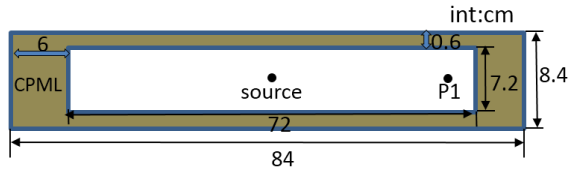

Fig. 4. Free space truncated by CPML.

In order to study the efficiency of the proposed method, more simulations are presented here. The time-step size of the traditional FDTD method is chosen as $\Delta t = 1.990\,ps$. In the HIE-FDTD method, they are chosen as $\Delta t = 1.99, 3.98, 7.96, 17.14\,ps$ and in the proposed method, they are also $\Delta t = 1.99, 3.98, 7.96, 17.14\,ps$. To complete these simulations, the computational times of these methods are presented in Table 1. The numbers of the computational iterations of each method are also presented in the Table 1.

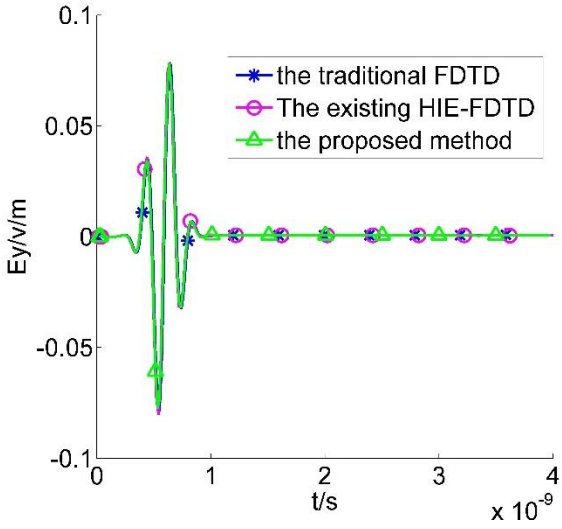

Fig. 5. The electric field values at $p1$ calculated by the FDTD algorithm, the existing HIE-FDTD algorithm and the proposed HIE-FDTD algorithm.

Table 1: Computer costs of the FDTD algorithm, the HIE-FDTD algorithm and the proposed method

Δt (ps)		1.99=1.99*1	3.98=1.99*2	7.96=1.99*4	17.14=1.99*8.6
CFLN		1	2	4	8.6
The traditional FDTD	Number of iterations	2000			
	CPU time (s)	29.1			
The HIE-FDTD	Number of iterations	2000	1000	500	232
	CPU time (s)	171.0	84.9	42.7	19.8
The proposed method	Number of iterations	2000	1000	500	232
	CPU time (s)	101.3	50.2	25.1	11.6

As shown in Table 1, when CFLN is 8.6, the proposed method consumes about 60.13% less CPU time than the traditional FDTD method. The main reason is as follows: the time-step size of the proposed method is 8.6 times larger than that of the traditional FDTD method. Therefore, the iteration number is much smaller for the same simulated time history. Besides, compared with the HIE-FDTD method, the proposed method saves about 41.60% CPU time, although the time step size in these two methods are same. This is because the formulation of the proposed method is much conciser than the HIE-FDTD method. It means even the proposed method uses same time-step size as the HIE-FDTD method, its computational time considerably reduced compared with that of the HIE-FDTD method. Note that if CFLN=1 is used, the proposed method would have no advantages over the traditional FDTD method. As the computational time of each iteration is longer because of additional efforts needed for solving the tri-diagonal linear system in proposed method.

VI. CONCLUSION

This paper introduces the CPML absorbing boundary conditions theories into the fourth-order one-step leapfrog HIE-FDTD algorithm. It is found that the technique is weakly conditionally stable and supports time step size greater than the CFL limit. Numerical simulations show that the maximum reflection error as low as -72 dB can be achieved by selecting $k_{\max} = 12$ and $\sigma_{\max}/\sigma_{opt} = 1.0$. It demonstrates the proposed method with CPML has good absorbing performance. Besides, the field components calculated by using the proposed method agree very well with the result calculated by using the traditional FDTD method and the HIE-FDTD method, which indicates that the proposed method has excellent calculation accuracy and low computational error. What's more, the computer cost of the proposed algorithm is much less than the traditional FDTD algorithm and the HIE-FDTD method. It means the proposed algorithm has higher efficiency.

ACKNOWLEDGMENT

This work was supported by National Natural Science Foundations of China (No. 61231003, 61601360, 61501365 and 61471292), and also supported by the Fundamental Research Funds for the Central Universities.

REFERENCE

[1] K. S. Yee, "Numerical solution of initial boundary value problems involving Maxwell's equations in isotropic media," *IEEE Transactions on Antennas Propagation*, vol. 14, pp. 302-307, 1996.

[2] A. Taflove, *Computational Electrodynamics*. Norwood,MA: Artech House, 1995.

[3] T. Namiki, "A new FDTD algorithm based on alternating-direction implitcit method," *IEEE Trans. Microwave Theory Tech*., vol. 47, pp. 2003-2007, 1999.

[4] Q.-X. Chu, L.-N. Wang, and Z.-H. Chen, "A novel numerical dispersion formulation of the 2D ADI-FDTD method," *International Journal of RF and Microwave Computer-Aided Engineering*, vol. 16, no. 6, pp. 584-587, 2006

[5] X.-T. Zhao, Z.-G. Wang, and X.-K. Ma, "A 3-D unconditionally stable precise integration time domain method for the numerical solutions of Maxwell's equations in circular cylindrical coordinates," *International Journal of RF and Microwave Computer-Aided Engineering*, vol. 19, no. 2, pp. 230-242, 2009.

[6] H. X. Zheng and K. W. Leung, "An efficient method to reduce the numerical dispersion in the ADI-FDTD," *IEEE Trans. Microwave Theory Tech*., vol. 53, pp. 2295-2301, 2005.

[7] S. Wang and C. W. Trueman, "An iterative ADI-FDTD with reduced splitting error," *IEEE Microw. Compon. Lett*., vol. 15, pp. 92-94, 2005.

[8] J. Chen and J. Wang, "Error between unconditionally stable FDTD methods and conventional FDTD method," *Electron. Lett*., vol. 42, pp. 1132-1133, 2006.

[9] V. E. Nascimento, F. L.Teixeira, and B. H. V. Borges, "Uncondtionally stable finite-difference time-domain method based on the locally-one-dimensional technique," *Proc. 22nd Symp. Brasileiro Telecomun*., vol. 9, pp. 288-291, 2005.

[10] J. Shibayama, M. Muraki, J. Yamauchi, et al., "Efficient implicit FDTD algorithm based on locally one-dimensional scheme," *Electron. Lett*., vol. 41, pp. 1046-1047, 2005.

[11] B. Huang and G. Wang, "A hybrid implicit-explicit FDTD scheme with weakly conditional stability," *Microwave Opt. Technol. Lett*., vol. 39, pp. 97-101, 2003.

[12] J. Chen and J. Wang, "A 3-D hybrid implicit-explicit FDTD scheme with weakly conditional stability," *Microwave Opt. Technol. Lett.*, vol. 48, pp. 2291-2294, 2006.

[13] J. Chen and J. G. Wang, "A three-dimensional semi-implicit FDTD scheme for calculation of shielding effectiveness of enclosure with thin slots," *IEEE Transactions on Electromagnetic Compatibility*, vol. 49, pp. 354-360, 2007.

[14] J. Chen and J. G. Wang, "Numerical simulation using HIE–FDTD method to estimate various antennas with fine scale structures," *IEEE Transactions on Antennas Propagation*, vol. 55, pp. 3603-3612, 2007.

[15] J. Wang, B. Zhou, L. Shi, C. Gao, et al., "A novel 3-D HIE-FDTD method with one-step leapfrog scheme," *IEEE Trans. Microw. Theory Tech*., vol. 62, pp. 1275-1283, 2014.

[16] M. Dong, A. Zhang, and J. Chen, "The fourth order one-step leapfrog HIE-FDTD method," *Applied Computational Electromagnetics Society Journal*, vol. 31, pp.1370-1376, 2016.

[17] D.-W. Zhu, Y.-G. Wang, and H.-L. Chen, "A one-step leapfrog HIE-FDTD method for rotationally symmetric structures," *International Journal of RF and Microwave Computer-Aided Engineering*, 2016.

[18] J. A. Roden and S. D. Gedney, "Convolutional PML (CPML): An efficient FDTD implementation of the CFS-PML for arbitrary media," *Microw. Opt. Technol. Lett*., vol. 27, pp. 334-339, 2002.

[19] M. Krumpholz and L. P. B. Katehi, "MRTD: New time-domain schems based on multiresolution analysis," *IEEE Trans. Microwave Theory Tech*., vol. 44, pp. 555-571, 1996.

[20] M. L. Ghrist, "High order difference methods for wave equations," *University of Colorado*, 1997.

[21] S. C. Yang, Z. Chen, Y. Yu, et al., "The unconditionally stable one-step leapfrog ADI-FDTD method and its comparisons with other FDTD methods," *IEEE Microw. Wireless Compon. Lett*., vol. 21, pp. 640-642, 2011.

[22] S. D. Gedney, "The perfectly matched layer absorbing medium," Advances in Computational Electrodynamics: The Finite Difference Time Domain, A. Taflove (Editor), Artech House, Boston, MA, pp. 263-340, 1998.

[23] J. Wang, Y. Wang, and D. Zhang, "Truncation of open boundaries of cylindrical waveguides in 2.5-dimensional problems by using the convolutional perfectly matched layer," *IEEE Trans. Plasma Sci*., vol. 34, pp. 681-690, 2006.

[24] J. Chen, N. Xu, and A. Zhang, "Using dispersion HIE-FDTD method to simulate the graphene-based polarizer," *IEEE Transaction on Antennas and Propagation*, vol. 24, pp. 3011-3017, 2016.

[25] J. Chen and J. Wang, "Three-dimensional dispersive hybrid implicit-explicit finite-difference time-domain method for simulations of graphene," *Computer Physics Communications*, vol. 207, pp. 211-216, 2016.

FDTD Evaluation of LEMP Considering the Lossy Dispersive Ground

Zheng Sun, Lihua Shi*, Yinghui Zhou, Bo Yang, and Wenwen Jiang

National Key Laboratory on Electromagnetic Environmental Effects and Electro-optical Engineering
PLA Army Engineering University, Nanjing, 210007, China
shilih@tom.com*

Abstract ─ An accurate evaluation of lightning electromagnetic pulse (LEMP) using the finite-difference time-domain (FDTD) method in 2-D cylindrical coordinates is studied, which takes the soil dispersion into account. The parameters of engineering soil models are reformed by the vector-fitting (VF) scheme, for an efficient handling in FDTD. The FDTD updating equations for the dispersive soil are developed with the semi-analytical recursive convolution (SARC) algorithm. The cylindrical CPML is also developed for truncating the dispersive soil. The efficiency of the proposed method is validated by comparing the numerical results with the Cooray-Rubinstein (CR) approximation. The proposed method provides an accurate FDTD evaluation of LEMP considering the soil dispersion and can be further incorporated into the simulations of more complicated LEMP problems.

Index Terms ─ Dispersive soil, FDTD, LEMP, SARC, vector-fitting.

I. INTRODUCTION

The electromagnetic field radiated by the lightning channel is a key threat to the safety of the social electronic equipment, communication systems and power systems. Therefore, it is important to investigate the lightning-radiated electromagnetic field and its propagating property. For the past decades, the precise evaluation of lightning electromagnetic pulse (LEMP) around the lightning channel has drawn worldwide concern. The evaluation methods for LEMP can be divided into three categories: theory, numerical simulations, and experimental validation [1]. Since the analytical formulation is restricted to unrealistically simple configurations and the experiment is not easy to be implemented, the numerical simulation has been increasingly employed in investigations of LEMP problems.

During the past decades, lots of numerical methods, such as the method of moments (MoM) [2], the finite-difference time-domain (FDTD) method [3-5], the finite-element method (FEM) [6,7], the transmission-line-modeling (TLM) method [8], and the partial-element equivalent-circuit (PEEC) method [9], have been adopted to calculate the LEMP generated by return strokes. Among these methods, the FDTD method is the most widespread choice, with the advantages of the efficiently modeling of inhomogeneous parameters, 3-D structures, grounding systems and the complex ground surface.

The FDTD evaluation of LEMP is firstly introduced by Yang [3] in 2-D cylindrical coordinates. And then Baba and Rakov [4] adopted a 3-D FDTD method for the LEMP analysis. Yang [5] proposed a two-step approach for simulating the LEMP problems, by combining the 2-D cylindrical FDTD method and the 3-D FDTD method. For the evaluation of the LEMP radiated from a vertical channel over a rotationally symmetrical ground, it is more advantageous to use the 2-D cylindrical FDTD method, since much less computational resource is required than the 3-D FDTD method.

The ground electronic parameters play an important role in the evaluation of LEMP. For the lightning frequency range, soil materials may exhibit relatively dispersive properties, which can affect the distributions of the LEMP [3, 6, 7]. However, in the FDTD evaluation of LEMP, the ground electronic parameters are always assumed either as a perfect electric conductor (PEC) or as a lossy homogeneous medium characterized by constant electrical parameters. To the best of our knowledge, none of the reports on the FDTD evaluation of LEMP has taken the dispersive property of soil into account.

In this paper, the 2-D cylindrical FDTD method for evaluation the LEMP is developed, which takes the soil dispersion into account. With the vector-fitting scheme [10], the engineering model of the dispersive soil is translated into a new form, which can be easily dealt with in FDTD. The FDTD updating equations for dispersive soil are developed by introducing the semi-analytical recursive convolution (SARC) algorithm [11]. For truncating the dispersive soil, the updating equations of CPML are also developed in cylindrical coordinates. The validation of the proposed method is proved by comparing its numerical results with those obtained from the Cooray-Rubinstein (CR) approximation [12]. The proposed method can be further incorporated into the

Submitted On: November 16, 2016
Accepted On: October 4, 2017

two-step method [5] to simulate more complicated LEMP problems, such as the coupling of underground cables and cavities.

II. METHODOLOGY

A. Computational model

In engineering models, the lightning channel is assumed to be straight and vertical to a rotationally symmetrical ground, as shown in Fig. 1. The field components H_φ, E_ρ, E_z are all independent of azimuth angle, therefore the lightning electromagnetic field around the lightning channel can be simulated by the two-dimensional FDTD in cylindrical coordinates [3]. The 2D-FDTD mesh is also depicted in Fig. 1.

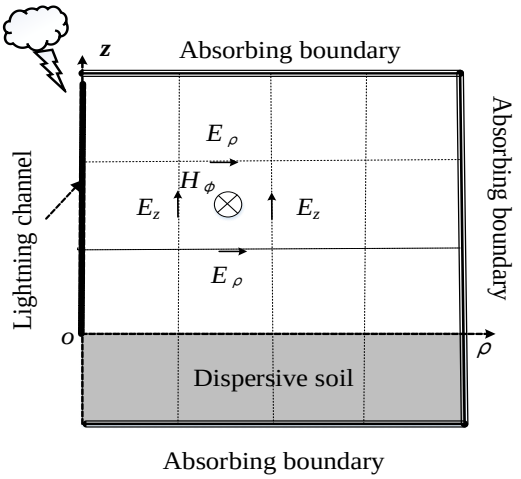

Fig. 1. Computational configurations.

The FDTD evaluation of the LEMP is achieved by solving the Maxwell's equations in the simulation area, with lightning currents along the lightning channel as exciting sources. For an isotropic, inhomogeneous, conductive, linear medium, the Maxwell's equations in the two-dimensional cylindrical coordinates (TMz) can be written as [13]:

$$-\mu_0 \frac{\partial H_\varphi}{\partial t} = \frac{\partial E_\rho}{\partial z} - \frac{\partial E_z}{\partial \rho}, \tag{1a}$$

$$\frac{\partial D_z}{\partial t} + \sigma E_z = \frac{1}{\rho}\frac{\partial (\rho H_\varphi)}{\partial \rho} = \frac{\partial (H_\varphi)}{\partial \rho} + \frac{H_\varphi}{\rho}, \tag{1b}$$

$$-\frac{\partial D_\rho}{\partial t} - \sigma E_\rho = \frac{\partial H_\varphi}{\partial z}, \tag{1c}$$

where μ_0 is the permeability of free space, σ is the conductivity. D_ρ, D_z are the displacement, which satisfy the constitutive relation to the electric field in frequency domain:

$$\begin{aligned} D_s(\omega) &= \varepsilon_0 \varepsilon_r(\omega) E_s(\omega) \\ &= \varepsilon_0 \left(\varepsilon_r'(\omega) - \mathrm{j}\varepsilon_r''(\omega)\right) E_s(\omega) \quad s = \rho, z \end{aligned}, \tag{2}$$

where ε_0 is the permittivity of free space, $\varepsilon_r(\omega)$ is the relative permittivity. $\varepsilon_r'(\omega)$ and $\varepsilon_r''(\omega)$ are the real part and the image part of $\varepsilon_r(\omega)$, respectively. According to the Fourier transform, (2) in time domain can be derived as:

$$D_s(t) = \varepsilon_0 \varepsilon_r(t) * E_s(t), \tag{3}$$

where $*$ is the convolution operator. When $\varepsilon_r(\omega)$ is frequency-dependent, solving the convolution results by direct-integration with FDTD is much time consuming.

B. Parameters of the dispersive soil

(1) Longmire & Smith model

The engineering models for dispersive soils are expressed in terms of curve-fitting expressions for the soil conductivity and relative permittivity based on experimental data. In this paper, we use the universal Longmire & Smith (LS) model [14] to represent the electrical parameters of dispersive soils. Based on the experimental data of Scott, the LS model expresses the soil parameters as functions of frequency and percentage of water content:

$$\sigma_{LS}(f) = \sigma_0 + \sigma_f'(f) = \sigma_0 + 2\pi\varepsilon_0 \sum_{n=1}^{N} \frac{a_n f_n (f/f_n)^2}{1+(f/f_n)^2}, \tag{4a}$$

$$\varepsilon_{r,LS}(f) = \varepsilon_\infty + \varepsilon_f'(f) = \varepsilon_\infty + \sum_{n=1}^{N} \frac{a_n}{1+(f/f_n)^2}, \tag{4b}$$

where $\sigma_0 = 8\cdot(p/10)^{1.54}\cdot 10^{-3}$ is the low-frequency conductivity at 100 Hz, f is the frequency, ranging from DC to 5 MHz, $\sigma_{LS}(f)$ and $\varepsilon_{r,LS}(f)$ are the soil conductivity and relative permittivity at each frequency, respectively. p is the water percentage of soil, and a_n are coefficients presented in Table 1. The LS model satisfies the Kramers–Kronig relationships, and thus provides causal results [15]. Typical curves associated with the frequency dependence of the soil relative permittivity and conductivity for different soil water contents are shown in Fig. 2.

Table 1: Coefficients a_n of the LS model

n	1	2	3	4	5	6	7
a_n	3.4e6	2.74e5	2.58e4	3.38e3	526	133	27.2
n	8	9	10	11	12	13	14
a_n	12.5	4.8	2.17	0.98	0.392	0.173	0

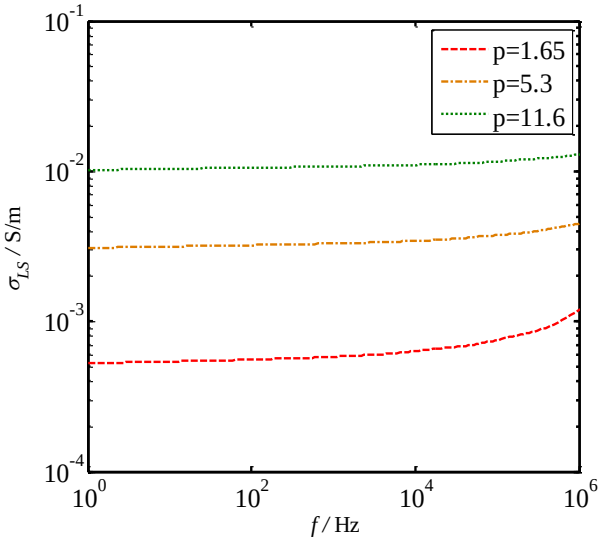

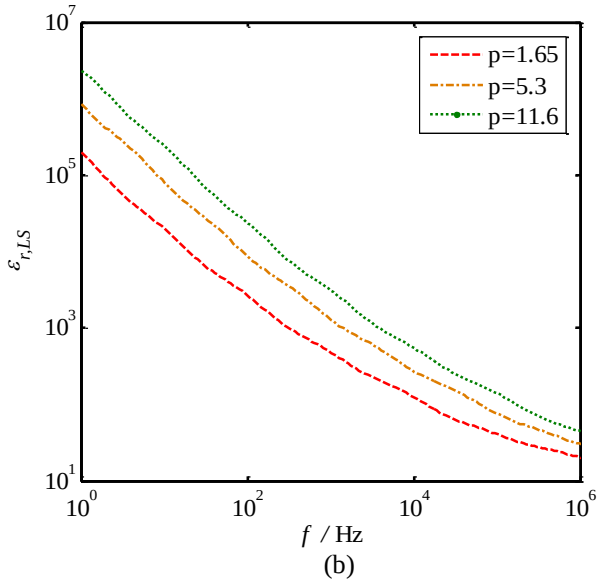

Fig. 2. Parameters of the dispersive soil over the frequency range of interest with different soil water contents: (a) relative permittivity and (b) conductivity.

(2) Translate LS model into FDTD parameters

The relations between the parameters of LS model and those in FDTD are [15]:

$$\sigma_{FDTD} = \sigma_0 , \tag{5a}$$

$$\varepsilon_{r,FDTD}(\omega) = \varepsilon_r'(\omega) - \mathrm{j}\varepsilon_r''(\omega)$$
$$= \varepsilon_{r,LS}(f) + \frac{\sigma_f'(f)}{j2\pi f \varepsilon_0} = \varepsilon_{r,LS}\left(\frac{\omega}{2\pi}\right) + \frac{\sigma_f'(\omega/2\pi)}{j\omega\varepsilon_0} . \tag{5b}$$

The high order rational fraction form of $\varepsilon_{r,FDTD}$ is difficult to deal with in FDTD scheme. Therefore, we employ the vector-fitting scheme [10] to reform $\varepsilon_{r,FDTD}$ as:

$$\varepsilon_{r,FDTD}(\omega) = \varepsilon_c + \chi(\omega) = \varepsilon_c + \sum_{q=1}^{Q} \frac{r_q}{j\omega - p_q} , \tag{6}$$

where ε_c is constant, r_q , p_q are the residues and poles, respectively. The fitting results and the relative fitting errors of the relative permittivity for different water contents are shown in Fig. 3. As we can see, the VF fitting results are excellent. The differences between the curves p=5.3 and p=11.6 caused by the different fitting orders Q employed (Q=17 for p=5.3, Q=14 for p=1.65 and p=11.6).

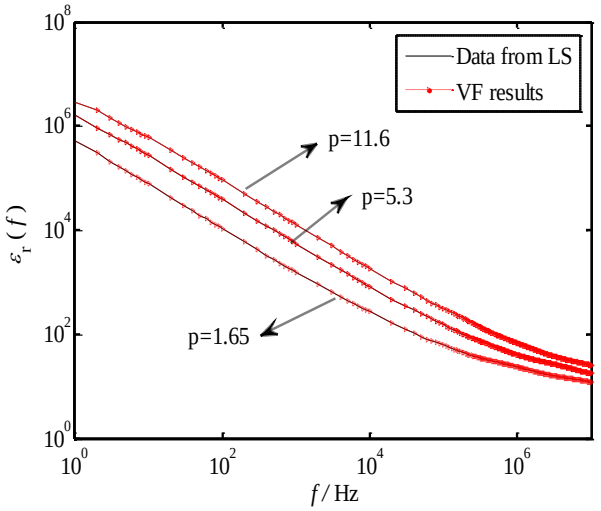

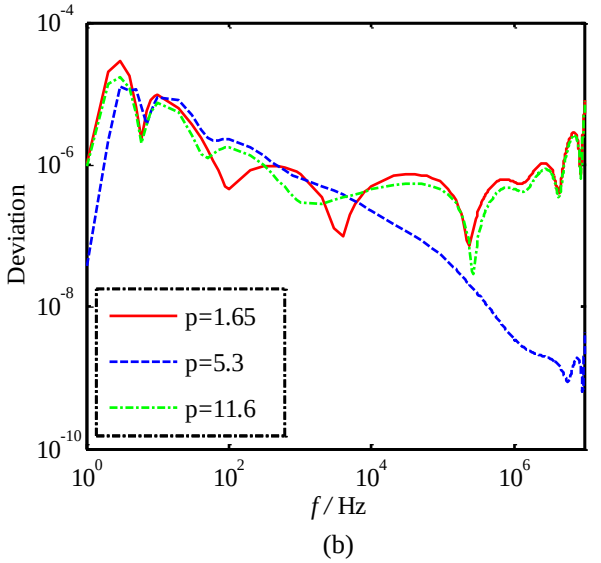

Fig. 3. The vector-fitting results of ε_r with different soil water contents p: (a) VF results and (b) deviations.

C. FDTD Updating equations for the dispersive soil

(1) Algorithms for the constitutive relation [11]

If $\varepsilon_r(\omega)$ has the form of (6), according to the frequency-time relation $1/(\alpha+j\omega)\rightarrow\exp(-\alpha t)U(t)$, the translation form of (2) in time domain is:

$$\begin{aligned} D_s(t) &= \varepsilon_0\left(\varepsilon_c E_s(t)+E_s(t)*\chi(t)\right) \\ &= \varepsilon_0\left(\varepsilon_c E_s(t)+E_s(t)*\left(\sum_{q=1}^{Q} r_q\exp(p_q t)U(t)\right)\right), \\ &= \varepsilon_0\left(\varepsilon_c E_s(t)+\sum_{q=1}^{Q}\psi_{s,q}^{n}(t)\right) \end{aligned} \quad (7)$$

where $$\psi_{s,q}(t)=E_s(t)*r_q\exp(p_q t)U(t). \quad (8)$$

Discretize (8) with time interval $t=n\Delta t$, we obtain:

$$\begin{aligned} \psi_{s,q}^{n} &= \int_0^{n\Delta t} r_q\exp\left(p_q(n\Delta t-\tau)\right)E_s(\tau)\,d\tau \\ &= \int_0^{(n-1)\Delta t} r_q\exp\left(p_q(n\Delta t-\tau)\right)E_s(\tau)\mathrm{d}\tau \\ &\quad +\int_{(n-1)\Delta t}^{n\Delta t} r_q\exp\left(p_q(n\Delta t-\tau)\right)E_s(\tau)\mathrm{d}\tau \\ &= \exp\left(p_q\Delta t\right)\cdot\psi_{s,q}^{n-1}+y_{s,q}^{n} \end{aligned}, \quad (9)$$

where

$$y_{s,q}^{n}=r_q\exp\left(p_q n\Delta t\right)\cdot\left(\int_{(n-1)\Delta t}^{n\Delta t}\exp\left(-p_q\tau\right)\right)E_s(\tau)\,d\tau\Big). \quad (10)$$

If we replace E_s over the time interval $[(n-1)\Delta t, n\Delta t]$ with the average approximation $(E_s^n+E_s^{n+1})/2$, we can get:

$$y_{s,q}^{n}=\exp(-p_q\Delta t)y_{s,q}^{n-1}+c_{0,q}(E_s^n+E_s^{n-1})/2, \quad (11)$$

where

$$c_{0,q}=\begin{cases} r_q\Delta t & p_q=0 \\ -\dfrac{r_q}{p_q}\left(1-\exp\left(p_q\Delta t\right)\right) & p_q\neq 0 \end{cases}. \quad (12)$$

(2) FDTD updating equations for the dispersive soil

Discretize (1c) with FDTD method [13]:

$$\begin{aligned} &-\frac{D_{\rho\ i+1/2,j}^{n+1}-D_{\rho i+1/2,j}^{n}}{\Delta t}-\sigma\frac{E_{\rho\ i+1/2,j}^{n+1}+E_{\rho i+1/2,j}^{n}}{2} \\ &=\frac{H_{\varphi\ i+1/2,j+1/2}^{n+1/2}-H_{\varphi\ i+1/2,j-1/2}^{n+1/2}}{\Delta z} \end{aligned}. \quad (13)$$

Substitute (7) into (13), we obtain the updating equation for E_ρ:

$$\begin{aligned} E_{\rho\ i+1/2,j}^{n+1} &= CA\cdot E_{\rho i+1/2,j}^{n} \\ &-CB\cdot\Delta t\cdot\frac{H_{\varphi\ i+1/2,j+1/2}^{n+1/2}-H_{\varphi\ i+1/2,j-1/2}^{n+1/2}}{\Delta z}, \\ &+CB\cdot\varepsilon_0\cdot\sum_{q=1}^{Q}\left((1-\exp(p_q\Delta t))\psi_{\rho,qi+1/2,j}^{n}\right) \end{aligned} \quad (14)$$

where

$$CA=\frac{\varepsilon_0(\varepsilon_c-\frac{1}{2}\sum_{q=1}^{Q}c_{0,q})-\frac{\sigma\Delta t}{2}}{\varepsilon_0(\varepsilon_c+\frac{1}{2}\sum_{q=1}^{Q}c_{0,q})+\frac{\sigma\Delta t}{2}}, \quad (15a)$$

$$CB=\frac{1}{\varepsilon_0(\varepsilon_c+\frac{1}{2}\sum_{q=1}^{Q}c_{0,q})+\frac{\sigma\Delta t}{2}}, \quad (15b)$$

$$\psi_{\rho,q}^{n+1}=\exp\left(p_q\Delta t\right)\cdot\psi_{\rho,q}^{n}+c_{0,q}(E_\rho^n+E_\rho^n)/2. \quad (16)$$

Similarly, we can derive the updating equation for E_z:

$$\begin{aligned} E_{z\ i,j+1/2}^{n+1} &= CA\cdot E_{z\ i,j+1/2}^{n} \\ &+CB\cdot\varepsilon_0\cdot\sum_{q=1}^{Q}\left\{\left[1-\exp(p_q\Delta t)\right]\psi_{z,qi,j+1/2}^{n}\right\} \\ &+CB\cdot\Delta t\cdot\left(\begin{array}{l}\dfrac{H_{\varphi\ i+1/2,j+1/2}^{n+1/2}-H_{\varphi\ i-1/2,j+1/2}^{n+1/2}}{\Delta\rho} \\ +\dfrac{H_{\varphi\ i+1/2,j+1/2}^{n+1/2}+H_{\varphi\ i-1/2,j+1/2}^{n+1/2}}{2\rho_i}\end{array}\right). \end{aligned} \quad (17)$$

CA, CB are the same as (15). Since (1a) has none dispersive parameters, the updating equation for H_φ is:

$$\begin{aligned} H_\varphi^{n+1/2}(i+1/2,j+1/2) &= H_\varphi^{n-1/2}(i+1/2,j+1/2) \\ -CC\cdot&\left[\begin{array}{l}\dfrac{E_\rho^n(i+1/2,j+1)-E_\rho^n(i+1/2,j)}{\Delta z} \\ -\dfrac{E_z^n(i+1,j+1/2)-E_z^n(i,j+1/2)}{\Delta\rho}\end{array}\right] \end{aligned}, \quad (18)$$

where $CC=\Delta t/\mu_0$.

(14), (17) and (18) are the updating equations for the dispersive soil.

D. CPML for the dispersive soil

The absorbing boundary condition is an essential technique in truncating the FDTD computational domain for open problem simulations. The Mur's boundary [16] is commonly employed in the FDTD simulations of LEMP [3, 5]. However, the absorbing performance of the Mur's boundary degrades severely when terminates the dispersive medium. The complex frequency-shifted PML (CFS-PML) has been proven to be very efficient for truncating the dispersive medium [17]. The modified Maxwell's scalar equations in CPML can be obtained from the stretched cylindrical coordinate (TMz) [18]:

$$-\mu_0\frac{\partial H_\varphi}{\partial t}=\frac{1}{s_z}\frac{\partial E_\rho}{\partial z}-\frac{1}{s_\rho}\frac{\partial E_z}{\partial\rho}, \quad (19a)$$

$$\frac{\partial D_z}{\partial t}+\sigma E_z=\frac{1}{s_\rho}\frac{\partial\left(H_\varphi\right)}{\partial\rho}+\frac{1}{s_\varphi}\frac{H_\varphi}{\rho}, \quad (19b)$$

$$-\frac{\partial D_\rho}{\partial t}-\sigma E_\rho=\frac{1}{s_z}\frac{\partial H_\varphi}{\partial z}, \tag{19c}$$

where

$$s_\rho=k_\rho+\sigma_\rho/(\alpha_\rho+j\omega\varepsilon_0), \tag{20a}$$

$$s_z=k_z+\sigma_z/(\alpha_z+j\omega\varepsilon_0), \tag{20b}$$

$$\begin{aligned}s_\varphi&=k_\varphi+\sigma_\varphi/\alpha_\varphi+j\omega\varepsilon_0\\&=(1/\rho)[\rho_0+\int_{\rho_0}^{\rho}(k_\rho+\sigma_\rho/(\alpha_\rho+j\omega\varepsilon_0))d\rho'],\end{aligned} \tag{21}$$

ρ_0 represents the interface between FDTD and PML grids. Based on the semi-analytical recursive convolution (SARC) algorithm [11], the CPML equations for truncating the dispersive soil can be derived as:

$$\begin{aligned}&E_\rho^{n+1}{}_{i+1/2,j}=CA\cdot E^n_{\rho i+1/2,j}\\&-CB\cdot\Delta t\cdot\left(\frac{H_\varphi^{n+1/2}{}_{i+1/2,j+1/2}-H_\varphi^{n+1/2}{}_{i+1/2,j-1/2}}{k_z\Delta z}+\phi^{n+1/2}_{e\rho z\ i+1/2,j}\right),\\&+CB\cdot\varepsilon_0\cdot\sum_{q=1}^{Q}((1-\exp(p_q\Delta t))\psi^n_{\rho,qi+1/2,j})\end{aligned} \tag{22}$$

$$\begin{aligned}&E_z^{n+1}{}_{i,j+1/2}=CA\cdot E^n_{z\,i,j+1/2}\\&+CB\cdot\varepsilon_0\cdot\sum_{q=1}^{Q}\left\{\left[1-\exp(p_q\Delta t)\right]\psi^n_{z,qi,j+1/2}\right\}\\&+CB\cdot\Delta t\cdot\left(\begin{array}{l}\dfrac{H_\varphi^{n+1/2}{}_{i+1/2,j+1/2}-H_\varphi^{n+1/2}{}_{i-1/2,j+1/2}}{k_\rho\Delta\rho}+\phi^{n+1/2}_{ez\rho\ i,j+1/2}\\+\dfrac{H_\varphi^{n+1/2}{}_{i+1/2,j+1/2}+H_\varphi^{n+1/2}{}_{i-1/2,j+1/2}}{k_\varphi 2\rho_i}+\phi^{n+1/2}_{ez\varphi\ i,j+1/2}\end{array}\right),\end{aligned} \tag{23}$$

$$\begin{aligned}&H_\varphi^{n+1/2}{}_{i+1/2,j+1/2}=H_\varphi^{n-1/2}{}_{i+1/2,j+1/2}\\&-CC\cdot\left[\begin{array}{l}\dfrac{E^n_{\rho i+1/2,j+1}-E^n_{\rho i+1/2,j}}{k_z\Delta z}+\phi^n_{h\varphi z i+1/2,j+1/2}\\-\dfrac{E^n_{z\,i+1,j+1/2}-E^n_{z\,i,j+1/2}}{k_\rho\Delta\rho}-\phi^n_{h\varphi\rho i+1/2,j+1/2}\end{array}\right],\end{aligned} \tag{24}$$

The auxiliary variables ϕ for E are updated by:

$$\begin{aligned}\phi^{n+1/2}_{e\rho z\ i+1/2,j}&=b_z\cdot\phi^{n-1/2}_{e\rho z\ i+1/2,j}\\&+a_z\cdot\frac{H_\varphi^{n+1/2}{}_{i+1/2,j+1/2}-H_\varphi^{n+1/2}{}_{i+1/2,j-1/2}}{\Delta z},\end{aligned} \tag{25a}$$

$$\begin{aligned}\phi^{n+1/2}_{ez\rho\ i,j+1/2}&=b_\rho\cdot\phi^{n-1/2}_{ez\rho\ i,j+1/2}\\&+a_\rho\cdot\frac{H_\varphi^{n+1/2}{}_{i+1/2,j+1/2}-H_\varphi^{n+1/2}{}_{i-1/2,j+1/2}}{\Delta\rho},\end{aligned} \tag{25b}$$

$$\begin{aligned}\phi^{n+1/2}_{ez\varphi\ i,j+1/2}&=b_\varphi\cdot\phi^{n-1/2}_{ez\varphi\ i,j+1/2}\\&+a_\varphi\cdot\frac{H_\varphi^{n+1/2}{}_{i+1/2,j+1/2}+H_\varphi^{n+1/2}{}_{i-1/2,j+1/2}}{2\rho_i},\end{aligned} \tag{25c}$$

where $b_i=e^{(-(\sigma_i/k_i+\alpha_i)(\Delta t/\varepsilon_0))}$, $a_i=(\sigma_i/k_i^2\alpha_i+\sigma_i k_i)(b_i-1)$, $i=\rho,z,\varphi$. The updating equations for $\phi_{h\varphi z}$, $\phi_{h\varphi\rho}$ can be derived similarly, which has the same form as (25a) and (25b).

III. NUMERICAL RESULTS AND DISCUSSIONS

A. Performance of the CPML

We first simulate a point source radiation using both the proposed CPML boundary and Mur's absorbing boundary. The simulation configuration is shown in Fig. 4 (a). The overall computation domain is defined by 50*50 cells with ten-cell-thick CPML. The source located at grid point (0, 26) is given by $H_\varphi(t)=-2(\frac{t-t_0}{t_w})\exp(-(\frac{t-t_0}{t_w})^2)$ with $t_w=50\Delta t$, $t_0=200\Delta t$. The observation point is placed next to the PML boundary at grid point (12, 38). The relative reflection error is calculated as follows:

$$\text{Error}=20\log_{10}(|H_\varphi(t)-H_\varphi^{ref}(t)|/|H_{\varphi\,\max}^{ref}(t)|), \tag{26}$$

where the H_φ^{ref} is the reference result from an extended simulation with no reflection coming from the boundary.

Figure 4 (b) shows the comparison of reflection errors from CPML and Mur's boundary. It can be observed that the CPML shows excellent absorbing performance, which is much better than the Mur's boundary.

B. Evaluation of the LEMP

In this study, the modified transmission line with linear current decay with height (MTLL) [19] is adopted for modeling the lightning return stroke channel with H=7500m, assuming a return stroke speed v=1.3e8m/s. The channel height is 2000m and the channel base current is represented by Heidler's function [20]:

$$\begin{aligned}i(0,t)=\frac{I_{01}}{\eta}\cdot\frac{(t/\tau_1)^2}{(t/\tau_1)^2+1}\cdot\exp(-t/\tau_2)\\+I_{02}\left[\exp(-t/\tau_3)-\exp(-t/\tau_4)\right]\end{aligned}, \tag{27}$$

with parameters listed in Table 2.

Table 2: Parameters of the channel base current

I_{01}/kA	I_{02}/kA	τ_1/μs	τ_2/μs	τ_3/μs	τ_4/μs	η
9.9	7.5	0.072	5.0	100.0	6.0	0.845

The parameters of the dispersive soil are obtained from the LS model with the water content of 1.65, which is associated with the low-frequency conductivity of σ_0=0.0005 S/m. Calculations are carried out by the proposed FDTD method with frequency-dependent

soil parameters (FD-FDTD) and the traditional FDTD method with constant soil parameters (CP-FDTD, σ =0.0005 S/m, ε_r =10). For comparison, the LEMP is also evaluated by the Cooray–Rubinstein (CR) formulation with frequency-dependent soil parameters.

The horizontal electric fields evaluated by different methods are shown in Fig. 5. As we can see, the results of FD-FDTD method agree well with the CR approximation, which prove that the proposed FDTD method can evaluated the LEMP with dispersive soil efficiently. On the other hand, the results of CP-FDTD display obvious deviations from the CR approximations, which validate the necessity to consider the dispersive property of soil in the evaluation of LEMP.

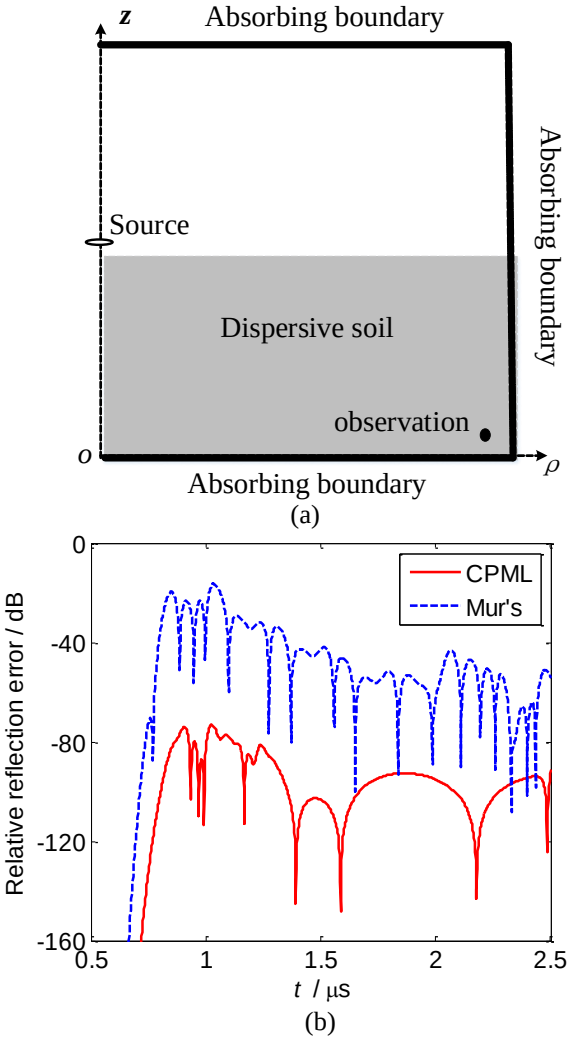

Fig. 4. Comparison of the absorbing performances of CPML and Mur's boundary: (a) computational configurations and (b) relative reflection errors.

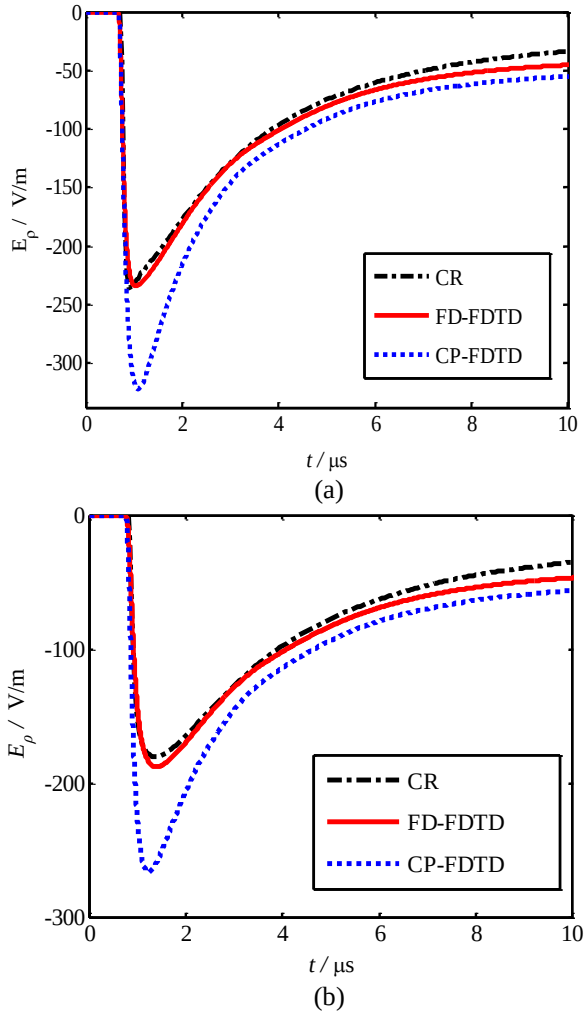

Fig. 5. The horizontal electric fields evaluated by different methods at 200m away from the lightning channel: (a) 1m below the ground and (b) 10m below the ground.

C. Effects of the soil dispersion

In order to further investigate the effect of soil dispersion, we evaluate the LEMPs with different water content percentage of p=1.65%, 5.3% and 11.6%, which are respectively associated with low-frequency conductivities of σ=0.0005, 0.003, and 0.01 S/m [6]. As comparisons, simulations of the traditional FDTD method with constant soil parameters are carried out simultaneously, with ε_r =10, σ=0.0005, 0.003 and 0.01 S/m respectively.

The horizontal electric fields calculated by the two methods with different soil water contents are shown in Fig. 6. It is shown that the dispersive property of the soil results in an attenuation of the amplitude of the

horizontal electric fields. As the decrease of the water content, the decrease of the amplitude becomes more noticeable. Therefore, the dispersive property of the soil should not be neglected in the evaluation of LEMP, especially for the poorly conducting soil.

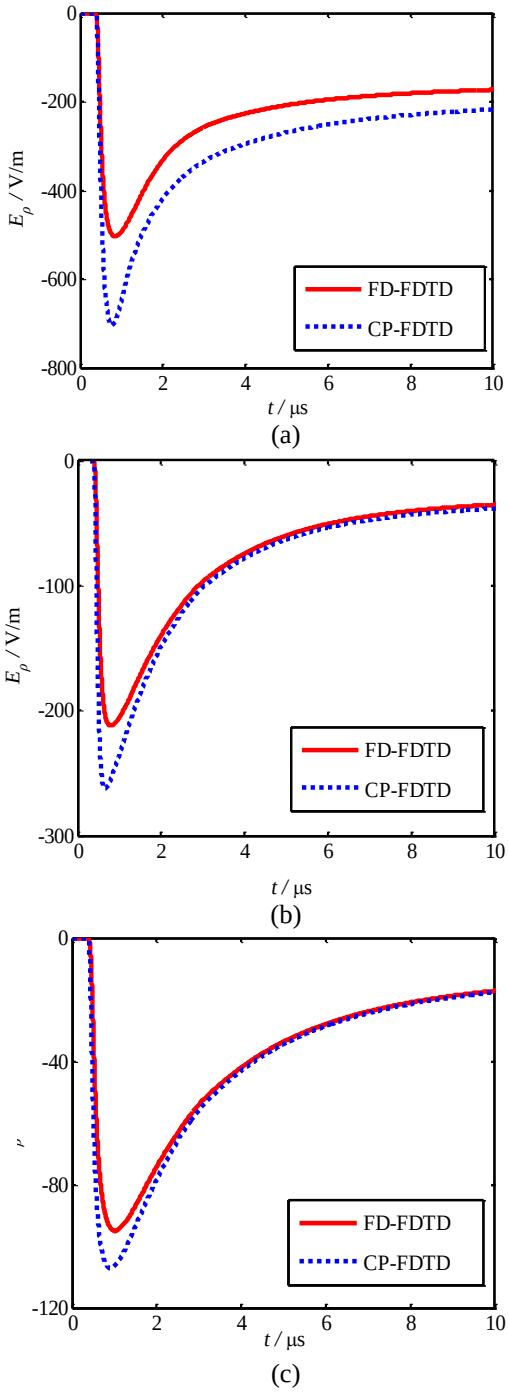

Fig. 6. The horizontal electric fields evaluated with different soil water contents (100m away from the lightning channel, 5m below the ground): (a) p=1.65, (b) p=5.3, and (c) p=11.6.

IV. CONCLUSION

To precisely evaluate the LEMP, the 2D-FDTD method in cylindrical coordinates is further developed for simulating the dispersive soil, by employing the SARC scheme. The cylindrical CPML is also derived for truncating the dispersive soil. The numerical results validate that the proposed method can evaluate the LEMP efficiently with the soil dispersion considered, which leads to a more accurate results than the FDTD methods that disregard the soil dispersion. It was also shown that the soil dispersion can significantly affect the LEMP values for soils with very low conductivity. The proposed method inherits the advantages of the FDTD method, which is efficient in modeling the inhomogeneous ground and the rough ground surface. The proposed method provides an efficient way to an accurate evaluation of LEMP with FDTD, which can be further incorporated into the simulations of more complicated LEMP problems.

ACKNOWLEDGMENT

This work was supported by NSFC in China under Grant No. 51477183 and Jiangsu Natural Science Foundation No. BK20170757.

REFERENCES

[1] M. Paolone, F. Rachidi, A. Borghetti, et al., "Lightning electromagnetic field coupling to overhead lines: Theory, numerical simulations, and experimental validation," *IEEE Trans. Electromagn. Compat.*, vol. 51, no. 3, pp. 532-547, 2009.

[2] M. Albani, A. Mazzinghi, and A. Freni, "Rigorous MoM analysis of finite conductivity effects in RLSA antennas," *IEEE Trans. Antennas Propagat.*, vol. 59, no. 11, pp. 4023-4032, 2011.

[3] C. Yang and B. Zhou, "Calculation method of electromagnetic field very close to lightning," *IEEE Trans. Electromagn. Compat.*, vol. 49, no. 1, pp. 133-141, 2004.

[4] Y. Baba and V. A. Rakov, "Voltages induced on an overhead wire by lightning strikes to a nearby tall grounded object," *IEEE Trans. Electromagn. Compat.*, vol. 48, no. 1, pp. 212-224, 2006.

[5] B. Yang, B. Zhou, C. Gao, et al., "Using a two-step finite-difference time-domain method to analyze lightning induced voltages on transmission lines," *IEEE Trans. Electromagn. Compat.*, vol. 53, no. 1, pp. 256-260, 2011.

[6] M. Akbari, K. Sheshyekani, A. Pirayesh, et al., "Evaluation of lightning electromagnetic fields soil electrical parameters and their induced voltages on overhead lines considering the frequency dependence," *IEEE Trans. Electromagn. Compat.*, vol. 55, no. 6, pp. 1210-1219, 2013.

[7] J. Paknahad, K. Sheshyekani, F. Rachidi, et al., "Evaluation of lightning-induced currents on

cables buried in a lossy dispersive ground," *IEEE Trans. Electromagn. Compat.*, vol. 56, no. 6, pp. 1522-1529, 2014.

[8] P. B. Johns and R. B. Beurle, "Numerical solutions of 2-dimensional scattering problems using a transmission-line matrix," *Proc. IEE*, vol. 118, no. 9, pp. 1203-1208, 1971.

[9] A. Ruehli, "Equivalent circuit models for three-dimensional multiconductor systems," *IEEE Trans. Microw. Theory Techn.*, vol. 22, no. 3, pp. 216-221, 1974.

[10] B. Gustavsen and A. Semlyen, "Rational approx.-imation of frequency domain responses by vector fitting," *IEEE Transactions on Power Delivery*, vol. 14, no. 3, pp. 1052-1061, 1999.

[11] Y. Q. Zhang and D. B. Ge, "A unified FDTD approach for electromagnetic analysis of dispersive objects," *Progress in Electromagnetics Research*, vol. 96, pp. 155-172, 2009.

[12] V. Cooray, "Some considerations on the 'Cooray–Rubinstein' approximation used in deriving the horizontal electric field over finitely conducting ground," *IEEE Trans. Electromagn. Compat.*, vol. 44, no. 4, pp. 560-565, 2002.

[13] A. Taflove and S. C. Hagness, *Computational Electrodynamics The Finite-Difference Time-Domain Method*, 3rd ed., Norwood, MA: Artech House, 2005.

[14] C. L. Longmire and K. S. Smith, "A universal impedance for soils," *Defense Nuclear Agency*, Topical Report for Period, Santa Barbara, CA, USA, 1975.

[15] D. Cavka, N. Mora, and F. Rachidi, "A comparison of frequency-dependent soil models: Application to the analysis of grounding systems," *IEEE Trans. Electromagn. Compat.*, vol. 48, no. 1, pp. 177-187, 2013.

[16] G. Mur, "Absorbing boundary conditions for the finite-difference approximation of the time-domain electromagnetic field equations," *IEEE Trans. Electromagn. Compat.*, vol. 23, pp. 377-382, 1981.

[17] J. A. Roden and S. D. Gedney, "Convolution PML (CPML): An efficient FDTD implementation of the CFS-PML for arbitrary media," *Microw. Opt. Tech. Lett.*, vol. 27, no. 5, pp. 334-339, 2000.

[18] J. Liu, G. Wan, J. Zhang, and X. Xi, "An effective CFS-PML implementation for cylindrical coord-inate FDTD method," *IEEE Microw. Wireless Compon. Lett.*, vol. 22, no. 6, pp. 300-302, 2012.

[19] V. A. Rakov and A. A. Dulzon, "Calculated electromagnetic fields of lightning return stroke," *Tekh. Elektr.*, no. 1, pp. 87-89, 1987.

[20] F. Heidler, "Travelling current source model for LEMP calculation," *Proc. 6th Int. Symp. Electromagn. Compat.*, Zurich, Switzerland, pp. 157-162, 1985.

Zheng Sun received the B.S. degree in Automatic Control in 2009 from Sourthest University, Jiangsu, China and Ph.D. degree of Electrical Engineering in PLA University of Science & Technology, Jiangsu, China, in 2014, respectively. He is currently working as a Lecturer in the PLA Army Engineering University, with his main interests on computing electromagnetics and lightning protections.

LiHua Shi received the B.S. degree from Xidian University, Shanxi, China, in 1990, the M.S. degree from Nanjing Engineering Institute, Jiangsu, China, in 1993,and the Ph.D. degree from the Nanjing University of Aeronautics and Astronautics, Jiangsu, in 1996,respectively. During 2001, he worked as a Visiting Scholar in Stanford University. He is currently working as a Professor in the PLA Army Engineering University, with his main interests on time-domain measurement technology.

Shi is a Member of the IEEE's I&M society and EMC society.

Design of a Jerusalem-Cross Slot Antenna for Wireless Internet Applications

Shu-Huan Wen and Hsing-Yi Chen

Department of Communications Engineering
Yuan Ze University, Chung-Li, Taoyuan, 32003, Taiwan
s1058603@mail.yzu.edu.tw, eehychen@saturn.yzu.edu.tw

Abstract ─ This paper provides a fast solution for the design of a Jerusalem-cross slot antenna for arbitrarily specifying any two operating frequencies. From simulation data and measurement results, the dual-resonant frequencies of the Jerusalem-cross slot antenna are found at near 5.8 and 24.0 GHz for the impedance matching with better than 15 dB return loss. It is found that the simulated and measured -10 dB bandwidths are 22.1% and 24.4% at 5.8 GHz respectively. The simulated and measured -10 dB bandwidths are 3.41% and 4.58% at 24.0 GHz, respectively. The simulated and measured results of radiation patterns in the E- and H-plane at frequencies of 5.8 and 24.0 GHz are broad and smooth. The antenna gains obtained by measurement and simulation at frequencies of 5.8 and 24.0 GHz are close to 3.0 and 6.0 dBi, respectively. This Jerusalem-cross slot antenna has a compact size with three dimensions of 22.731×7.577×0.87 mm which can be fabricated at a low cost using the standard PCB process. The compact patch antenna is suitable for applications in unlicensed frequency bands of 5.8 and 24 GHz for wireless internet applications including RFID systems, medical devices, and the internet of things (IoT).

Index Terms ─ Antenna gain, dual-resonant frequencies, Jerusalem-cross frequency selective surface, radiation pattern,

I. INTRODUCTION

Recently, the internet of things (IoT) is a booming market. Under the concept of IoT, tens of billions of devices and systems can be connected via wireless technologies [1]. The IoT can be widely applied in healthcare, utility, media, transportation, environment and energy management, exploration, and smart homes/cites. Its demand for incorporating with wireless technologies is increasing. This will increase the demand for IoT antennas compliant to IoT modules. The type and number of wireless technologies used in IoT will impact the type and number of antennas needed. Since an IoT module should be designed as compact as possible, the corresponding system board sizes and antenna volume should be miniaturized to form miniaturized sensors that meet versatile IoT needs. The types of IoT antennas may be chip antennas, wire antennas, whip antennas, or patch antennas.

Patch antennas have many advantages including low profile, low weight, low cost, and easy fabrication. Nevertheless, a patch antenna also has many drawbacks such as narrow band, low gain, low efficiency, poor polarization purity, and limited power capacity. Many researchers extend great effort to overcome these drawbacks in order to make full use of the advantages of a patch antenna. These efforts include selecting suitable substrate, changing the patch antenna's shape and size, using a variety of feeding techniques, application of impedance matching methods, using stacked layer structures, and the implementation of frequency selective surfaces [2-19].

Frequency selective surface (FSS) has a wide variety of applications including the design of antennas [17-31]. The FSS is usually formed by periodic arrays of metallic patches or slots of arbitrary geometries. The patch type FSS is used where reflection is maximum at resonant frequencies, while the slot type FSS is used where transmission is maximum at resonant frequencies. The FSS structure has a phenomenon with high impedance surfaces that reflect the plane wave in-phase and suppress surface waves. Therefore, a patch antenna with one FSS structure can improve its radiation efficiency, bandwidth, gain, and reduce the side lobe and back lobe level in its radiation pattern [17], [18], [32].

In this study, the frequency bands of 5.8 and 24.0 GHz are chosen for designing a Jerusalem-cross slot antenna based on frequency selective surface (FSS). We consider the WiFi frequency range at 5.8 GHz for this study because it is an unlicensed use and may be used for wireless internet applications including RFID systems and IoT. Recently, the 24.0 GHz frequency has been proposed by several authors from industry and academia [33-35] for wireless internet applications. The 24.0 GHz industrial, scientific, and medical (ISM) frequency band is of wide interest because unlicensed devices and services are permitted and the atmospheric attenuation does not compromise the communication [36].

Based on a dual-band Jerusalem-cross FSS with a

Submitted On: September 18, 2017
Accepted On: January 1, 2018

Rogers RO4003 substrate on one side, a compact Jerusalem-cross slot antenna is designed for wireless internet applications operating at 5.8 and 24.0 GHz. Return losses, radiation patterns, and antenna gains of the Jerusalem-cross slot antenna at 5.8 and 24.0 GHz are presented in this paper. Comparison of antenna performance between measurement results and HFSS (Ansoft, Pittsburgh, PA) simulation data is also made.

II. ANTENNA DESIGN

Based on previous research works [37-38], we can quickly obtain optimum values of geometrical parameters of a dual-band Jerusalem-cross FSS with a Rogers RO4003 substrate operating at two resonant frequencies of 5.8 and 24.0 GHz in 20.66 seconds. Figure 1 shows the Jerusalem-cross FSS with a Rogers RO4003 substrate on one side and its optimum values of geometrical parameters p, w, s, h, d, t and T. In Fig. 1, p = 7.577 mm is the periodicity of a unit cell, w = 0.6059 mm is the width of the conductive strip, s = 0.1294 mm is the separation distance between adjacent units, h = 0.3793 mm is the width of the end caps of the Jerusalem-cross, d = 4.931 mm is the length of the end caps of the Jerusalem-cross, t = 0.035mm is the thickness of the metallic foil, and T = 0.8 mm is the thickness of the Rogers RO4003 substrate. The relative dielectric constant and dielectric loss tangent of the Rogers RO4003 substrate are $\varepsilon_r = 3.31$ and $\tan\delta = 0.0027$, respectively. Figure 2 shows the frequency response of transmission of the Jerusalem-cross FSS with the Rogers RO4003 substrate on one side obtained by a HFSS simulator. It is clear that resonant frequencies of this patch FSS can be found very close to 5.8 and 24.0 GHz, respectively.

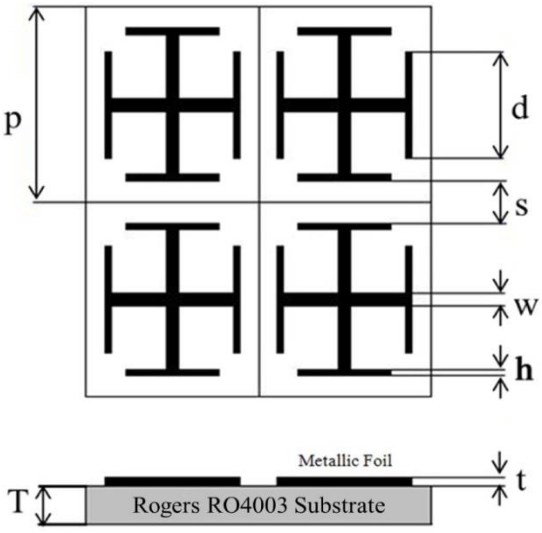

Fig. 1. A Jerusalem-cross FSS with a Rogers RO4003 substrate on one side operating at 5.8 and 24.0 GHz.

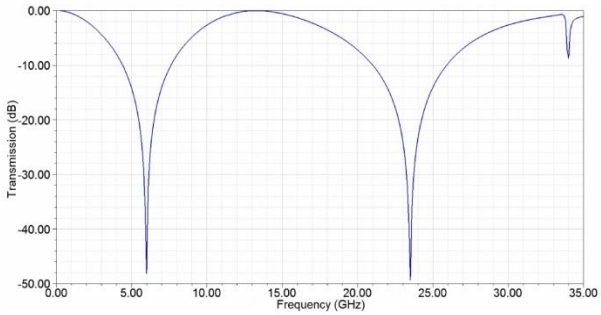

Fig. 2. Frequency response of transmission of the dual-band Jerusalem-cross FSS with a Rogers RO4003 substrate on one side.

For a slot FSS, it is designed where transmission is maximum but reflection is minimum in the neighborhood of the resonant frequency. In designing a Jerusalem-cross slot antenna, a complementary patch FSS (slot FSS) with a Rogers RO4003 substrate on one side is used as the radiator of the antenna. Figure 3 shows a Jerusalem-cross slot antenna with an off-center feeding to excite dual resonant frequencies of 5.8 and 24.0 GHz. This antenna has a compact size with dimensions of 22.731×7.577×0.87 mm. The same geometrical parameters of the patch FSS as shown in Fig. 1 are used to construct the slot FSS of this antenna. This antenna is designed on a single layer Rogers PCB board with a relatively big ground plane. The ground plane of this antenna would change the radiation performance, especially, the radiation pattern. A 50-ohm micro-strip feeding line having a length of L=P/2 and a width of 1 mm is used to excite the antenna with an SMA connector attached on the ground plane. Frequency response of reflection coefficient (S11) of this antenna obtained by HFSS simulations is shown in Fig. 4. From Fig. 4, it is clear that the lower resonant frequency of 5.8 GHz is well matched below -10 dB in the simulation. However, unsatisfied matching is observed: the higher resonant frequency of 24 GHz is not well matched below -10dB. For IoT applications, at least -10 dB matching is usually required. Therefore, it is needed to fine tune the geometrical parameters of this antenna to overcome the unsatisfied matching problem at 24.0 GHz.

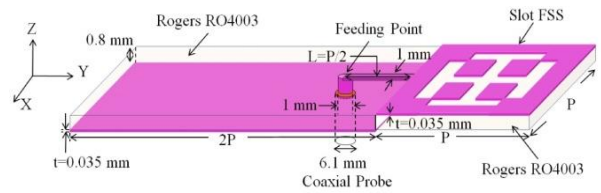

Fig. 3. The Jerusalem-cross slot antenna. The copper foil is in pink.

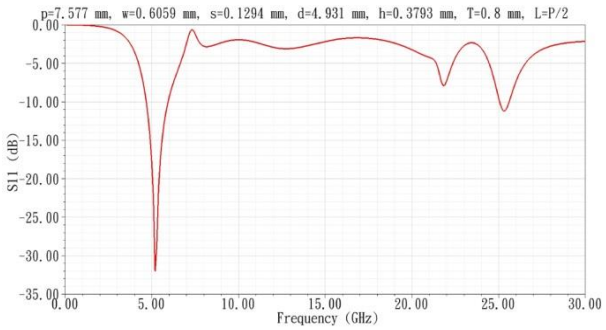

Fig. 4. Frequency response of return loss (S11) of the antenna.

In order to improve the reflection coefficient at 24 GHz, a few new optimum values of geometrical parameters of a dual-band Jerusalem-cross FSS with a Rogers RO4003 substrate are tuned by arbitrarily specifying any two resonant frequencies of 5.8 and 24.0±(0.01~0.5) GHz [37-38]. The fine-tuned geometrical parameters of the slot FSS are found to be p = 7.426 mm, w = 1.076 mm, s = 0.8693 mm, h = 0.467 mm, and d = 4.931 mm. Frequency response of reflection coefficient (S11) of the fine-tuned antenna is shown in Fig. 5. From Fig. 5, it is shown that two resonant frequencies of 5.8 and 24.0 GHz are well matched below -10 dB in HFSS simulations. It is also shown that an undesired frequency band of 19.0 GHz appears in the frequency response. In the HFSS software computer program, current distributions on the antenna surface can be simulated and presented at any frequency. In order to eliminate the undesired frequency band, the current distribution of the fine-tuned antenna at 19.0 GHz is checked and presented in Fig. 6. It is clear that higher current densities are located at the right hand side of the fine-tuned antenna at 19.0 GHz. In the final design step, two half cylinders in the left hand side of the FSS are removed to eliminate the radiation source at 19.0 GHz and the Jerusalem-cross slot antenna is reconstructed as shown in Fig. 7. In Fig. 7, the ground plane and the FSS are separated by a distance of 0.4 mm and the length of the FSS is extended by 0.1 mm. The length of the ground plane is shortened from 2 P to1.8 P. The length and width of the 50-ohm micro-strip feeding line are changed to L=P/2-0.1 mm and 1.524 mm, respectively. Frequency responses of reflection coefficient (S11) of the final Jerusalem-cross slot antenna obtained by simulation and measurement are shown in Fig. 8.

From Fig. 8, the undesired frequency band of 19.0 GHz is improved and the resonant frequencies of the patch antenna are found to be near 5.8 and 24.0 GHz for the impedance matching with better than 15 dB return loss. Return losses of 24.5 and 28.5 dB are achieved by the measurements and simulations at 5.8 GHz, respectively. On the other hand, return losses of 40.9 and 16.0 dB are achieved by the measurements and simulations at 24.0 GHz, respectively. It is found that the bandwidths for 10 dB return loss obtained by the HFSS simulations are 22.1% and 3.41% at resonant frequencies of 5.8 and 24.0 GHz respectively. It is also found that the bandwidths for 10 dB return loss obtained by the measurements are 24.4% and 4.58% at resonant frequencies of 5.8 and 24.0 GHz, respectively. It is clear that this Jerusalem-cross slot antenna provides a very wide bandwidth at 5.8 GHz. Instead of having a wide bandwidth at 5.8 GHz, the bandwidth of 3.41~4.58% occurring at 24.0 GHz is much narrower. The prototype of the Jerusalem-cross slot antenna is shown in Fig. 9. From Fig. 9, it is shown that this Jerusalem-cross slot antenna has a compact size with three dimensions of 22.731×7.577×0.87 mm.

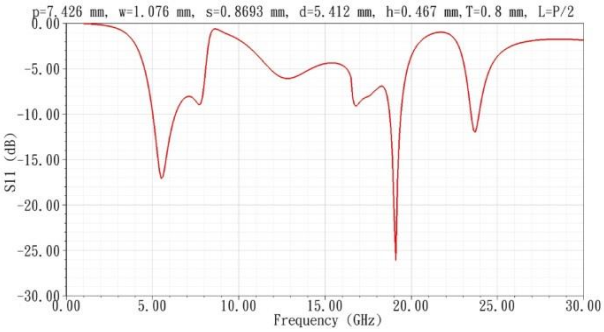

Fig. 5. Frequency response of reflection coefficient (S11) of the fine-tuned antenna.

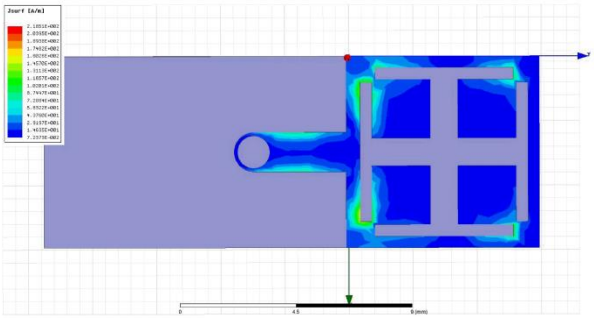

Fig. 6. Current distribution of the fine-tuned antenna at 19 GHz.

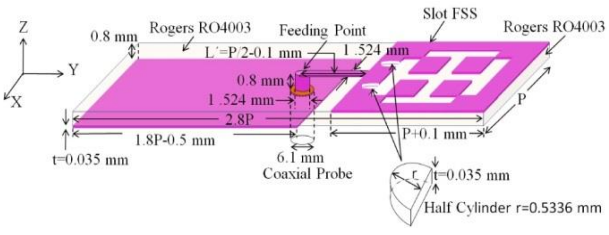

Fig. 7. The final structure of the Jerusalem-cross slot antenna. The copper foil is in pink.

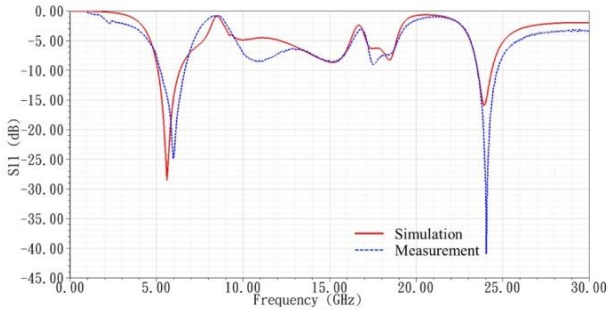

Fig. 8. Frequency response of reflection coefficient (S11) of the final Jerusalem-cross slot antenna.

(a) Top view (b) Bottom view

Fig. 9. Prototype of the Jerusalem-cross slot antenna.

III. MEASUREMENT AND SIMULATION OF ANTENNA PERFORMANCE

Measurement results and simulation data of antenna performance were obtained by using an Anritsu37369C antenna measurement system in the Yuan Ze University (YZU) anechoic chamber and by using the HFSS simulator, respectively. Measurement setup in the YZU anechoic chamber is shown in Fig. 10. Comparisons of 3-D and 2-D radiation patterns between simulation data and measurement results at 5.8 and 24.0 GHz are shown in Figs. 11-16. It can be observed that the pattern shape and beam angle obtained by the simulation and measurement are similar to each other. The radiation patterns in the E- and H-plane are broad and smooth. Radiation patterns shown in Figs. 12, 13, 15, and 16 are presented both for a co-polarization and a cross-polarization response. In general, the co-polarization is the desired polarization for an antenna design. Due to the depolarization mechanisms, a polarization orthogonal to co-polarization called cross-polarization will be generated in an antenna radiation pattern. The polarization quality is expressed by the ratio of co-polarization to cross-polarization. The averaged ratio between co-polarization and cross-polarization shown in Figs. 12 and 13 is greater than 20 dB. This indicates that the system power loss due to polarization mismatch is insignificant at 5.8 GHz. The averaged ratio between co-polarization and cross-polarization shown in Fig. 16 is also greater than 20 dB, but the averaged ratio between co-polarization and cross-polarization shown in Fig. 15 is much less than 20 dB. This means that the system power loss due to polarization mismatch may be significant at 24.0 GHz. The antenna gains obtained by simulation and measurement are shown in Table 1. The antenna gains obtained by simulation are 2.75 and 5.89 dBi at 5.8 and 24.0 GHz, respectively. The antenna gains obtained by measurement are 3.07 and 6.11 dBi at 5.8 and 24 GHz, respectively. From Figs. 11-16 and Table 1, it is shown that simulation data and measurement results make a good agreement in radiation patterns and antenna gains. This Jerusalem-cross slot antenna demonstrates a good example of dual-resonance operation at 5.8 and 24.0 GHz.

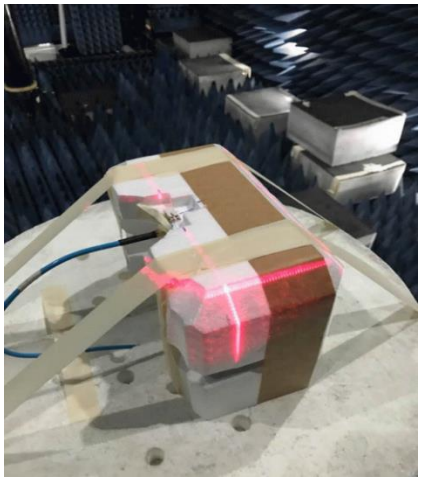

Fig. 10. Measurement setup in the YZU anechoic chamber.

Table 1: Antenna gain at 5.8 and 24.0 GHz

Frequency	5.8 GHz	24 GHz
Simulated (dBi)	2.75	5.89
Measured (dBi)	3.07	6.11

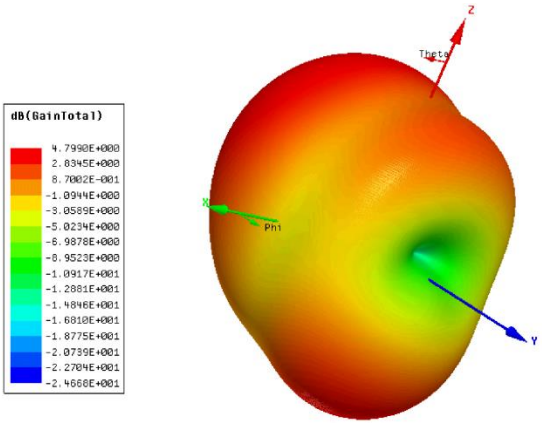

(a) Simulation

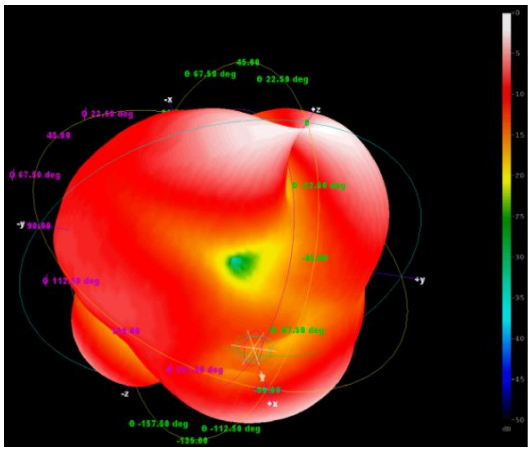

(b) Measurement

Fig. 11. Comparison of 3-D radiation patterns between simulation data and measurement results at 5.8 GHz.

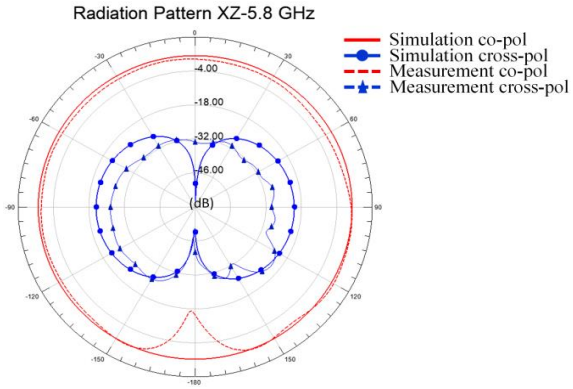

Fig. 12. Comparison of radiation patterns between simulation data and measurement results in the E-plane (x-z plane) at 5.8 GHz.

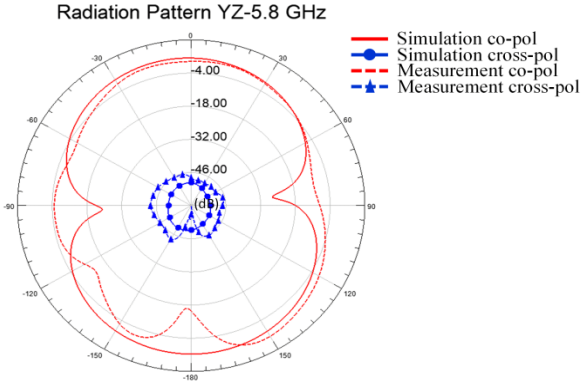

Fig. 13. Comparison of radiation patterns between simulation data and measurement results in the H-plane (y-z plane) at 5.8 GHz.

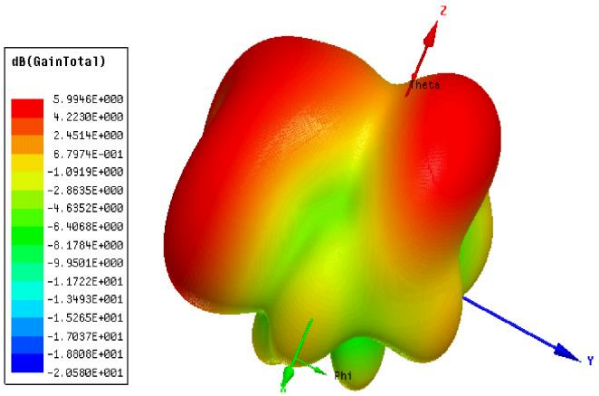

(a) Simulation

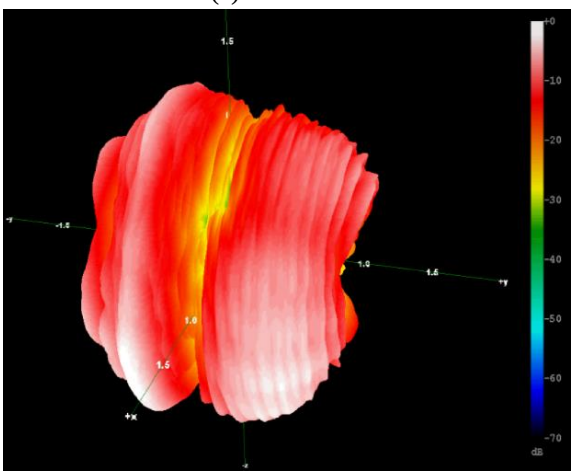

(b) Measurement

Fig. 14. Comparison of 3-D radiation patterns between simulation data and measurement results at 24.0 GHz.

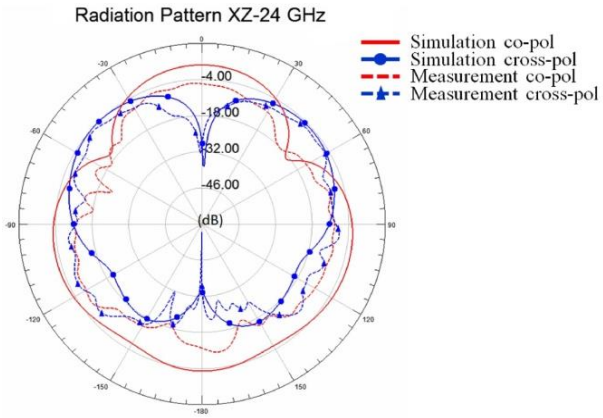

Fig. 15. Comparison of radiation patterns between simulation data and measurement results in the E-plane (x-z plane) at 24.0 GHz.

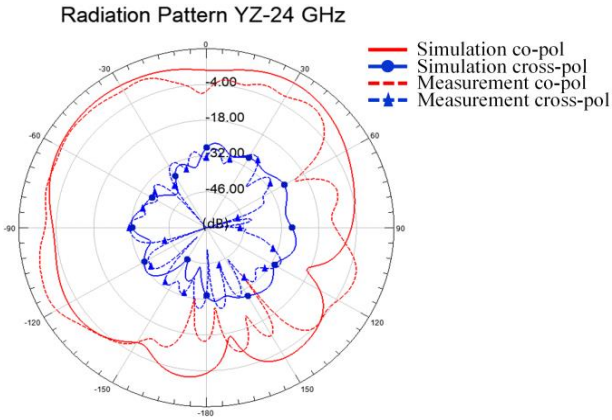

Fig. 16. Comparison of radiation patterns between simulation data and measurement results in the H-plane (y-z plane) at 24.0 GHz.

IV. CONCLUSIONS

Based on the studies of dual-band Jerusalem-cross frequency selective surface with substrates, we can quickly design a compact Jerusalem-cross slot antenna for WiFi and medical applications. The design procedure is presented in this paper. Measurement results and simulation data of antenna properties were obtained by using an Anritsu37369C antenna measurement system in the YZU anechoic chamber and by using the Ansoft high-frequency structure simulator (HFSS), respectively. It is shown that simulation data and measurement results make a good agreement in antenna properties. The dual-resonant frequencies of this patch antenna are found at near 5.8 and 24.0 GHz for the impedance matching with better than 15 dB return loss. It is found that the simulated -10 dB bandwidths are 22.1% and 3.41% at 5.8 and 24 GHz respectively. The measured -10 dB bandwidths are 24.4% and 4.58% at 5.8 and 24.0 GHz, respectively. It is clear that this Jerusalem-cross slot antenna provides a very wide bandwidth at 5.8 GHz. Broad and smooth radiation patterns are found in the E- and H-plane. The antenna gains obtained by measurement and simulation at frequencies of 5.8 and 24.0 GHz are close to 3.0 and 6.0 dBi, respectively. This compact patch antenna has three dimensions of 22.731×7.577×0.87 mm which can be fabricated at a low cost using the standard PCB process. Finally, this compact patch antenna can be used to apply in unlicensed frequency bands of 5.8 and 24.0 GHz for wireless internet applications including RFID systems, medical devices, and IoT.

REFERENCES

[1] D. Evans, *The Internet of Things: How the Next Evolution of the Internet Is Changing Everything*, White Paper, Apr. 2011 [Online]. Available: https://www.cisco.com/c/dam/en_us/about/ac79/docs/innov/IoT_IBSG_0411FINAL.pdf

[2] K. L. Wong and K. P. Yang, "Compact dual frequency microstrip antenna with a pair of bend slot," *Electronic Lett.*, vol. 34, pp. 225-226, 1988.

[3] P. C. Prasad and N. Chattoraj, "Design of compact Ku band microstrip antenna for satellite communication," *Communications and Signal Processing (ICCSP), 2013 International Conference*, pp. 196-200, Apr. 3-5, 2013.

[4] R. Q. Lee, K. F. Lee, and J. Bobinchak, "Characteristics of a two-layer electromagnetically coupled rectangular patch antenna," *Electron. Lett.*, vol. 23, pp. 1070-1072, 1987.

[5] M. Rubelj, P. F. Wahid, and C. G. Christodoulou, "A microstrip antenna array for direct broadcast satellite receivers," *Microw. Opt. Technol. Lett.*, vol. 15, no. 2, pp. 68-72, 1997.

[6] B. L. Ooi, "A double-II stub proximity feed U-slot patch antenna," *IEEE Trans. Antennas Propag.*, vol. 52, no. 9, pp. 2491-2496, Sep. 2004.

[7] R. Chair, C. L. Mak, K. F. Lee, K. M. Luk, and A. Kishk, "Minuature wide-band half U-slot and half E-shaped patch antenna," *IEEE Trans. Antennas Propag.*, vol. 53, no. 8, pp. 26452652, Aug. 2005.

[8] U. H. Park, H. S. Noh, S. H. Son, K. H. Lee, and S. I. Jeon, "A novel mobile antenna for Ku-band satellite communications," *ETRI J.*, vol. 27, no. 3, pp. 243-249, 2005

[9] R. Saluja, et al., "Analysis of bluetooth patch antenna with different feeding techniques using simulation and optimization," in *Proc. International Conference on Recent Advances in Microwave Theory and Applications*, pp. 742-744, 2008.

[10] V. V. Reddy and R. Rana, "Design of linearly polarized rectangular microstrip patch antenna using IE3D/PSO," Bachelor thesis, Department of Electronics and Communication Engineering, National Institute of Technology Rourkela, Rourkela, 2009.

[11] U. K. Revankar and A. Kumar, "Broadband stacked three-layer circular microstrip antenna arrays," *Electron. Lett.*, vol. 28, no. 21, pp. 1995-1997, 1992.

[12] E. Nishiyama, S. Egashira, and A. Sakitani, "Stacked circular polarized microstrip antenna with wide band and high gain," *Proc. IEEE AP-S Int. Symp. and URSI Radio Science Meeting*, pp. 1923-1926, 1992.

[13] S. Egashira, E. Nishiyama, and A. Sakitani, "Stacked microstrip antenna with wide band and high gain," *IEEE Trans. Antennas Propag.*, vol. 44, no. 11, pp. 1533-1534, 1996.

[14] H.-S. Noh and U.-H. Park, "Three-stacked microstrip patch array antenna for both transmitting and receiving," *IEE Proc.-Microw. Antennas Propag.*, vol. 153, no. 4, pp. 385-388, Aug. 2006.

[15] K. Agarwal, Nasimuddin, and A. Alphones, "Triple-

band compact circularly polarised stacked microstrip antenna over reactive impedance meta-surface for GPS applications," *IET Microw. Antennas Propag.*, vol. 8, no. 13, pp. 1057-1065, 2014.

[16] Y. Gao, R. Ma, Y. Wang, Q. Zhang, and C. Parini, "Stacked patch antenna with dual-polarization and low mutual coupling for massive MIMO," *IEEE Trans. Antennas Propag.*, vol. 64, no. 10, pp. 4544-4549, Oct. 2016.

[17] H. Y. Chen and Y. Tao, "Bandwidth enhancement of a U-Slot patch antenna using dual-band frequency selective surface with double rectangular ring elements," *Microw. Opt. Technol. Lett.*, vol. 53, no. 7, pp. 1547-1553, July 2011.

[18] H. Y. Chen and Y. Tao, "Performance improvement of a U-slot patch antenna using a dual-band frequency selective surface with modified Jerusalem cross elements," *IEEE Trans. Antennas Propag.*, vol. 59, no. 9, pp. 3482-3486, Sep. 2011.

[19] D. Nashaat, H. A. Elsadek, E. A. Abdallah, M. F. Iskander, and H. M. El Hennawy, "Ultrawide bandwidth 2 2 microstrip patch array antenna using electromagnetic band-gap structure (EBG)," *IEEE Trans. Antennas Propag.*, vol. 59, no. 5, pp. 1528-1534, May 2011.

[20] B. A. Munk, R. J. Luebbers, and R. D. Fulton, "Transmission through a 2-layer array of loaded slots," *IEEE Trans. Antennas Propag.*, vol. AP22, no. 6, pp. 804-809, Nov. 1974.

[21] M. A. Hiranandani, A. B. Yakovlev and A. A. Kishk, "Artificial magnetic conductors realized by frequency-selective surfaces on a grounded dielectric slab for antenna applications," *IEE Pro.-Microw. Antennas Propag.,* vol. 153, no. 5, pp. 487-493, Oct. 2006.

[22] F. Yang and Y. Rahmat-Samii, "Reflection phase characterizations of the EBG ground plane for low profile wire antenna applications," *IEEE Trans. Antennas Propag*., vol. 51, no. 10, pp. 2691-2703, Oct. 2003.

[23] J. Liang and H. Y. David Yang, "Radiation characteristics of a microstrip patch over an electromagnetic bandgap surface," *IEEE Trans. Antennas Propag*., vol. 55, no. 6, pp. 1691-1697, June 2007.

[24] D. Sievenpiper, L. Zhang, R. F. Jimenez Broas, N. G. Alex´opolous, and E. Yablonovitch, "High-impedance electromagnetic surfaces with a forbidden frequency band," *IEEE Trans. Microwave Theory Tech.,* vol. 47, no. 11, pp. 2059-2074, Nov. 1999.

[25] Y. Zhang, J. von Hagen, M. Younis, C. Fischer, and W. Wiesbeck, "Planar artificial magnetic conductors and patch antennas," *IEEE Trans. Antennas Propag.,* vol. 51, no. 10, pp. 2704-2712, Oct. 2003.

[26] X. L. Bao, G. Ruvio, M. J. Ammann, and M. John, "A novel GPS patch antenna on a fractal hi-impedance surface substrate," *IEEE Antennas Wireless Propag. Lett.*, vol. 5, pp. 323-326, 2006.

[27] H. Mosallaei, and K. Sarabandi, "Antenna miniaturization and bandwidth enhancement using a reactive impedance substrate," *IEEE Trans. Antennas Propag.,* vol. 52, no. 9, pp. 2403-2414, Sep. 2004.

[28] R. F. J. Broas, D. F. Sievenpiper, and E. Yablonovitch, "A high-impedance ground plane applied to a cellphone handset geometry," *IEEE Trans. Microw. Theory Tech.,* vol. 49, no. 7, pp. 1262-1265, July 2001.

[29] A. P. Feresidis, G. Goussetis, S. Wang, and J. C. Vardaxoglou, "Artificial magnetic conductor surfaces and their application to low-profile high-gain planar antennas," *IEEE Trans. Antennas Propag.,* vol. 53, no. 1, pp. 209-215, Jan. 2005.

[30] H. Li, S. Khan, J. Liu, and S. He, "Parametric analysis of Sierpinski-like fractal patch antenna for compact and dual band WLAN applications," *Microw. Opt. Technol. Lett.*, vol. 51, no. 1, pp. 36-40, Jan. 2009.

[31] M. Hosseini and S. Bashir, "A novel circularly polarized antenna based on an artificial ground plane," *Progress Electromagn. Research Lett.*, vol. 5, pp. 13-22, 2008.

[32] S. Malisuwan, J. Sivaraks, N. Madan, and N. Suriyakrai, "Design of microstrip patch antenna for Ku-band satellite communication applications," *Int. J. Comput. Commun. Eng.*, vol. 3, no. 6, pp. 413-416, Nov. 2014.

[33] J. Wargo, *Unlicensed 24 GHz Point to Point Wireless Backhaul Option*, May 2010. [Online]. Available: http://www.aowireless.com

[34] SAF Tehnika JSC, *Highspeed Internet Provider Selects SAF Freemile 24 GHz to Extend Its Network in Hawaii*. Jun. 2012. [Online]. Available: http://www.openpr.com/news/226290/

[35] F. Alimenti, P. Mezzanotte, G. Tasselli, A. Battistini, V. Palazzari, and L. Roselli, "Development of low-cost 24-GHz circuits exploiting system-in-package SiP approach and commercial PCB technology," *IEEE Trans. Compon. Packag. Manuf. Technol.*, vol. 2, no. 8, pp. 1265-1274, 2012.

[36] M. Poggiani, F. Alimenti, P. Mezzanotte, M. Virili, C. Mariotti, G. Orecchini, and L. Roselli, "24-GHz patch antenna array on cellulose-based materials for green wireless internet applications," *IET Sci. Meas. Technol*., vol. 8, no. 6, pp. 342-349, 2014.

[37] H. Y. Chen, T. H. Lin, and P. K. Li, "Fast design of Jerusalem-cross parameters by equivalent circuit model and least-square curve fitting technique," *Appl. Comput. Electromagn. Soc. J.*, vol. 31, no. 4, pp. 455-467, 2016.

[38] H. Y. Chen and S. H. Wen, "An Empirical formula for resonant frequency shift due to Jerusalem-cross FSS with substrate on one side," *Appl. Comput. Electromagn. Soc. J.*, submitted, Nov. 16, 2016.

Shu-Huan Wen was born in Taiwan, in 1991. He received the B.S. degree in Electronic Engineering from Oriental Institute of Technology in 2013. He is currently working toward the Ph.D. degree in Communications Engineering at Yuan Ze University, Taiwan. His research interests include patch antenna design, frequency selective surfaces, EM field measurement, and computational electromagnetics.

Hsing-Yi Chen was born in Taiwan, in 1954. He received the B.S. and M.S. degrees in Electrical Engineering in 1978 and 1981 from Chung Yuan Christian University and National Tsing Hua University, respectively. He received the Ph.D. degree in Electrical Engineering from University of Utah, Salt Lake City, Utah in 1989. He joined the faculty of the Department of Electrical Engineering, Yuan Ze University, Taiwan, in September 1989. He was the Chairman of Electrical Engineering from 1996 to 2002, the Chairman of Communications Engineering from 2001 to 2002, the Dean of Engineering College from 2002 to 2006, the Dean of Electrical and Communication Engineering College from 2006 to 2012, and the Dean of Research and Development Office from 2012 to 2013. Currently, he is the Dean of General Affairs Office, Yuan Ze University. His current interests include electrostatic discharge, electromagnetic scattering and absorption, waveguide design, radar systems, electromagnetic compatibility and interference, bio-electromagnetics, electromagnetic radiation hazard protection, and applications of frequency selective surface.

He is a member of Phi Tau Phi. He was also a member of the editorial board of the *Journal of Occupational Safety and Health* from 1996 to 1997. He was elected an Outstanding Alumnus of the Tainan Second High School in 1995. He has been the recipient of numerous awards including the 1990 Distinguished Research, Service, and Teaching Award presented by the Yuan Ze University, the 1999 and 2002 YZU Outstanding Research Award, and the 2005 Y. Z. Hsu Outstanding Professor Award for Science, Technology & Humanity Category. He was awarded Chair Professor by Far Eastern Y. Z. Hsu Science and Technology Memorial Foundation in 2008. His name is listed in Who's Who in the World in 1998.

Null-Steering Beamformer Using Bat Algorithm

Tong Van Luyen [1] and Truong Vu Bang Giang [2]

[1] Faculty of Electronic Engineering
Hanoi University of Industry, Hanoi, 100000, Vietnam
luyen.tv@haui.edu.vn

[2] Faculty of Electronics and Telecommunications
VNU University of Engineering and Technology, Hanoi, 100000, Vietnam
giangtvb@vnu.edu.vn

Abstract ─ This paper proposes an adaptive null-steering beamformer based on Bat Algorithm (BA) for Uniform Linear Array (ULA) antennas to suppress the interference. The beamformer is targeted at steering nulls of ULA pattern in the directions of the interferences. The amplitude-only nulling method has been utilized for adjusting excitation weight of each array element. In order to validate the proposal, several scenarios of ULA array pattern imposed with the prescribed nulls have been investigated and compared with those of accelerated particle optimization (APSO) and genetic algorithm (GA). The proposed beamformer has shown the ability to suppress sidelobes and to place precisely single, multiple, and broad nulls at arbitrary interference directions. Furthermore, the beamformer is much faster and more effective than APSO and GA-based ones.

Index Terms ─ Array pattern synthesis, bat algorithm, beamformer, beamforming, interference suppression, null-steering, ULA antennas.

I. INTRODUCTION

Adaptive beamformers for smart antennas are widely applied in wireless communication systems to enhance the performance by increasing the effectiveness of radio spectrum utilizing, interference suppression, and saving power consumption. In order to obtain the desired pattern of the array, the beamformers create appropriate weights for array antenna elements [1].

Nowadays, the increasing number of wireless devices causes serious pollution in the electromagnetic propagation environment. In this context, smart antennas with null-steering capabilities emerge as promising solution for interference suppression in wireless communications and radar applications.

Several nulling methods such as controlling the amplitude-only, the phase-only, position-only, and the complex weights (both the amplitude and the phase) have been widely studied and implemented [1,2]. All of these methods have their own advantages and limitations.

Among those, the complex weights method has been considered as the most flexible and efficient one because it allows to adjust amplitude and phase simultaneously [3-6]. Nonetheless, it is the most complicated and expensive due to the fact that each array element must have controllers, phase shifters and attenuators. Especially, the computational time will be a considerable issue in large array antennas.

Indeed, the problem for the phase-only and position-only nulling methods is inherently nonlinear [7]. The position-only method [8-10] requires a mechanical driving system such as servomotors for adjusting the array element position. This makes the system more complicated, and has difficulty in accuracy control. Phase-only null synthesizing is less complex and more attractive for the phased arrays since the required controls are available at no extra cost, but it still has common problems [11-14].

The amplitude-only control [7], [15-17] is the simple method, compared to the others as it only changes the amplitude excited at each array element. Specifically, in the case of even number of elements that is symmetrical at the center of the array, the number of attenuators and the computational time will be reduced by half.

In recent years, optimization techniques have been widely applied in beamforming for antenna array pattern synthesis including null steering. The classical optimization techniques used for the array pattern synthesis are likely to be stuck in local minima if the initial guesses are not reasonably close to the final solution. Most of the classical optimization techniques and analytical approaches also suffer from the lack of producing flexible solutions for a given antenna pattern synthesis problem. To overcome these issues, various nature-inspired optimization algorithms based on computational intelligence approaches have been developed. These algorithms such as ant colony

Submitted On: February 4, 2017
Accepted On: October 12, 2017

optimization [5], bacterial foraging algorithm [7], differential evolution [16], clonal selection [17], bees algorithm [18], especially the genetic algorithm (GA) [2,6, 19-21] and particle swarm optimization (PSO) [20, 22,23] have been proved to be better and more flexible solutions than the classical techniques. These techniques have been proposed and implemented with their own benefits and limitations in the array pattern synthesis.

BA is a new nature-inspired computation technique based on the bat behavior of using echolocation to detect prey, avoid obstacles, and locate their roosting crevices in the dark. It has been successfully used to solve various kinds of engineering problems [24,25]. BA is better than PSO and GA optimization in terms of convergence, robustness and precision [24]. This algorithm has been applied for the first time for beamforming in [26]. The authors of [26] showed that the BA is a promising optimization tool for adaptive beamforming in terms of computation time. Nevertheless, this work was still in preliminary phase and thus, it lacked adequate analysis on the application of BA in beamforming.

In this paper, a beamformer based on BA is proposed for ULA antennas pattern synthesis with null-steering abilities. In our proposal, the amplitudes of excitation for array elements are the only controlling parameters, and the main aim is to synthesize array patterns with nulls imposed on directions of interferences. The proposed beamformer will be verified in five scenarios, and compared with accelerated particle swarm optimization (APSO) and GA-based ones. The results show that the beamformer operates well in terms of steering the nulls to interference directions, sidelobe suppression, and more efficiently than those of APSO and GA-based ones.

II. PROBLEM FORMULATION

Null-steering for interference suppression is achieved by adjusting the weights of array elements. Simultaneously, it is always desirable to keep the beamwidth and the peak sidelobe level (SLL) within a required level. This is realized by solving min optimization problem subjected to three constrains, namely, SLL limits, the prescribed location of the null points and acceptable broadening of the main lobe. The problem can be described as follows:

$$\begin{Bmatrix} min(|AF_o(\omega_n,\theta,d)|) & at\ \theta=\theta_i \\ min(|AF_o - AF_d|) & at\ \theta\neq\theta_i \end{Bmatrix}, \quad (1)$$

where: $AF(\omega_n,\theta,d)$ is the array factor, which is a function of weights (ω_n); θ is the elevation angle of incident wave with respect to the direction of the antenna array; and d is the distance between adjacent elements. AF_0 and AF_d are the optimization patterns obtained by using an optimization, which will be BA in this paper, and the desired pattern, respectively. θ_i are the angles of null points.

The ULA antenna of $2N$ isotropic elements is considered and presented in Fig. 1. The array is positioned symmetrically along the x axis, and the array factor can be expressed as:

$$AF(\theta) = \sum_{n=-N}^{N} \omega_n e^{jndksin(\theta)}, \quad (2)$$

where: $\omega_n = \omega_n^{re} + j\omega_n^{im}$, $\{n=(-N,\ldots,-2,-1,1,2,\ldots,N)\}$, is the complex weight of n^{th} array element; $k = \frac{2\pi}{\lambda}$ is the wave number; λ is wave length. In our study, the imaginary parts of weight (ω_n^{im}) are zero, and $\omega_{-n}^{re} = \omega_n^{re}$. Therefore, the weights are real and symmetrical around the center of the array. This means the number of attenuators and computation time are halved, and the array pattern is symmetrical around the main lobe at θ=0.

Since $\omega_n^{im} = 0$ and $sin\big(-ndksin(\theta)\big) = -sin\big(ndksin(\theta)\big)$, the array factor in (1) can be rewritten as:

$$AF(\theta) = 2\sum_{n=1}^{N} \omega_n^{re} \cos\big(ndksin(\theta)\big). \quad (3)$$

According to (3), the array factor is symmetrical around the center of the array (or about theta angle θ=0).

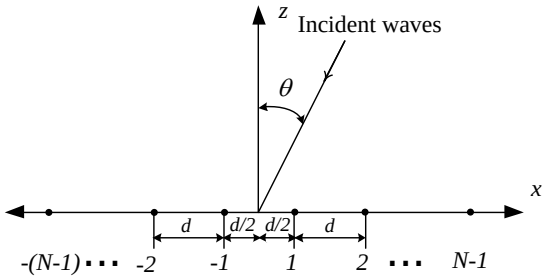

Fig. 1. Geometry of ULA antennas of 2N elements.

For the investigated ULA, to put a null at a given angle θ_i, we need [3]:

$$AF(\theta_i) = W^T v(\theta_i) = 0, \quad (4)$$

where: W is $N\times1$ vector, which is defined as:

$$W = [\omega_{-N}, \omega_{-(N-1)}, \ldots, \omega_{N-1}, \omega_N]^T,$$

and

$$v(\theta_i) = \begin{bmatrix} e^{-jNdksin(\theta)} \\ e^{-j(N-1)dksin(\theta)} \\ . \\ . \\ . \\ e^{j(N-1)dksin(\theta)} \\ e^{jNdksin(\theta)} \end{bmatrix}_{N\times1}.$$

Additionally, inspired by the objective function implemented previously in [7,27], a new objective function F, which meets the requirements in (1), has been developed as follows:

$$F_1 = \sum_{\theta=-90^0}^{90^0} [|AF_o(\theta) - AF_d(\theta)|^2],\ with\ \theta \neq \theta_i, \quad (5)$$

$$F_2 = \sum_{i=1}^{I} [|AF_o(\theta_i)|^2], \quad (6)$$

where: F_1 is used to reduce SLL and to keep beamwidth of main lobe within a maximum allowable change; F_2 is for placing the null points.

The objective function F has been built from F_1 and F_2 as follows:

$$F = \begin{cases} N(\theta)F_2, & \text{for } \theta = \theta_i \\ F_1, & \text{elsewhere} \end{cases}, \quad (7)$$

where: $N(\theta)$ is a parameter, which is defined by simulations during the investigation of the proposal (see Section IV).

III. PROPOSAL OF THE BEAMFORMER

A. Bat algorithm

The Bat algorithm is a new swarm intelligence optimization method developed by Yang in 2010 [24], in which the fundamental principle is inspired by the social behavior of bats and the phenomenon of echolocation to sense distance.

In BA [24,25], each bat (i) is defined by its position x_i^t, velocity v_i^t, frequency f_i, loudness A_i^t, and the emission pulse rate r_i^t in a d-dimensional search space. The new solutions x_i^t and velocities v_i^t at time step t are given by:

$$\begin{aligned} f_i &= f_{min} + (f_{max} - f_{min})\beta, \\ v_i^t &= v_i^{t-1} + (x_i^t - x_*)f_i, \\ x_i^t &= x_i^{t-1} + v_i^t, \end{aligned} \quad (8)$$

where $\beta \in [0,1]$ is a random vector drawn from a uniform distribution. Here x_* is the current global best location (solution) which is located after comparing all the solutions among all n bats. Frequency range is defined by f_{min} and f_{max}, which are chosen depending on the domain size of the problem of interest. Initially, each bat is randomly given a frequency which is drawn uniformly from $[f_{min}, f_{max}]$. For the local search part, once a solution is selected among the current best solutions, a new solution for each bat is generated locally using random walk as:

$$x_{new} = x_{old} + \varepsilon A^t, \quad (9)$$

where $\varepsilon \in [0,1]$ is a random number, while A^t is the average loudness of all the bats at time step t.

Furthermore, in consecutive iterations, the loudness A_i and the rate r_i of emission pulse can be updated by:

$$A_i^{t+1} = \alpha A_i^t, \quad (10)$$

$$r_i^{t+1} = r_i^0[1 - \exp(-\gamma t)], \quad (11)$$

where $0<\alpha<1$ and $0<\gamma$ are constants.

B. Bat algorithm based beamformer

The basic principle of the beamformers has been presented in [28]. Additionally, in our previous papers [29-31], the adaptive beamformer for ULA antennas with detailed design and verification procedure has been given. Inspired by these beamfomers and BA, a null-steering beamformer for interference suppression is being proposed and presented in Fig. 2. Operation of the beamformer is described as follows.

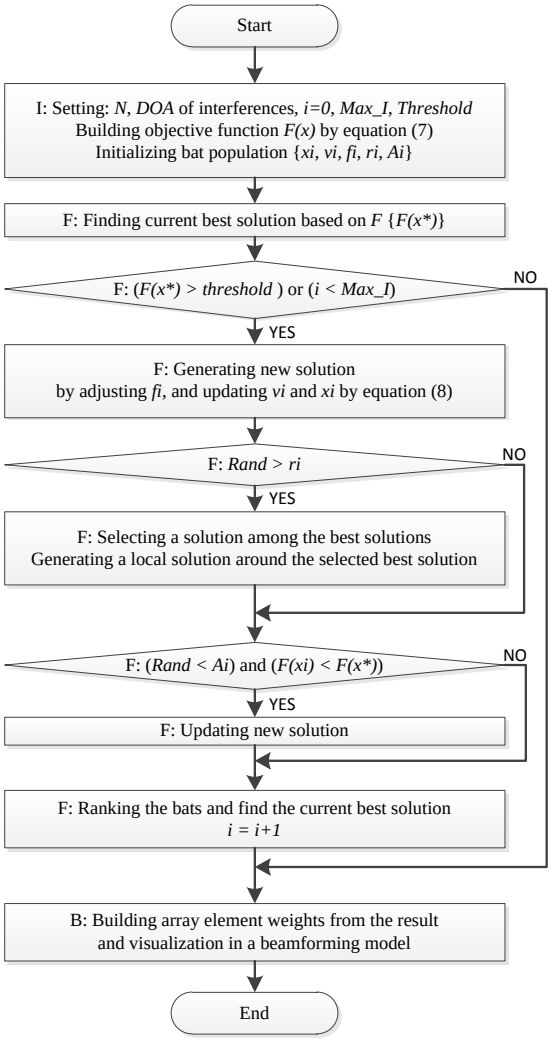

Fig. 2. Flowchart of the proposed beamformer.

Initializations (I):

- Setting the input data such as: number of array elements (N), Direction of Arrival (DOA) of interferences; number of iteration (i); maximum number of iterations (Max_I); and the termination criterion ($Threshold$).
- Initializing bat population in which parameters of each bat are: location x_i; velocity v_i; pulse frequency f_i; pulse rate r_i; and loudness A_i. Each bat is corresponding to a

potential solution.

Finding the best solution (F):

- The beamformer consecutively calculates and searches for the current best solution based on the BA. The operation is finished when the termination criterion or maximum number of iterations is satisfied. Then, the final best solution is obtained.

Building of the amplitude of excitations for array elements (B):

- From the best solution, the beamformer calculates the corresponding amplitude excited at each element of ULA antenna. These parameters will be used for null-steering.

IV. NUMERICAL RESULTS

To demonstrate the capability and flexibility of the proposal for sidelobe suppression and null steering, five scenarios will be investigated. It is well-known that the Chebyshev array weights distribution produces the optimum pattern in terms of tradeoff between the sidelobe level and the first-null beamwidth of main lobe for equally spaced arrays [32]. Therefore, in this paper, array factor of Chebyshev array has been chosen as a desired one to control the sidelobe level and the beamwidth. A -30 dB Chebyshev array pattern for 20 isotropic elements with $\lambda/2$ inter-element spacing has been utilized as the initial pattern.

The initial parameters for BA have been chosen for all investigation scenarios as: population size is 1000 and number of iterations is 20 (except for the first scenarios); step size of random walk is 0.01; boundary frequency values: f_{min}=0 and f_{max}=1; search value x_i in the range of 0 to 1; $A = r = 0.5$.

Parameters for GA: selection rate: 50%; mutation rate: 20%; crossover type: roulette wheel; crossover rate: 90%; and elitism: 1.

Due to the simplicity and improved convergence speed, APSO by Yang [25] has been considered as a good choice, and the parameters have been chosen as $\alpha = 0.2$ and $\beta = 0.5$ [23,25].

The values of the objective function parameters given in Equation (7) are selected as follows:

$$AF_d = \begin{cases} 0, & \text{for } \theta = \theta_i \\ \text{Initial pattern}, & \text{elsewhere} \end{cases}, \quad (12)$$

$$N(\theta) = \begin{cases} 10000, & \text{for } \theta = \theta_i \\ 1, & \text{otherwise} \end{cases}. \quad (13)$$

In order to show the ability of our proposed beamformer for interference suppression, five scenarios have been built as Convergence Characteristics, Single Null, Multiple Nulls and Broad Null. The simulation results of all scenarios have been compared and presented in Figs. 3-7, in which the results are averaged values of Monte Carlo simulations with 1000 times for the first scenario, and 100 times for the others.

A. Convergence characteristics

In the first scenario, convergence rate of the proposed beamformer has been investigated and compared with those of APSO and GA-based ones. In order to do that, these beamformer have been applied to obtain the desired optimization pattern as -30 dB Chebyshev array pattern. Additionally, the initial population has been randomly generated, number of iteration is 100. Their convergence rates have been illustrated in Fig. 3. It can be seen that BA-based beamformer converges much faster than APSO and GA-based ones.

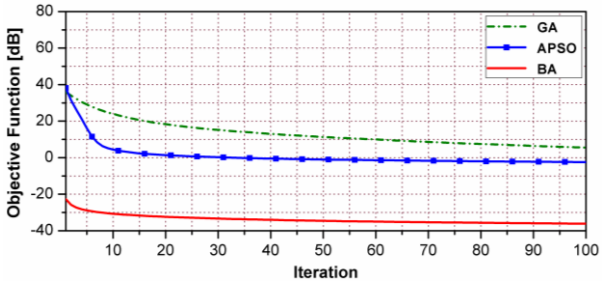

Fig. 3. Objective function comparisons of BA, APSO, and GA.

B. Single null

In the second scenario, the optimized patterns with single null have been demonstrated. This null is arbitrarily set at any angle, which is chosen at peak of the second sidelobe (14^0) in this test case. The population has been initialized as -30 dB Chebyshev array weights. As shown in Fig. 4, the optimized pattern by the proposed beamformer (BA pattern) preserves almost characteristics of the initial Chebyshev pattern such as approximately equal half power beam width (HPBW = $7,64^0$) and sidelobe level (-30 dB) except for first sidelobe level of -27 dB and the nulling location (θ_i=14^0) of -90.6 dB. It should be noted that a symmetric null is also observed at θ_i = -14^0 due to the symmetry of the array factor in (3). Additionally, the single null pattern optimized by our proposal is better than that of APSO and GA in the context of null depth level (NDL).

C. Multiple nulls

In the third scenario, the optimized patterns imposed with multiple nulls, which are set at 14^0, 26^0, and 33^0 corresponding to the peaks of the second, the fourth and the fifth sidelobe next to the main lobe of Chebyshev array pattern, has been given in Fig. 5. It can be seen that the nulls of optimized pattern have been exactly obtained at the predefined locations. All the NDLs are deeper than -71 dB and most sidelobe levels are nearly equal to that of Chebyshev pattern excluding the first and second sidelobe (maximum SLL is -20.5 dB). The BA pattern shows advantages over the APSO and GA patterns in

terms of NDL and SLL.

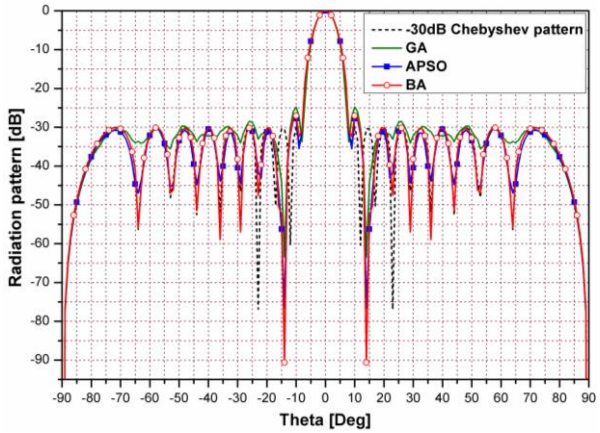

Fig. 4. Optimized pattern with single symmetric null at 14^0.

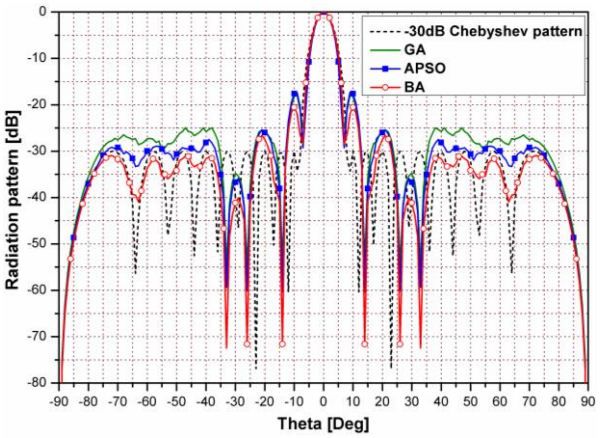

Fig. 5. Optimized patterns with three symmetric multiple nulls at 14^0, 26^0, and 33^0.

D. Broad null

In interference suppression application, if the directions of arrival of undesired interferences vary slightly with time or not be known exactly, or a null is continuously steered for obtaining an appropriate signal-to-noise ratio, a broad null is required. To give a demonstration of broad interference suppression capability, in the fourth scenario, the pattern with an imposed broad null locating at 35^0 with angular width ($\Delta\theta_i = 30^0$) has been obtained and illustrated in Fig. 6. It can be observed that a broad null (minimum NDL < -63 dB) on the BA pattern at the target sector has been obtained. The beamwidth stays the same without significant changes, and maximum SLL is -18.3 dB. According to the results, the BA pattern surpasses the APSO and GA ones in terms of NDL.

In all of the above scenarios, the null points of the patterns have been set accurately and the beamwidths have been approximately preserved. Notwithstanding this, SLLs were bigger than -30 dB. To hold maximum SLL at a predefined value (for example, -30 dB) and a symmetric broad null at the target sectors of [20^0, 50^0] as well, the fifth scenario has been conducted, in which AF_d has been substituted by the array factor of Chebyshev array with SLL of -49 dB. Optimized patterns have been shown in Fig. 7.

There exists a trade-off between the SLL and the beamwidth of the patterns, which possess maximum SLL of -30 dB and a broadened HPBW.

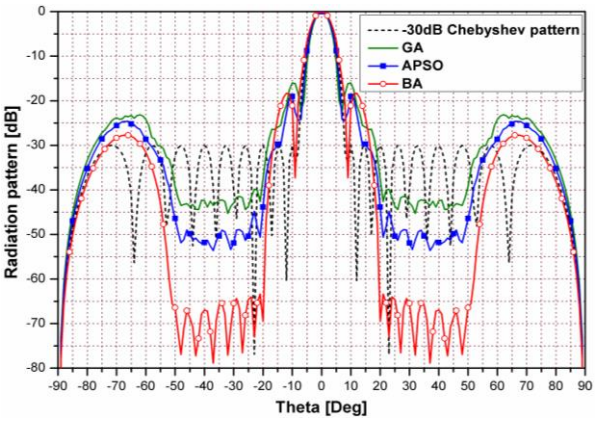

Fig. 6. Optimized patterns with a symmetric broad null from 20^0 to 50^0, unchanged main lobe and maximum SLL = -18.3 dB.

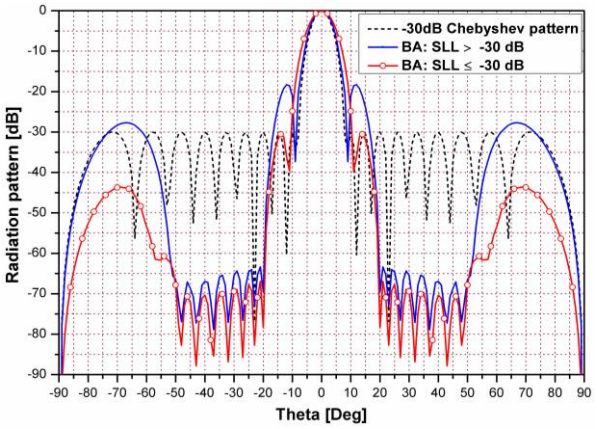

Fig. 7. Optimized pattern with a symmetric broad null from 20^0 to 50^0, broadened main lobe and SLL ≤ -30 dB.

V. CONCLUSION

In this paper, a BA-based beamformer has been proposed for adaptive steering nulls of ULA antennas patterns. The nulls steering capability of the beamformer has been verified by five scenarios including operation speed, null steering with single, multiple and broad nulls. The results show that the above mentioned nulls can be precisely imposed to arbitrary interference directions

using our proposed beamformer, while the patterns have maintained the HPBW and low SLL. Furthermore, compared with APSO and GA-based beamformers, our proposal is more efficient in terms of operation speed and adaptive null steering in array pattern synthesis.

ACKNOWLEDGEMENTS

This work has been partly supported by Vietnam National University, Hanoi (VNU), under Project No. QG. 16.27.

REFERENCES

[1] H. L. Van Trees, *Optimum Array Processing: Part IV of Detection, Estimation, and Modulation Theory*. chap. 1, pp. 1-12, John Wiley & Sons, 2002.

[2] R. L. Haupt, *Antenna Arrays: A Computational Approach*. chap. 8, sec. 8.4, pp. 484-515, John Wiley & Sons, 2010.

[3] H. Steyskal, R. A. Shore, and R. L. Haupt, "Methods for null control and their effects on the radiation pattern," *IEEE Trans. Antennas Propagat.*, vol. 34, pp. 404-409, 1986.

[4] K. Guney and A. Akdagli, "Null steering of linear antenna arrays using modified tabu search algorithm," *Progress In Electromagnetics Research*, vol. 33, pp. 167-182, 2001.

[5] D. Karaboga, K. Guney, and A. Akdagli, "Antenna array pattern nulling by controlling both the amplitude and the phase using modified touring ant colony optimisation algorithm," *Int. J. Electronics*, vol. 91, pp. 241-251, 2004.

[6] Y. Lu and B. K. Yeo, "Adaptive wide null steering for digital beamforming array with the complex coded genetic algorithm," *IEEE Int. Conf. Phased Array Systems and Technology*, Dana Point CA, USA, pp. 557-560, 2000.

[7] K. Guney and S. Basbug, "Interference suppression of linear antenna arrays by amplitude-only control using a bacterial foraging algorithm," *Progress In Electromagnetics Research*, vol. 79, pp. 475-497, 2008.

[8] D. I. Abu-Al-Nadi, T. H. Ismail, and M. J. Mismar, "Interference suppression by element position control of phased arrays using LM algorithm," *Int. J. Electron. Commun.*, vol. 60, pp. 151-158, 2006.

[9] A. Akdagli, K. Guney, and D. Karaboga, "Pattern nulling of linear antenna arrays by controlling only the element positions with the use of improved touring ant colony optimization algorithm," *Journal of Electromagnetic Waves and Applications*, vol. 16, pp. 1423-1441, 2002.

[10] K. Guney and M. Onay, "Bees algorithm for null synthesizing of linear antenna arrays by controlling only the element positions," *Neural Network World*, vol. 16, pp. 153-169, 2007.

[11] R. A. Shore, "Nulling at symmetric pattern location with phase only weight control," *IEEE Trans. Antennas Propagat.*, vol. 32, pp. 530-533, 1984.

[12] A. Akdagli and K. Guney, "Null steering of linear antenna arrays by phase perturbations using modified tabu search algorithm," *J. Communications Technology and Electronics*, vol. 49, pp. 37-42, 2004.

[13] M. Mouhamadou, P. Vaudon, and M. Rammal, "Smart antenna array patterns synthesis: Null steering and multi-user beamforming by phase control," *Progress In Electromagnetics Research*, vol. 60, pp. 95-106, 2006.

[14] M. Mouhamadou, P. Armand, P. Vaudon, and M. Rammal, "Interference supression of the linear antenna arrays controlled by phase with use of SQP algorithm," *Progress In Electromagnetics Research*, vol. 59, pp. 251-265, 2006.

[15] N. Karaboga, K. Guney, and A. Akdagli, "Null steering of linear antenna arrays by using modified touring ant colony optimization algorithm," *Int. J. RF and Microwave Computer Aided Eng.*, vol. 12, pp. 375-383, 2002.

[16] S. W. Yang, Y. B. Gan, and A. Y. Qing, "Antenna-array pattern nulling using a differential evolution algorithm," *Int. J. RF and Microwave Computer Aided Eng.*, vol. 14, pp. 57-63, 2004.

[17] B. Babayigit, A. Akdagli, and K. Guney, "A clonal selection algorithm for null synthesizing of linear antenna arrays by amplitude control," *Journal of Electromagnetic Waves and Applications*, vol. 20, pp. 1007-1020, 2006.

[18] K. Guney and M. Onay, "Amplitude-only pattern nulling of linear antenna arrays with the use of bees algorithm," *Progress In Electromagnetics Research*, vol. 70, pp. 21-36, 2007.

[19] J. Jin, H. L. Wang, W. M. Zhu, and Y. Z. Liu, "Array patterns synthesizing using genetic algorithm," *Progress In Electromagnetics Research Symposium*, Cambridge, USA, pp. 64-68, 2006.

[20] D. W. Boeringer and D. H. Werner, "Particle swarm optimization versus genetic algorithms for phased array synthesis," *IEEE Trans. Antennas Propagat.*, vol. 52, pp. 771-779, 2004.

[21] M. R. Khan and V. Tuzlukov, "Null steering beamforming for wireless communication system using genetic algorithm," *2011 IEEE International Conference on Microwave Technology & Computational Electromagnetics*, Beijing, pp. 289-292, 2011.

[22] K. C. Lee and J. Y. Jhang, "Application of particle swarm algorithm to the optimization of unequally spaced antenna arrays," *Journal of Electromagnetic Waves and Applications*, vol. 20, pp. 2001-2012, 2006.

[23] P. V. Florence and G. S. N. Raju, "Synthesis of

linear antenna arrays using accelerated particle swarm optimization algorithm," *Int. J. Computer Applications*, vol. 103, no. 3, pp. 43-49, 2014.
[24] X. S. Yang, "A new metaheuristic Bat-inspired algorithm," *Studies in Computational Intelligence*, vol. 284, pp. 65-74, 2010.
[25] X. S. Yang, *Nature-Inspired Optimization Algorithms*. London: Elsevier, pp. 141-154, 2014.
[26] Q. Yao and Y. Lu, "Efficient beamforming using bat algorithm," *2016 IEEE MTT-S Int. Con. on Numerical Electromagnetic and Multiphysics Modeling and Optimization (NEMO)*, July 2016.
[27] S. U. Khan, I. M. Qureshi, F. Zaman, and A. Naveed, "Null placement and side lobe suppression in failed array using symmetrical element failure technique and hybrid heuristic computation," *Progress In Electromagnetics Research B*, vol. 52, pp. 65-184, 2013.
[28] J. Litva and T. Kwok-Yeung Lo, *Digital Beamforming in Wireless Communications*. chap. 2-3, pp. 13-55, Artech House, 1996.
[29] T. V. Luyen and T. V. B. Giang, "Proposal of beamformer hardware model for smart antennas," *in Proc. of The 2014 National Conference on Electronics, Communications and Information Technology*, Nha Trang, pp. 190-193, Sep. 2014.
[30] T. V. Luyen and T. V. B. Giang, "Design and implementation of FPGA based LMS adaptive beamformer for ULA antennas," *in Proc. of The Vietnam Japan Microwave 2015*, Ho Chi Minh City, pp. 71-76, Aug. 2015.
[31] T. V. Luyen and T. V. B. Giang, "Design of LMS based adaptive beamformer for ULA antennas," *VNU Journal of Science: Comp. Science & Com. Eng.*, vol. 32, no. 3, pp. 72-79, 2016.
[32] C. L. Dolph, "A current distribution for broadside arrays which optimizes the relationship between beam width and side-lobe level," *Proc. IRE*, vol. 34, pp. 335-348, June 1946.

Tong Van Luyen is a Lecturer at Faculty of Electronic Engineering, Hanoi University of Industry. He received the B.S. and M.S. degree from the Hanoi University of Science and Technology, in 2002 and 2004, respectively. He is now a Ph.D. student at Faculty of Electronics and Telecommunications, University of Engineering and Technology, VNU.

His research interests are in Digital Beamforming and Beamsteering for Smart Antennas, Nature Inspired Optimization.

Truong Vu Bang Giang was born in Hanoi, Vietnam, in 1973. He received the B.S. and M.S. degree from the VNU-University of Sciences,in 1994 and 1997, respectively, and the Dr.-Ing. (Ph.D.) degree in Electrical Engineering from the Hamburg-Harburg University of Technology, Hamburg, Germany, in 2006.

From 1997 to 2002, he was a Research Assistant at the Faculty of Electronics and Telecommunications, VNU-University of Sciences then at the Faculty of Engineering of Vietnam National University, Hanoi.

From 2002 to 2006, he did his Ph.D. and then worked as a Development Engineer at the Institute of Communications and Navigation, German Aerospace Center (DLR), Oberpfaffenhofen, Germany.

From 2006 to 2015, he worked at VNU-University of Engineering and Technology, where he was the Vice Head of the Division for Science, Technology and Graduate Study (2006-2009) and the Dean of the Faculty of Faculty of Electronics and Telecommunications (2009-2015).

Since May 2015, he has been appointed as the Deputy Director of Science and Technology Department of Vietnam National University, Hanoi and as the Secretary of the National Research Program for Sustainable Development of North-West Region of Vietnam.

He is currently the Vice President of Radio Electronics Association of Vietnam; Member of IEEE MTTs and APS. He has served as the Steering Committee (Co-Chair), Organizing Committee (Chair and Co-Chairs) or Technical Committee of ATC, REV-ECIT, VJMW, VJISAP conferences in Vietnam; Scientific and Technical Committee, International Transaction Journal of Engineering, Management, & Applied Sciences & Technologies (Thailand); Editorial Board, VNU Journal of Science: Computer Science and Communication Engineering (JCSCE).

His current research interests include Microstrip Antennas for Mobile and Handheld Devices; Analysis and Design of Conformal Antennas; Digital Beamforming and Beamsteering for Smart Antennas; Metamaterial Antennas; Design of RF Devices and Systems.

A Compact Triple-Band Notched MIMO Antenna for UWB Systems

Ling Wu, Yingqing Xia, and Xia Cao

College of Physical Science and Technology, Huazhong Normal University
No. 152 Luoyu Road, Wuhan, Hubei 430070, People's Republic of China

Abstract ─ A miniaturization ultra-wideband (UWB) multiple-input-multiple-output (MIMO) antenna with triple-notched band function is presented in the paper. There are two similar monopole radiators in the UWB-MIMO system. Based on half-cutting method, the system only occupies 21×27 mm^2. Three inverted L-shaped slots are inserted to get three rejected bands for suppressing interference from 3.5 GHz WiMAX, 5.5 GHz WLAN, and 8.1 GHz X-band. With a T-shaped stub extruding from the ground plane, both impedance bandwidth and port isolation are effectively improved. The proposed antenna covers operating frequency band of 3.1-11 GHz except three notched bands, and has a low port isolation of better than -20 dB. Moreover, good radiation patterns, stable gain and low envelope correlation coefficient (ECC) also ensure that the designed antenna is helpful in UWB systems.

Index Terms ─ Half-cutting method, monopole antenna, multiple-input-multiple-output (MIMO), notched band, ultra-wideband (UWB).

I. INTRODUCTION

UWB technology has attracted heated discussion since FCC (Federal Communications Commission) permitted 3.1-10.6 GHz for UWB applications in 2002 [1]. Monopole antennas have many advantages of low profile, compact volume and easy manufacture and the like. However, there are some difficulties in antenna design, of which frequency interference is the main challenge. Some systems frequencies working in 3.1-10.6 GHz may severely affect UWB applications, like WiMAX (3.3-3.7 GHz), WLAN (5.15-5.825 GHz), and X-band (7.7-8.5 GHz). Design multiple band notched UWB antenna is a useful means to mitigate these interferences. The second challenge is multipath fading. As MIMO technology can significantly enhance the capacity of the system and resist multipath fading, it has become a hot spot in the field of wireless communication [2]. For above reasons, design UWB-MIMO antennas with multiple notched bands and low mutual coupling is promising.

In recent years, many reports about multiple notched bands for UWB systems have been discussed, such as inserting various structures (folded stepped-impedance resonators [3], CSRR structure [4], arc-shaped slots [5]). However these multiple notched-band antennas have a big size [3-5]. With half-cutting method [6,7], size of antenna can be reduced a lot. A LTCC antenna with compact size of 17×10 mm^2 was proposed [6]. And the dimension of antenna was decreased from 40×40 mm^2 to 10×20 mm^2 [7].

Recently, some technologies about improving port isolation of UWB-MIMO antennas have been reported [8-14]. [8] applied a tree-like decoupling element to get isolation of less than -16 dB. [9] adopted a sine-curve based nested T-shaped structure to obtain -20 dB port isolation. Neutralization lines were used in [10] to obtain isolation more than 22 dB. [11] introduced a rectangle stub as a decoupling structure to achieve -15 dB isolation. A T-shaped strip was placed between two radiators to alleviate mutual coupling [12]. Metal strips also can be applied to reduce isolation [13]. Without decoupling elements, two antennas were arranged vertically in [14] and high isolation of -20 dB was easily achieved.

Based on half-cutting method, a miniaturization triple band-notched UWB-MIMO antenna is introduced in the article. The whole size of the UWB-MIMO antenna is 21×27 mm^2 = 567 mm^2. Extruding a T-shaped stub on the back side, both impedance bandwidth and isolation are improved, which is the highlight of the design. Some decoupling elements in reports are just used to increase isolation, such as the decoupling structure in [8-12]. With inserting three inverted L-shaped slots on each radiator, triple notched bands are achieved for filtering 3.5 GHz WiMAX, 5.5 GHz WLAN, and 8.1 GHz X-band. Only one type of filter element with simple structure is adopted, so it is easy to adjust notched bands, which is another advantage of the design. Simple structure, triple-band notched characteristic and low mutual coupling make the antenna meaningful in UWB applications.

II. ANTENNA DESIGN

A. Configurations

The configuration of the UWB-MIMO antenna is exhibited in Fig. 1 (a). The system is etched on a 21×27×0.8 mm^3 FR4 substrate with dielectric constant

Submitted On: December 13, 2016
Accepted On: November 29, 2017

ε_r=4.4, loss tangent of 0.025. There are two identical monopole radiators in the system. Each radiator comprises a rectangular radiating patch with a beveled edge which is helpful for wider impedance bandwidth. A 50 ohm microstrip line of dimension Lf × wf is used for feeding each radiator. Three inverted L-shaped slots, labeled with Slot 1, Slot 2, Slot 3, are inserted in each radiator to mitigate 8.1 GHz X-band, 5.5 GHz WLAN and 3.5 GHz WiMAX separately. A T-shaped stub is extruded from the middle of the back ground, which is used to broaden impedance bandwidth and improve isolation.

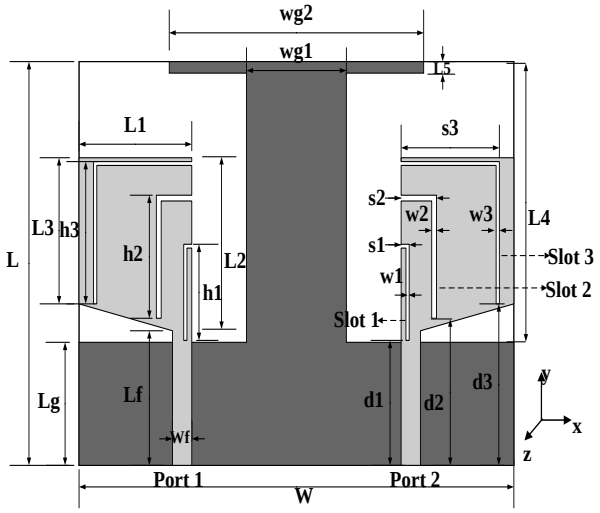

(a)

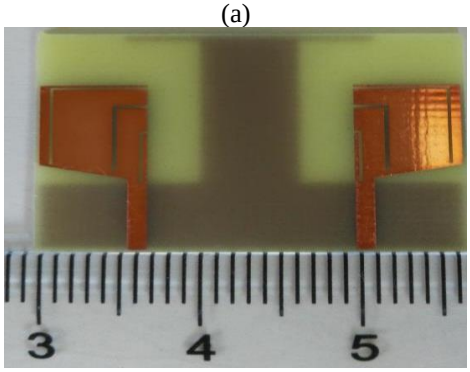

(b)

Fig. 1. (a) Schematic of proposed antenna, and (b) manufactured prototype.

In the design, total length of each inverted L-shaped slot is set to quarter of guided wavelength λ_g:

$$L = \frac{\lambda_g}{4} = \frac{c}{4f_c\sqrt{\varepsilon_{eff}}}, \quad (1)$$

where c denotes light speed, f_c is center frequency of corresponding notched band and,

$$\varepsilon_{eff} = \frac{(\varepsilon_r + 1)}{2} + \frac{(\varepsilon_r - 1)}{2}[1 + 12\frac{h}{W}]^{-1/2},$$

is effective dielectric constant.

Table 1 lists calculated L and simulated values. By comparison, the two are very close, which guarantees the design correctness.

Table 1: Calculated and simulated values

L	f_c (GHz)	Calculated Value (mm)	Simulated Value (mm)
L_1	3.5	11.1	13.3
L_2	5.5	7	8.3
L_3	8.1	4.8	5.3

CST Microwave Studio is applied in all simulations. The optimum parameters are obtained as follows (Unit: mm):

W=27, L=21, Lg=6.4, Lf=7, Wf=1.2, L1=7, L2=9, L3=7.6, L4=14, L5=0.6, wg1=6.2, wg2=15.8, s1=0.5, w1=0.2, h1=4.8, d1=6.5, s2=2.2, w2=0.3, h2=6.1, d2=7.65, s3=6.1, w3=0.2, h3=7.2, d3=8.4. As shown in Fig. 1 (b), a prototype was fabricated according to the above parameters.

B. Effect of the T-shaped stub

Figure 2 shows evolution of the ground plane. In the initial design, only a partial ground plane is applied, which is shown in Fig. 2 (a). In Fig. 2 (b), a T-shaped stub is added to the ground. The effects of the T shape ground on the antenna with and without those slots are shown in Fig. 3 and Fig. 4.

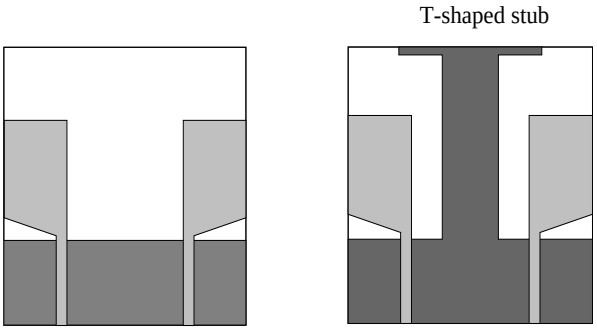

(a) Ant-1 (b) Ant-2

Fig. 2. Design evolution of the ground plane: (a) Ant-1 and (b) Ant-2.

Figure 3 plots S-parameters for the above antennas which named Ant-1, Ant-2, respectively. Due to symmetry of Port 1 and Port 2, only S11 and S21 are studied for simplicity. As plotted in Fig. 3 (a), without the T-shaped stub, the value of S11 is less than -10 dB from 5.5 to 11 GHz for Ant-1. For Ant-2, after adopting the T-shaped stub, a response is generated at 3.4 GHz. Thus, Ant-2 has a much lower frequency than Ant-1. And then the

proposed antenna can cover 3.1-11 GHz UWB band. In Fig. 3 (b), at low frequency band, the value of S21 is above -15 dB for Ant-1. However, it is less than -15 dB for Ant-2. So the T-shaped stub improves isolation.

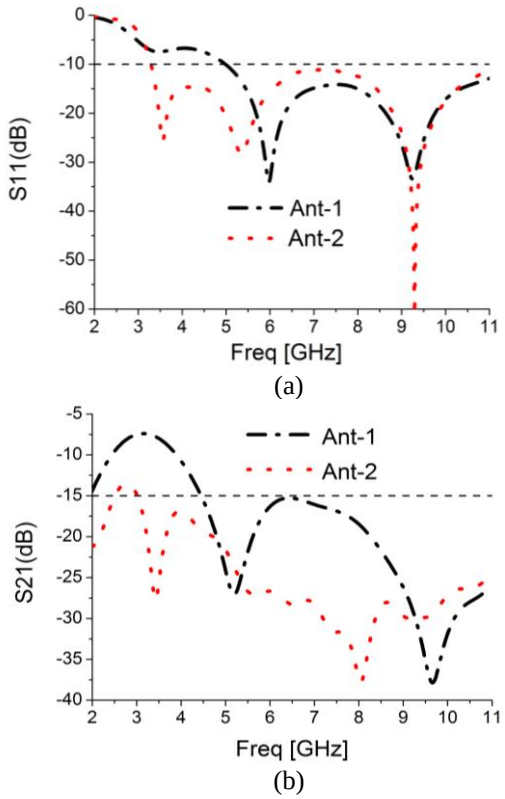

Fig. 3. (a) Simulated S11and (b) simulated S21.

Figure 4 shows surface current distributions at 4.5 GHz with/without the T-shaped stub and with/without three slots when Port1 is excited. From Fig. 4 (a), a lot of electric current is coupled to Port 2 without the stub. By contrast, with the stub, as shown in Fig. 4 (b), a large part of current is stopped from flowing to Port 2, and port isolation is greatly improved. The phenomenon of current tendency in Fig. 4 (c) is similar to Fig. 4 (a), and Fig. 4 (d) is similar to Fig. 4 (a). Whether or not there are slots on the patch, the T-shaped stub can reduce coupling. Figure 3 and Fig. 4 demonstrate that the T-shaped stub is not only used to broaden -10 dB impedance bandwidth, but also to reduce coupling.

C. Effects of inverted L-shaped slots (Slot 1, Slot 2, and Slot 3)

Figure 5 exhibits the effect of h3, h2, and h1 on S11, respectively. When one parameter is varied, the others are fixed. The effect of different h3 on S11 is plotted in Fig. 5 (a). When h3 grows from 7 to 7.4 mm, the length of Slot 3 becomes larger. The first notched band (denoted as NB) shifts slightly to the left, which can be deduced by formula (1). As Fig. 5 (b) shows, the second NB moves from 5.7 GHz to 5.3 GHz when the length of Slot 2 (h2) increases from 5.9 to 6.3 mm. In Fig. 5 (c), adjusting h1 from 4.6 mm to 5 mm, the length of Slot 1 is increased. Central frequency of the third NB is decreased from 8.5 GHz to 7.6 GHz. From Fig. 5, it also can be observed that when one NB was controlled, the other NBs keep almost unchanged. Thus, each NB can be adjusted individually.

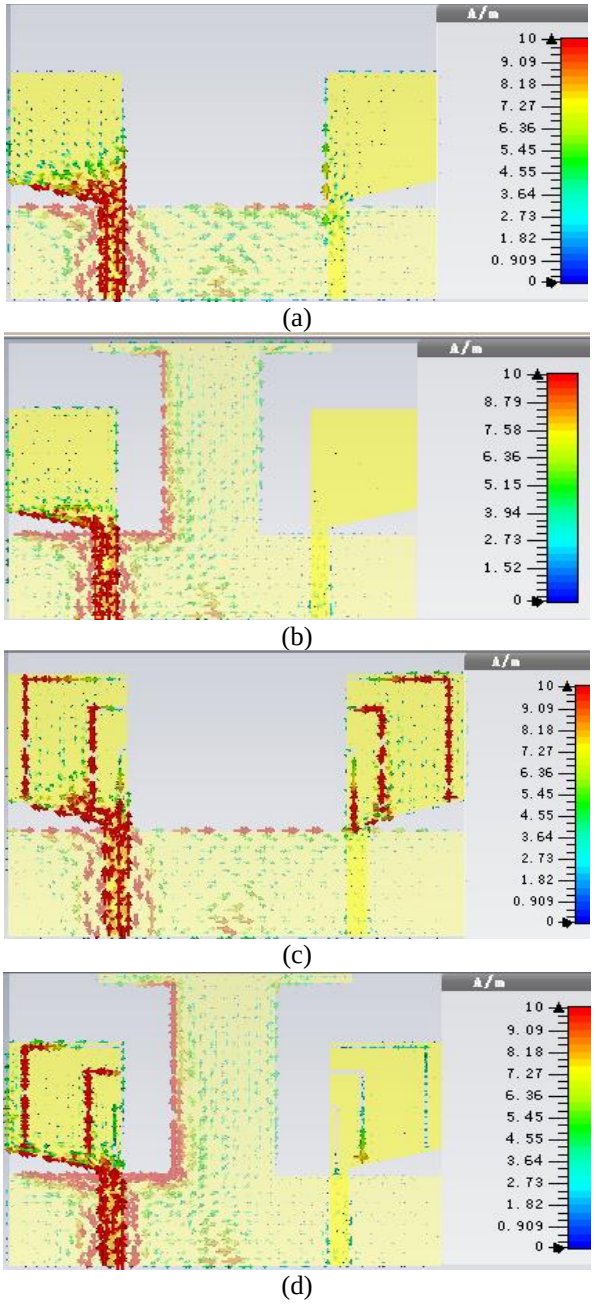

Fig. 4. Surface current distributions at 4.5 GHz: (a) without T-shaped stub, (b) with T-shaped stub, (c) with three slots and without T-shaped stub, and (d) with three slots and T-shaped stub.

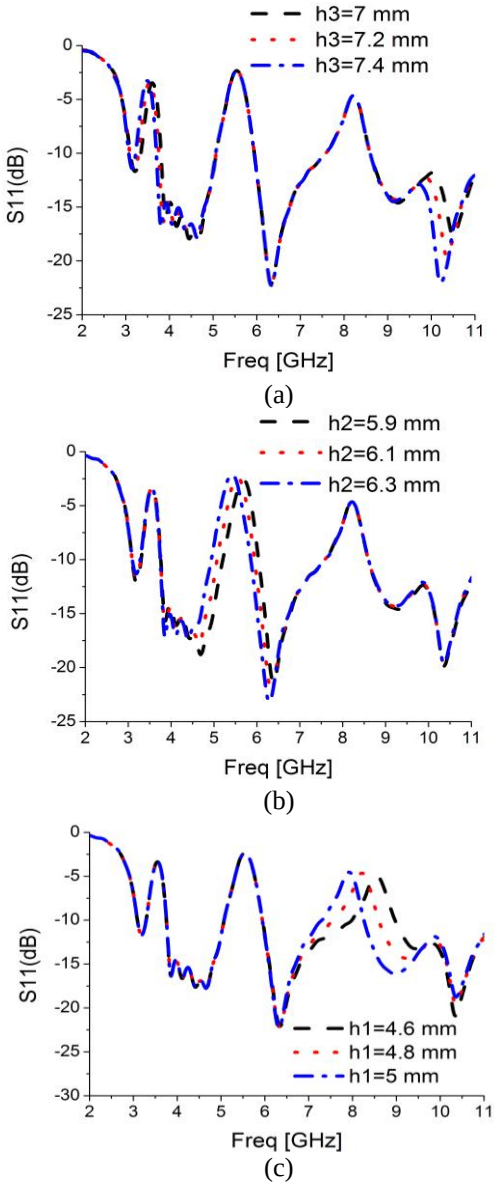

Fig. 5. Simulated S11: (a) effect of h3, (b) effect of h2, and (c) effect of h1.

Surface current distributions on the antenna at 3.5, 5.5, and 8.1 GHz are shown in Fig. 6, which help us to better understand the formation mechanism of rejected bands. From Fig. 6, at notched frequencies, strong electric current concentrates around the corresponding slot, which demonstrates that the slots play important role in the formation of NBs. Moreover, with the increase of the distance away from the feeding point, weaker current is appeared on the slots. At the top of the slots, weakest current and highest impedance is observed. These slots can be considered as a quarter-wavelength resonator, which converter nearly zero impedance to high impedance. The mismatch of impedance leads to the generation of NBs.

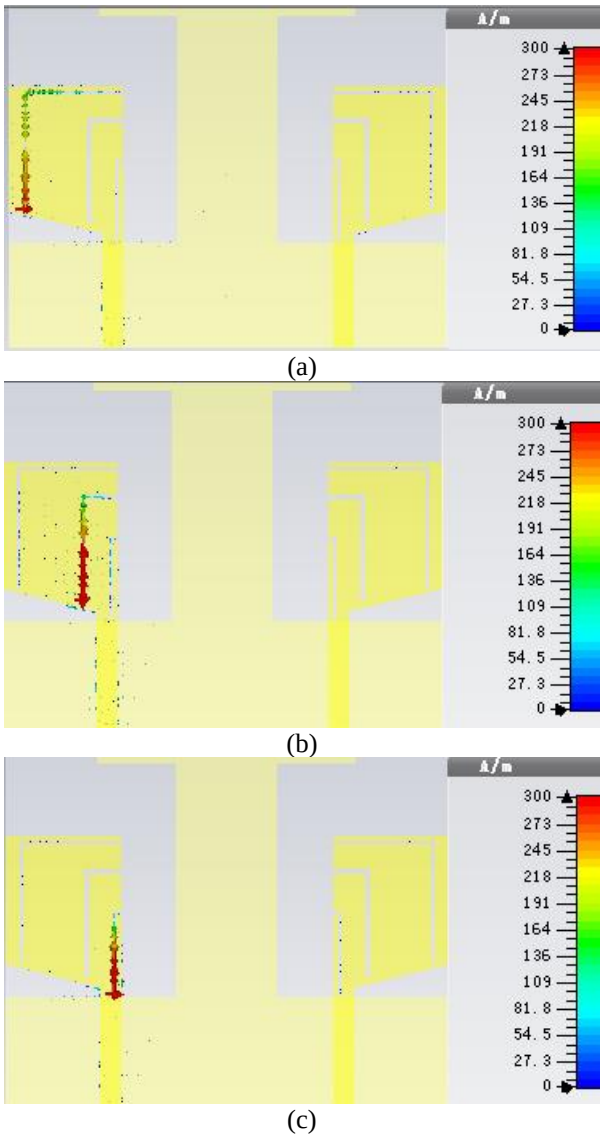

Fig. 6. Surface current distributions when Port 1 is excited: (a) 3.5 GHz, (b) 5.5 GHz, and (c) 8.1 GHz.

III. RESULTS AND DISCUSSIONS

To verify the introduced design method, the antenna was manufactured and tested. The S-parameters of the proposed antenna were measured with Agilent E8362B network analyzer. The results were gained when Port 1 was excited and Port 2 was terminated with a 50 ohm load. As shown in Fig. 7 (a), the introduced antenna maintains S11<-10 dB (or VSWR<2) from 3.1 to 11 GHz, except three notched bands of 3.3-3.75 GHz, 5.07-5.95 GHz and 7.6-8.6 GHz. That means the antenna can filter 3.5 GHz WiMAX, 5.5 GHz WLAN and 8.1 GHz X-band effectively. The same conclusion can be obtained in Fig. 7 (b). From Fig. 7 (c), the value of measured S21 is

smaller than -20 dB in the entire UWB band, which proves that the antenna can be used in MIMO applications. Measured results are in good accordance with simulated analysis except slight deviations, may be caused by manufacturing error and jointing of SMA connector.

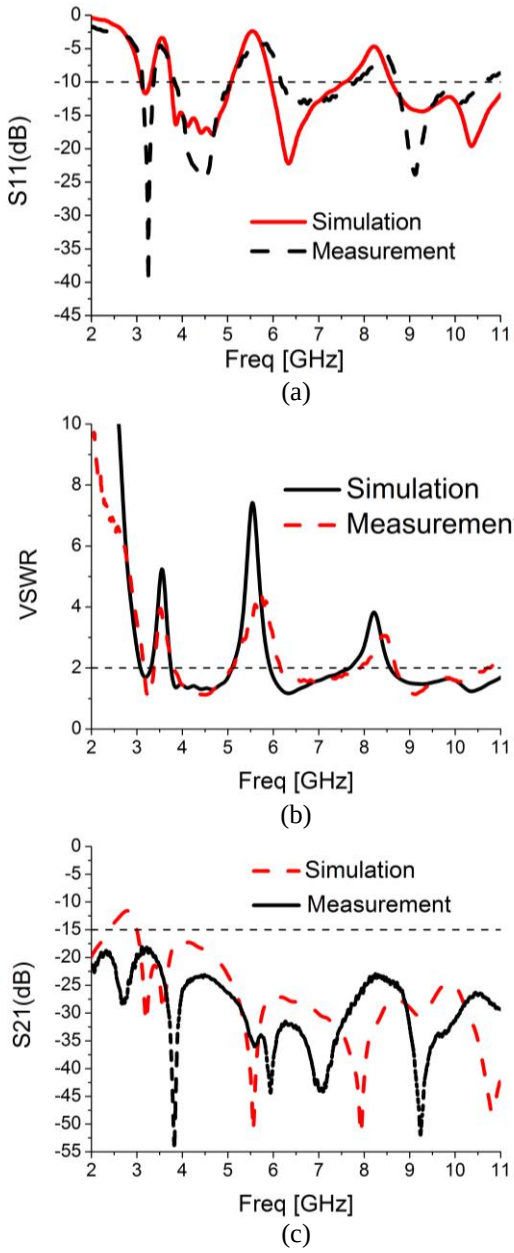

Fig. 7. Simulated and measured S-parameters of the proposed antenna: (a) S11, (b) VSWR, and (c) S21.

Figure 8 shows simulated normalized far field radiation patterns of y-z (E) plane and x-z (H) plane for Port 1 at 4, 6.5, and 9 GHz. It is similar to a dipole in y-z (E) plane, and quasi omnidirectional radiation pattern in the x-z (H) plane. Figure 9 (a) presents the comparison between the peak gain and the other azimuth angles when Port 1 is excited. From Fig. 9 (a), sharp drops are observed at 3.5 GHz, 5.5 GHz, and 8.1 GHz notched frequencies, while in the working band the peak gain is stable with less than 2 dB variation. In addition, when the azimuth angle is 60 degrees or 90 degrees, the gain is always less than the peak gain. Figure 9 (b) shows that radiation efficiency is above 70% except three lowest values at rejected bands.

In order to further evaluate MIMO diversity performance, ECC (envelope correlation coefficient) is analyzed. For two-port MIMO systems, ECC can be calculated by [15]:

$$\rho_e = \frac{\left|S_{11}^{*}S_{12} + S_{21}^{*}S_{22}\right|^2}{\left(1-\left|S_{11}\right|^2-\left|S_{21}\right|^2\right)\left(1-\left|S_{22}\right|^2-\left|S_{12}\right|^2\right)}, \quad (2)$$

for symmetry of Port 1 and Port 2, $S_{11}=S_{22}$, $S_{12}=S_{21}$. After obtaining measured S-parameters, ECC results are calculated by Eq. (2). Figure 10 shows that the ECC are below 0.04 across 3.1-10.6 GHz UWB band.

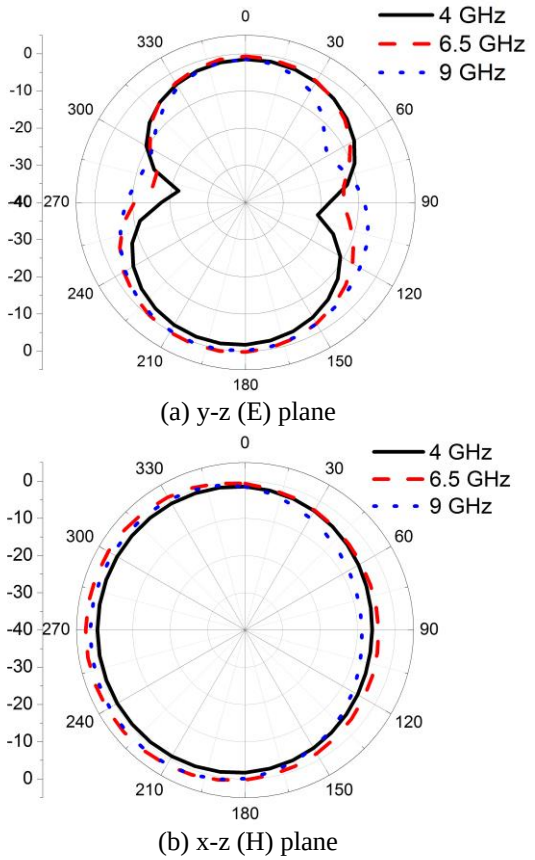

Fig. 8. Simulated normalized far field radiation patterns for Port 1.

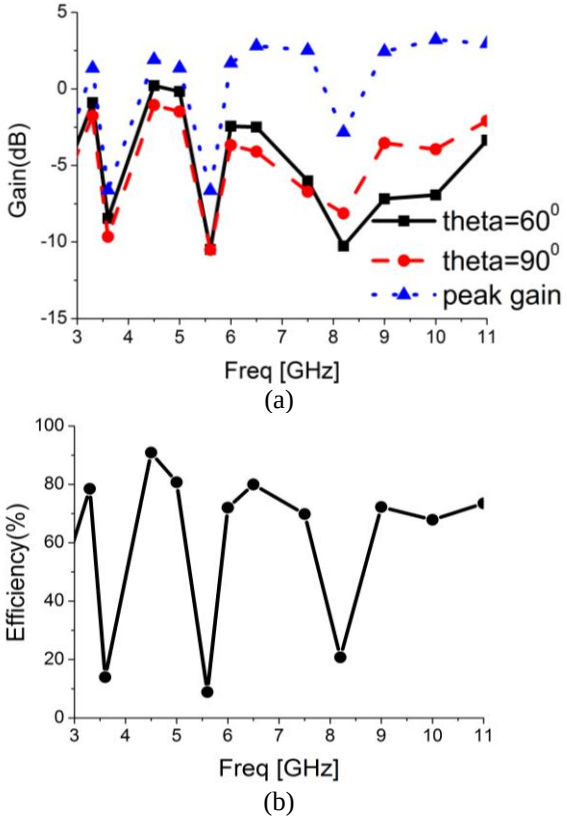

Fig. 9. (a) Simulated gain and (b) simulated radiation efficiency.

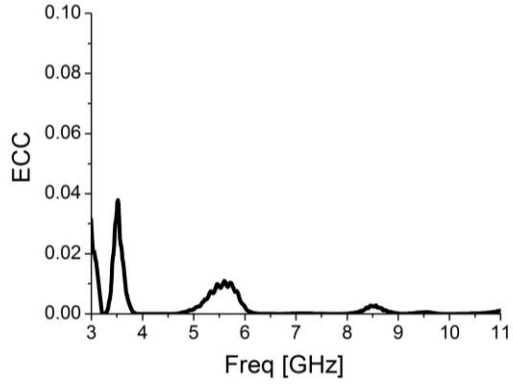

Fig. 10. Measured ECC of the proposed antenna.

Finally, Table 2 compares the introduced antenna with other UWB-MIMO systems. Antennas in [8,9] can cover UWB band, but without filtering performance. [10] introduces a novel decoupling structure (neutralization lines); however, 3.1-5 GHz band was covered. The antennas in [11,12] have 5.5 GHz notch function, but they are relatively large in size. With two notched band characteristic, the antenna in [13] has a bigger size and stronger mutual coupling than the proposed antenna. Also filtering for WiMAX, WLAN and X-band in [14], the proposed antenna has a smaller size. By comparison, this work has a more compact size, high isolation, and triple notched band characteristic.

Table 2: Comparisons of the introduced antenna and other UWB-MIMO antennas

Ref.	Size (mm^2)	Stop Bands (GHz)	Isolation (dB)	BW (GHz)
[8]	35×40	-	-16	3.1-10.6
[9]	30×50.5	-	-20	3.1-10.6
[10]	35×33	-	-22	3.1-5
[11]	48×48	5.5	-15	2.5-12
[12]	38.5×48.5	5.5	-15	3.08-11.8
[13]	30×40	3.5/5.5	-15	3.1-10.6
[14]	30×60	3.5/5.5/8	-20	2.8-11
This work	21×27	3.5/5.5/8.1	-20	3.1-11

*BW is bandwidth.

VI. CONCLUSION

With triple notched band function, a compact UWB-MIMO antenna has been designed and analyzed. Based on half-cutting method, the whole size is only 21×27 mm^2. Three inverted L-shaped slots are inserted on each radiator to notch 3.5 GHz WiMAX, 5.5 GHz WLAN and 8.1 GHz X-band. With a T-shaped stub extruding from the ground plane, the antenna can cover 3.1-11 GHz and high port isolation of -20 dB is achieved. Moreover, good radiation patterns, stable gain, and ECC of less than 0.04 prove it helpful in UWB applications.

ACKNOWLEDGMENT

The authors are grateful to the technical support of the Electromagnetic Laboratory in Huazhong Normal University.

REFERENCES

[1] FCC, “First report and order,” 2002. FCC: First report and order on ultra-wideband technology, Washington, DC, USA, 2002.

[2] T. Kaiser, Z. Feng, and E. Dimitrov, “An overview of ultra-wideband systems with MIMO,” *Proc. IEEE*, pp. 285-312, March 2009.

[3] T. Li, H. Q. Zhai, G. H. Li, L. Li, and C. H. Liang, “Planar ultrawideband antenna with multiple band-notches based on folded stepped-impedance resonator and defected split ring resonator,” *Microw. Opt. Technol. Lett.*, vol. 55, no. 3, pp. 600-603, March 2013.

[4] J. Y. Kim, N. Kim, S. Lee, and B. C. Oh, “Triple band-notched UWB monopole antenna with two resonator structures,” *Microw. Opt. Technol. Lett.*, vol. 55, no. 1, pp. 4-6, January 2013.

[5] J. Liu, K. P. Esselle, S. G. Hay, and S. S. Zhong, “Study of an extremely wideband monopole

antenna with triple band-notched characteristics," *Progress In Electromagnetics Research*, vol. 123, no. 8, pp. 143-158, January 2012.

[6] M. Sun, Y. P. Zhang, and Y. L. Lu, "Miniaturization of planar monopole antenna for ultra-wideband radios," *IEEE Trans. Antennas Propag.*, vol. 58, no. 7, pp. 2420-2425, August 2010.

[7] G. P. Gao, B. Hu, and J. S. Zhang, "Design of a miniaturization printed circular-slot UWB antenna by the half-cutting method,"*IEEE Antennas Wireless Propag. Lett.*, vol. 12, no. 1, pp. 567-570, December 2013.

[8] S. Zhang, Z. N. Ying, J. Xiong, and S. L. He, "Ultrawideband MIMO/diversity antennas with a tree-like structure to enhance wideband isolation," *IEEE Antennas Wireless Propag. Lett.*, vol. 8, no. 4, pp. 1279-1282, February 2009.

[9] M. Bilal, R. Saleem, M. F. Shafique, and H. A. Khan, "MIMO application UWB antenna doublet incorporating a sinusoidal decoupling structure," *Microw. Opt. Technol. Lett.*, vol. 56, no. 7, pp. 1547-1553, July 2014.

[10] S. Zhang and G. F. Pedersen, "Mutual coupling reduction for UWB MIMO antennas with a wideband neutralization line," *IEEE Antennas Wireless Propag. Lett.*, vol. 15, pp. 166-169, January 2016.

[11] P. Gao, S. He, and et al., "Compact printed UWB diversity slot antenna with 5.5-GHz band-notched characteristic," *IEEE Antennas Wireless Propag. Lett.*, vol. 13, no. 4, pp. 376-379, January 2014.

[12] L. Kang, H. Li, X. H. Wang, and X. W. Shi, "Compact offset microstrip-fed MIMO antenna for band-notched UWB applications," *IEEE Antennas Wireless Propag. Lett.*, vol. 14, pp. 1754-1757, January 2015.

[13] T. C.Tang and K. H. Lin, "An ultrawideband MIMO antenna with dual band-notched function," *IEEE Antennas Wireless Propag. Lett.*, vol. 13, pp. 1076-1079, January 2014.

[14] H. Huang, Y. Liu, S. S. Zhang, and S. X. Gong, "Compact polarization diversity ultrawideband MIMO antenna with triple band-notched characteristics," *Microw. Opt. Technol. Lett.*, vol. 57, no. 4, pp. 946-953, April 2015.

[15] S. Blanch, J. Romen, and I. Corbella, "Exact representation of antenna system diversity performance from input parameter description," *Electron. Lett.*, vol. 39, no. 9, pp. 705-707, June 2003.

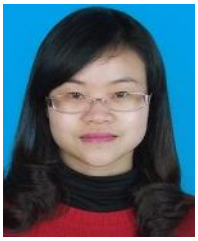

Ling Wu received M.S. degree in Huazhong Normal University in 2007. Currently, she is a Lecturer, and she is pursuing her Ph.D. Her main research includes microtrip-fed antenna design, signal processing.

Yingqing Xia received his Ph.D. in Huazhong Normal University in 2003. From 2006 to 2007, he engaged in postdoctoral research at the University of Oxford. Now he is a Professor who is interested in microwave circuits and hardware systems.

Multi-Functional Ultra-Wideband Monopole Antenna with High Frequency Selectivity

Ying Jiang Guo [1], Kai Da Xu [2,*], and Xiao Hong Tang [1]

[1] EHF Key Lab of Science, University of Electronic Science and Technology of China, Chengdu, 611731, China

[2] Department of Electronic Science, Xiamen University, Xiamen, 361005, China
Shenzhen Research Institute of Xiamen University, Shenzhen 518057, China
*kaidaxu@xmu.edu.cn

Abstract ─ A multi-functional microstrip-fed ultra-wideband (UWB) monopole antenna has been presented. By loading two dual-mode resonators and shunt metallic strips on the reference UWB antenna, two additional operational states are created, including band-notched UWB response (i.e., 3.1~11.5 GHz passband response except the notched band of 5.15~5.8 GHz) and narrow bandpass response (5.5-5.95 GHz) with high frequency selectivity. Moreover, the frequency characteristics of bandpass filtering antenna is also studied when we solder two lumped-chip 0 Ω resistors instead of the shunt metallic strips. Four antenna prototypes are designed, fabricated and measured to validate the design concept. Full-wave electromagnetic simulator HFSS is used for the antenna design optimization and performance prediction. The measured results are presented including return losses, gains and radiation patterns, declaring that the proposed antennas have good impedance matching performance and radiation patterns.

Index Terms ─ High frequency selectivity, monopole antenna, notched band, ultra-wideband.

I. INTRODUCTION

Since the Federal Communications Commission (FCC) released the bandwidth of 3.1-10.6 GHz as the ultra-wideband (UWB) [1] and the concepts of software defined radio (SDR) and cognitive radio (CR) were redefining the design of wireless systems [2], UWB communication systems applied to SDR or CR have attracted great attention in the wireless world due to their advantages including high-speed data rate, flexibility and high capacity. Planar monopole antennas are found as good candidates for UWB applications [3-5] owing to their fascinated features, such as ease of fabrication, simple structure, and good radiation properties. However, in practical applications, in order to eliminate the frequency interference between UWB system and other wireless communication systems, it is significantly necessary to design UWB antennas with notched bands. Meanwhile, for most of the existing SDR and CR antennas, more than one antenna radiator is needed to achieve multi-function performance, and additional isolation techniques are also needed for mutual coupling reduction [6]. It significantly increases design complexity. Thus, the antenna with a single radiator but multiple operational states is highly required. Some multi-functional UWB antennas based on the same radiator were reported [7-8]. A novel multi-state RF MEMS switch was developed in 2013 [7] to achieve multiple operational states. Recently, the split ring resonators and short strips were used to realize transformation between band-notched UWB and narrow band response [8]. However, the bandwidths and the frequency selectivity of these designs are limited due to the inherent narrowband nature of these structures. Although great efforts have been made to achieve higher selectivity [9-13], these designs were realized by altering the structure of the radiation element, which may be not easily applied to other UWB antennas with different radiation elements. Moreover, some of them [10], [11] utilized two resonators with two different resonant frequencies to create a wide notched band, which would lead to an increase of the design complexity. In our previous work [14], a UWB antenna with dual notched bands with high frequency selectivity are presented.

In this paper, a novel multi-functional planar monopole antenna with high frequency selectivity is proposed. By placing two dual-mode resonators beside the feed line of UWB antenna, a band-notched UWB response with two reflection zeros at either side of the notched band is generated. Based on the same structure, the narrow bandpass filtering characteristic will be created when two metallic shunt strips are added. Moreover, two lumped-chip 0 Ω resistors instead of the shunt strips are utilized in the bandpass filtering antenna to obtain a simple, flexible and reconfigurable design.

Submitted On: August 26, 2016
Accepted On: January 1, 2018

II. ANTENNA DESIGN AND ANALYSIS

Three antenna prototypes named Antennas A, B and C with varied loadings of dual-mode resonators and metallic shunt strips have been proposed as shown in Fig. 1. Antenna A is a basic UWB antenna regarded as the reference antenna. Antenna B is developed with a pair of dual-mode resonators along the feed line based on the reference antenna, as seen in Fig. 1 (b). Moreover, two shunt strips are added for Antenna C as depicted in Fig. 1 (c). The added strips are located to align with the symmetric axis of the loading resonators. On the bottom layer, there is a metallic ground plane with a size of $L_5 \times W$ as seen in Fig. 2, where a square shaped slot with a size of $L_6 \times W_3$ is etched. This slot is employed to improve the return losses of the UWB antenna.

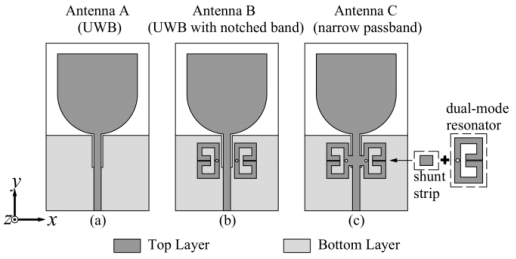

Fig. 1. Schematic view of: (a) Antenna A, (b) Antenna B, and (c) Antenna C.

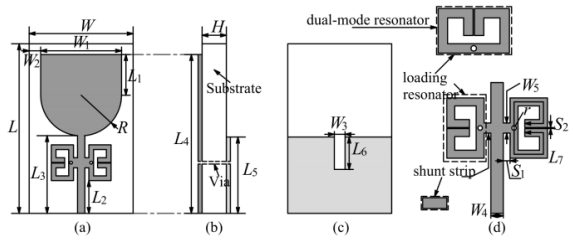

Fig. 2. Geometry of Antenna C: (a) top view, (b) side view, (c) bottom view, and (d) schematic of feed line loaded with dual-mode resonators and shunt strips.

The proposed resonator with a metallic via loaded in the center can be seen as a second-order quarter-wavelength resonator [15] or a short-circuited stub-loaded half-wavelength resonator with the zero stub length [16], which is a dual-mode resonator. The center frequency f_r of the notched band or the passband in the antenna design can be approximately calculated by:

$$f_r = \frac{c}{\lambda_g \sqrt{\varepsilon_{eff}}} \approx \frac{c}{2L_7 \sqrt{(\varepsilon_r + 1)/2}}, \quad (1)$$

where λ_g denotes the guided wavelength, c is the light velocity in free space, L_7 is the whole length of the resonator, ε_{eff} and ε_r denote the effective dielectric constant and relative dielectric constant of the substrate, respectively.

To investigate the frequency characteristics of the proposed antenna structures loaded with the dual-mode resonators, Fig. 3 demonstrates the frequency responses of the Antennas B and C with respect to different L_7 and S_2 while other dimensions of the loading resonators are fixed as follows: W=30, W_1=20, W_2=5, W_3=1, W_4=1.1, W_5=1.5, L=37, L_1=10, L_2=4.85, L_3= L_5=11.5, L_4=37, L_6=5, S_1=0.1, and the radius of the via r =0.2, all in mm. They are all modeled on the substrate with a relative dielectric constant ε_r =3.66 and a thickness H=0.508 mm. The physical dimensions of radiators and feed lines are all identical. The notched band of the Antenna B and the passband of the Antenna C are designed to operate at the frequency of f_r to tune the parameter L_7 according to the Equation (1). For instance, when L_7=16.5 mm, the theoretical center frequency of two bands is around 5.95 GHz, which almost agree with the simulated results in Figs. 3 (a) and (c). On the other hand, the bandwidth of the notched band is mainly determined by the two resonant frequencies of the resonator, which can be adjusted by the intra-coupling of the dual-mode resonator, i.e., the parameter S_2.

For Antenna B, the center frequency of the notched band can be tuned by controlling the parameter L_7 while other parameters are fixed (see Fig. 3 (a)). Besides, the parameter S_2 affects the bandwidth of the notched band as demonstrated in Fig. 3 (b). Meanwhile, the frequency characteristics of the narrow bandpass filtering antenna (Antenna C) is plotted in Figs. 3 (c) and (d), where the center frequency and bandwidth of the passband can also be controlled by L_7 and S_2, respectively. Thus, the frequency characteristics of the notched band and passband responses can be flexibly adjusted by the loading resonators without tuning the antenna radiator parameters. In addition, it is worthwhile to highlight that two reflection zeros are located at the edges of the notched band, thus high frequency selectivity can be achieved. Compared with the proposed single-mode resonator in [8], this design can obtain wider bandwidth due to the dual-mode feature.

Furthermore, to switch from band-notched UWB state to narrow bandpass state (or vice versa) conveniently, two lumped-chip 0 Ω resistors with each size of 1 mm × 0.5 mm are soldered to replace the shunt strips in Antenna C, paving the way to realize antenna reconfigurable design. Figure 4 shows the schematic view of this antenna, namely, Antenna D, whose dimensions are the same as those of Antenna C. Figure 5 displays the frequency responses of Antenna D when the parameters L_7 and S_2 are varied while other parameters are fixed. It manifests that Antenna D exhibits similar bandpass filtering response compared to Antenna C, where center frequency and bandwidth of the passband can also be easily controlled by altering the loading resonator dimensions. Two resonant modes can be also seen within the passband. Therefore, the variations of the notched band and passband with the changes of the

loading resonator parameters, and the switch from Antenna B to Antenna C can be both exploited in future by introducing varactors, PIN diodes or memristors [17] for practically reconfigurable achievement.

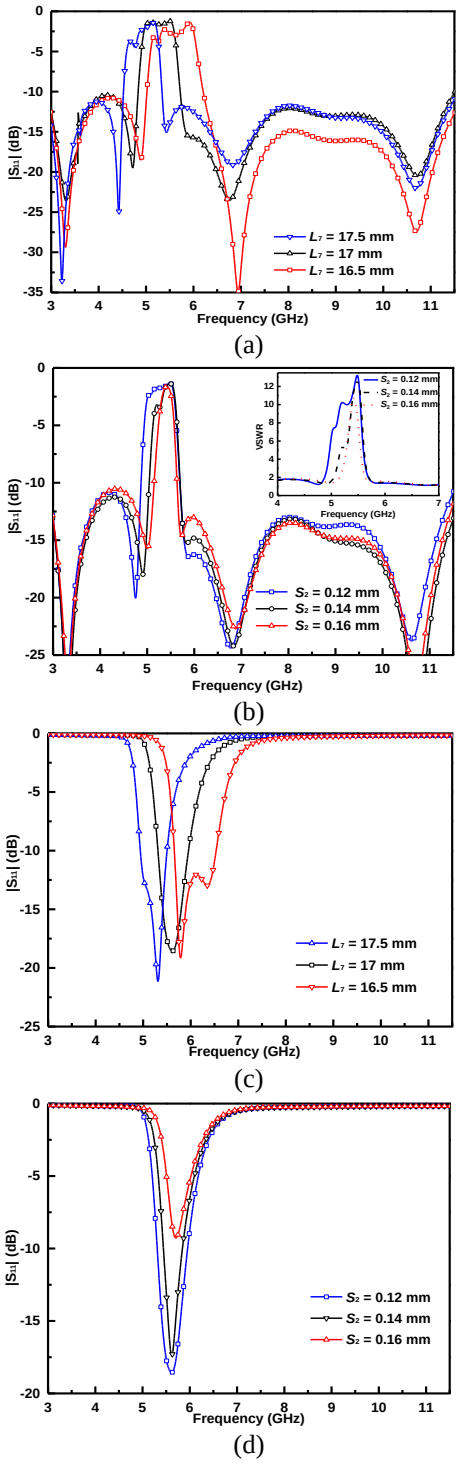

Fig. 3. Simulated reflection coefficients of Antenna B with varied (a) L_7 and (b) S_2, as well as Antenna C with varied (c) L_7 and (d) S_2.

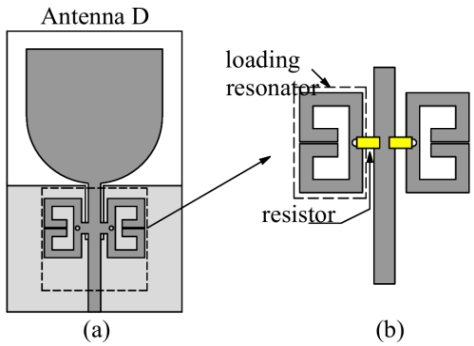

Fig. 4. Schematic view of: (a) Antenna D and (b) corresponding details of the loading resonators.

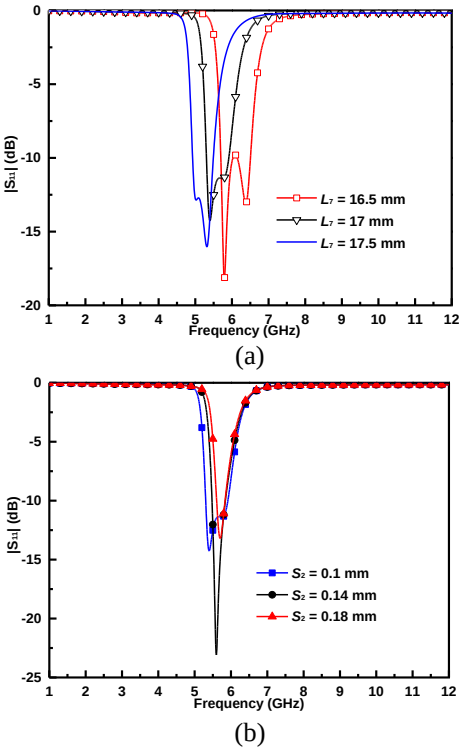

Fig. 5. Simulated reflection coefficients of Antenna D with respect to varied dimensions of the loading resonators.

III. MEASUREMENTS AND DISCUSSION

In order to validate the proposed idea, Antennas A, B, C and D with desired resonant frequencies are designed, simulated, and implemented based on the analysis above. The dimensions of the four antennas are determined as follows (all in mm): W=30, W_1=20, W_2=5, W_3=1, W_4=1.1, W_5=1.5, L=37, L_1=10, L_2=4.85, L_3=11.5, L_4=37, L_5=11.5, L_6=5, L_7=17, S_1=S_2=0.1. The simulated and measured reflection coefficients of the four antennas are illustrated in Fig. 6, using the full-wave electromagnetic simulator HFSS and Agilent E8363B

vector network analyzer, respectively.

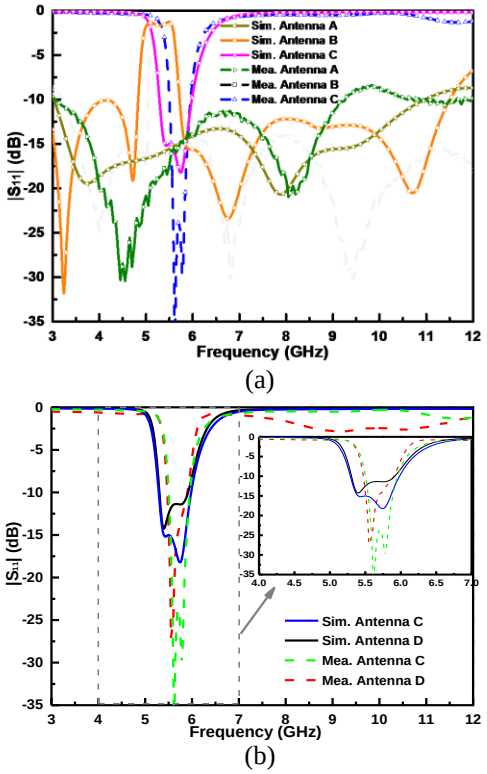

Fig. 6. (a) Simulated and measured reflection coefficients of Antennas A, B and C, and (b) reflection coefficient comparisons between Antennas C and D.

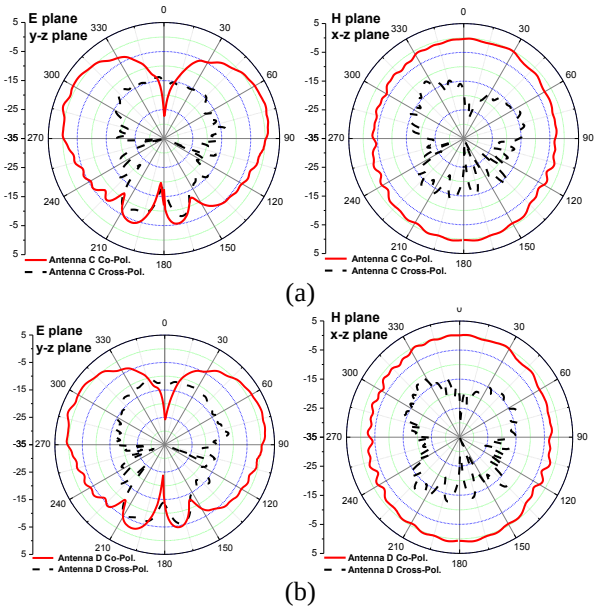

Fig. 7. Measured co-polarized and cross-polarized radiation patterns of: (a) Antenna C in E- and H-planes, and (b) Antenna D in E- and H-planes at 5.6 GHz.

For Antenna B, the return loss is below -10 dB from 3.1 to 11.5 GHz except the notched band with the 10-dB return loss bandwidth of 5.15-5.8 GHz which can be used to reject the 5.2/5.8-GHz (5.15-5.35/5.725-5.825 GHz) WLAN bands. Two reflection zeros are observed at both sides of the notched band, which ensures high frequency selectivity. For Antenna C, a narrow passband filtering antenna of 5.5-5.95 GHz (S_{11} < -10 dB) with two resonant modes is achieved. Since the value of resistance in a lumped *RLC* boundary in HFSS must be at least 10 μΩ, the resistor of 10 μΩ in the simulation is taken place of the practical soldering 0 Ω resistor in Antenna D. The reflection coefficients of Antenna D and Antenna C are in agreement, which mean that 0 Ω resistor has nearly the same effect as the metallic strip. The slight discrepancy between these two antennas may be attributed to the non-ideal resistance behavior, width differences of the strip or errors caused by soldering. In addition, the center frequencies of the notched band and the narrow passband are both close to the resonant frequencies of the loading resonators.

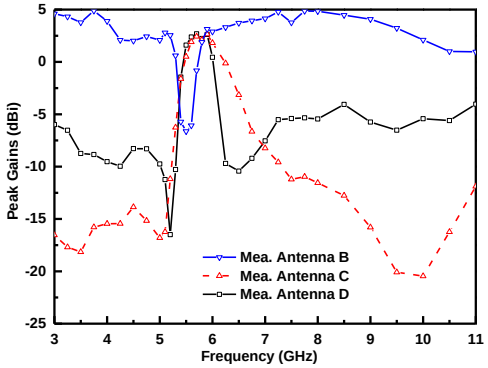

Fig. 8. Measured peak gains of Antennas B, C and D.

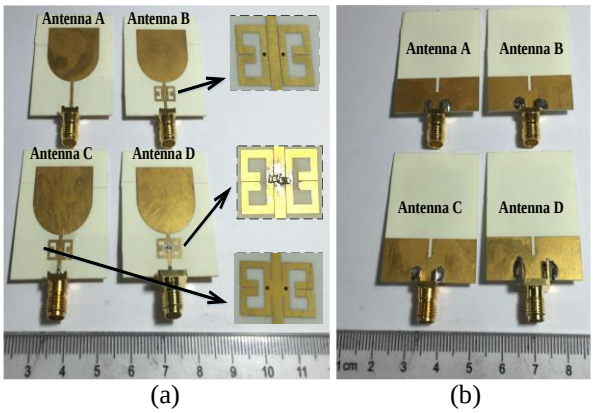

Fig. 9. Photographs of the four fabricated antennas: (a) top view and (b) bottom view.

Figure 7 shows the measured co-polarized and

cross-polarized radiation patterns of the Antennas C and D in E- and H-plane at 5.6 GHz. We can see that both of the antennas have good dipole-like co-polarized radiation patterns in E-plane and omnidirectional patterns in H-plane. Moreover, the measured peak gains of Antennas B, C and D are plotted in Fig. 8. The peak gain of Antenna B significantly decreases at the notched bands due to the function of the loading resonator, while both of Antennas C and D have opposite effects compared to Antenna B. The photograph of the four fabricated prototypes is displayed in Fig. 9. Table 1 exhibits the comparisons between the proposed design and the previous reported work, which shows that our work has the advantages of high frequency selectivity, multiple operation states and miniaturized size.

Table 1: Performance comparisons with some previous antennas

	Frequency Selectivity	Technique of the Notched Band	No. of Operation States	Antenna Size $\lambda_g \times \lambda_g$*
[8]	Poor	A pair of SRRs	3	1.54×1.54
[9]	Good	Nonuniform stub + coupled-line + two substrate layers	1	1×0.92
[11]	Good	Two slots + two stubs	2	0.94×0.8
[13]	Moderate	Folded strips	1	1.14*1.26
This work	**Good**	**Dual-mode resonators**	**3**	**1×0.8**

*λ_g is the guided wavelength of 50 Ohm microstrip line on the substrate at the center frequency of their corresponding notched bands.

IV. CONCLUSION

A planar multi-functional microstrip-fed UWB antenna with high frequency selectivity has been studied and investigated. By loading a pair of dual-mode resonators and the metallic shunt strips, the antenna exhibits band-notched UWB response and narrow bandpass response. High frequency selectivity is obtained by the intrinsic feature of the loading resonators. To verify the proposed idea, four practical antennas have been fabricated and measured. Due to its simple structure, flexible design and excellent performance, the proposed antennas are expected to be good candidates for use in UWB systems.

ACKNOWLEDGMENT

This work was supported in part by the National Natural Science Foundation of China (No. 61601390), and Shenzhen Science and Technology Innovation Project (No. JCYJ20170306141249935).

REFERENCES

[1] Federal Communications Commission, "First report and order in the matter of revision of part 15 of the Commission's Rules Regarding Ultra-Wideband Transmission Systems," ET-Docket 98-153, Apr. 22, 2002.

[2] P. S. Hall, P. Gardner, and A. Faraone, "Antenna requirements for software defined and cognitive radios," *Proc. IEEE*, vol. 100, no. 7, pp. 2262-2270, 2012.

[3] J. Liang, C. Chiau, X. Chen, and C. Parini, "Study of a printed circular disc monopole antenna for UWB system," *IEEE Transactions on Antennas & Propagation*, vol. 53, no. 11, pp. 3500-3504, 2005.

[4] N. P. Agrawall, G. Kumar, and K. P. Ray, "Wide-band planar monopole antennas," *IEEE Transactions on Antennas & Propagation*, vol. 46, no. 2, pp. 294-295, 1998.

[5] C. W. Ling, W. H. Lo, R. H. Yan, and S. J. Chung, "Planar binomial curved monopole antennas for ultrawideband communication," *IEEE Transactions on Antennas & Propagation*, vol. 55, no. 9, pp. 2622-2624, 2007.

[6] F. Ghanem, P. S. Hall, and J. R. Kelly, "Two port frequency reconfigurable antenna for cognitive radios," *Electronics Letters*, vol. 45, no. 11, pp. 534-536, 2009.

[7] A. Pourziad, S. Nikmehr, and H. Veladi, "A novel multi-state integrated RF MEMS switch for reconfigurable antennas applications," *Progress in Electromagnetics Research*, vol. 139, no. 3, pp. 389-406, 2013.

[8] J. Y. Siddiqui, C. Saha, and Y. M. M. Antar, "A novel ultrawideband (UWB) printed antenna with a dual complementary characteristic," *IEEE Antennas & Wireless Propagation Letters*, vol. 14, pp. 974-977, 2015.

[9] C. T. Chuang, T. J. Lin, and S. J. Chung, "A band-notched UWB monopole antenna with high notch-band-edge selectivity," *IEEE Transactions on Antennas & Propagation*, vol. 60, no. 10, pp. 4492-4499, 2012.

[10] Q. X. Chu, C. X. Mao, and H. Zhu, "A compact notched band UWB slot antenna with sharp selectivity and controllable bandwidth," *IEEE Transactions on Antennas & Propagation*, vol. 61, no. 8, pp. 3961-3966, 2013.

[11] Z. H. Tu, W. A. Li, and Q. X. Chu, "Single-layer differential CPW-fed notch-band tapered-slot UWB antenna," *IEEE Antennas & Wireless Propagation Letters*, vol. 13, pp. 1296-1299, 2014.

[12] T. G. Ma, R. C. Hua, and C. F. Chou, "Design of a multiresonator loaded band-rejected ultrawideband planar monopole antenna with controllable notched bandwidth," *IEEE Transactions on Antennas & Propagation*, vol. 56, no. 9, pp. 2875-2883, 2008.

[13] T. G. Ma and J. W. Tsai, "Band-rejected ultrawideband planar monopole antenna with high frequency selectivity and controllable bandwidth using inductively coupled resonator pairs," *IEEE Transactions on Antennas & Propagation*, vol. 58, no. 8, pp. 2747-2752, 2010.

[14] Y. J. Guo, X. Tang, K. D. Xu, and J. Ai, "Dual high-selectivity band-notched UWB monopole antenna using simple dual-mode resonator and high-impedance lines," *International Journal of Microwave and Wireless Technologies*, vol. 9 no. 4, pp. 923-929, 2017.

[15] F. Cheng, X. Q. Lin, Z. B. Zhu, L. Y. Wang, and Y. Fan, "High isolation diplexer using quarter-wavelength resonator filter," *Electronics Letters*, vol. 48, no. 6, pp. 330-331, 2012.

[16] K.-D. Xu, Y.-H. Zhang, C.-L. Zhuge, and Y. Fan, "Miniaturized dual-band bandpass filter using short stub-loaded dual-mode resonators," *Journal of Electromagnetic Waves and Applications*, vol. 25, pp. 2264-2273, 2011.

[17] K. D. Xu, Y. H. Zhang, L. Wang, M. Q. Yuan, Y. Fan, W. T. Joines, and Q. H. Liu, "Two memristor SPICE models and their applications in microwave devices," *IEEE Transactions on Nanotechnology*, vol. 13, no. 3, pp. 607-616, 2014.

Ying Jiang Guo received the B.E. degree in Electronic Engineering from the Sichuan University, Chengdu, China in 2008, and received M.S. in Electromagnetic Field and Microwave Technology from the University of Electronic Science and Technology of China (UESTC), Chengdu, China in 2011, where he is currently working toward the Ph.D. degree in Electromagnetic Field and Microwave Technology. From 2011 to 2013, he was with the Chengdu Research Institute of Huawei Technology Ltd., where he was involved in the pre-research of ultra-wideband power amplifier, high frequency clock for AD and 5G communication prototype design. From 2013 to 2014, he was with the Sichuan Normal University, where he was a Lecturer. He has filed/granted a number of China patents in microwave circuit and internet of vehicle. His research interests include RF/microwave/mm-wave circuits design, antennas design, and monolithic-microwave integrated circuit applications.

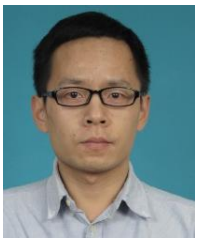

Kai Da Xu received the B.S. and Ph.D. degrees in Electromagnetic Field and Microwave Technology from University of Electronic Science and Technology of China (UESTC), Chengdu, China, in 2009 and 2015, respectively.

From 2012 to 2014, he was a Visiting Researcher in the Department of Electrical and Computer Engineering, Duke University, Durham, NC, under the financial support from the China Scholarship Council (CSC). From 2016 to 2017, he was a Postdoctoral Fellow with the State Key Laboratory of Millimeter Waves, City University of Hong Kong, Hong Kong. He is currently an Assistant Professor with the Department of Electronic Science, Xiamen University, Xiamen, China. He received the UESTC Outstanding Graduate Awards in 2009 and 2015. He was the recipient of National Graduate Student Scholarship in 2012, 2013, and 2014 from Ministry of Education, China. He has authored and coauthored over 70 papers in peer-reviewed journals and conference proceedings. Since 2014, he has served as a Reviewer for some journals including the IEEE TMTT, IEEE TED, IEEE TCAD, IEEE AWPL, IEEE MWCL, and ACES Journal. He is currently an Associate Editor of the IEEE Access, and Electronics Letters. He is also an Editorial Board Member of the AEÜ-International Journal of Electronics and Communications. His research interests include RF/microwave and mm-wave circuits, antennas, and nanoscale memristors.

Xiao Hong Tang was born in Chongqing, China, in 1962. He received the M.S. and Ph.D. degrees in Electromagnetism and Microwave Technology from the University of Electronic Science and Technology of China (UESTC), Chengdu, China, in 1983 and 1990, respectively. In 1990, he joined the School of Electronic Engineering, UESTC, as an Associate Professor, and became a Professor in 1998. He has authored or coauthored over 80 technical papers. His current research interests are microwave and millimeter-wave circuits and systems, microwave integrated circuits, and computational electromagnetism.

Novel Compact Microstrip Dual-Mode Filters with Two Controllable Transmission Zeros

Zhaojun Zhu, Lu Cao, and Chaolei Wei

Institute of Applied Physics
University of Electronic Science and Technology of China, Chengdu, 610054, China
uestc98@163.com, cl_stella@163.com, uestcweichaolei@163.com

Abstract ─ Novel compact pentagonal dual-mode filters by short-loaded are presented. The field patterns of this type of resonators are investigated using full-wave electromagnetic simulations. The technique of utilizing capacitive and inductive source-load coupling to improve the performance of filters is fully researched. Advantages of using this type of filter are not only its compact size, but also its transmission zeros that can be independently controlled. Then, two dual-mode bandpass filters are designed, fabricated and tested to validate the design. Good agreement is achieved between the measured results and simulated ones.

Index Terms ─ Bandpass filter, dual-mode, source-load coupling, transmission zero.

I. INTRODUCTION

Bandpass filter is one of the most important components in microwave circuits. To meet the requirement of modern microwave communication systems, microwave bandpass filters with compact size and high performance are in urgent demand. The dual-mode resonators are attractive because each resonator can be used as a doubly tuned circuit, and the number of resonators is reduced by half, resulting in a compact size. Wolff first demonstrated a microstrip dual-mode filter in 1972 [1]. Since then, dual-mode microstrip filters have been widely used in communications systems [2-3]. Among them, E-shaped microstrip resonators and filters have been originally reported [4]. More recently, the E-shaped resonator was modeled as a dual-mode resonator [5]. However, it was difficult to control the location of the transmission zeros. Circular dual-mode filter based on source-load coupling was proposed [6]. By introducing a capacitive cross-coupling between the input and output ports, the additional zero can be generated, but that can't be independently controlled. The open stub dual-mode filter with adjustable transmission zeros by inductive source-load coupling was firstly proposed [7-8]. Two novel bandpass filters with multiple transmission zeros using four open/ shorted stubs were proposed [9-10]. The out-of-band transmission zeros can be adjusted easily by only changing the electrical length of the four open/shorted stub. But the resonator occupied a large circuit area, size reduction is becoming a major design consideration for modern practical applications. Two filters [11], with pentagonal dual-mode resonator and capacitive/ inductive S-L coupling, have been designed and fabricated in the last two years. Which show good stopband rejection with adjustable transmission zeros.

In this paper, two compact bandpass filters with a pentagonal dual-mode resonator and source-load coupling are introduced. The reduction of the size is achieved by using a pentagonal dual-mode resonator. Furthermore, with a cross-coupling between the input and output feed lines, two tunable transmission zeros are obtained. The transmission zeros can be controlled independently by changing the amount of the capacitive or inductive source-load coupling. The proposed bandpass filter shows a good stopband rejection because of the two tunable transmission zeros. Two practical filters verify the feasibility of the technique.

II. DUAL-MODE PENTAGONAL RESONATOR

Figure 1 shows the geometry of proposed dual-mode filters with the pentagonal open-loop resonator with short-loaded. The filter comprises an improved pentagonal half-wavelength resonator and a short-loaded stub. A via hole was used to achieve the required short. The source-load coupling include two types, i.e., capacitive and inductive.

The proposed dual-mode filter can be equivalent to a T-shaped resonator model with a half-wavelength resonator and an inductance-loaded element as shown in Fig. 2. Z_1 is the characteristic impedance of the half-wavelength resonator with the electrical length $\theta_1 = 90$. L_1 is the equivalent inductance of the short-loaded stub. C_1 is the coupling capacitance between resonator and feed line. A via hole was used to achieve the required inductance. The usage of short-loaded stub saves the circuit size compared with that of open-loaded stub.

Submitted On: August 8, 2017
Accepted On: October 12, 2017

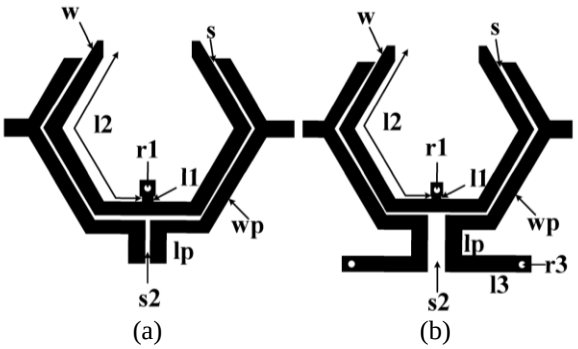

(a) (b)

Fig. 1. Layout of the proposed pentagonal dual-mode bandpass filter. (a) Capacitive source-load coupling, and (b) inductive source-load coupling.

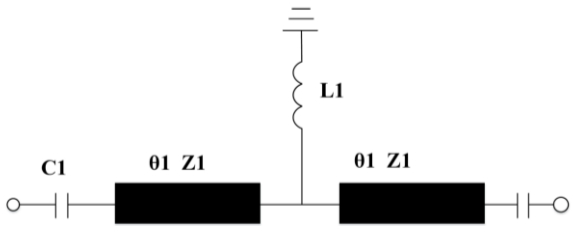

Fig. 2. Schematic of a half-wavelength resonator with an inductance-loaded.

For a compact size, the half-wavelength lines are bent to a pentagon. The via hole at the centre of the resonator introduces another transmission pole near the fundamental frequency of the half-wavelength resonator. This new pole and the fundamental frequency pole make the proposed structure a dual-mode resonator. So this symmetric structure can support two modes, i.e., an even mode and an odd mode.

The commercially available full-wave electro-magnetic simulators (HFSS) were used to characterize the electric field patterns for the dual-mode resonator. HFSS uses the finite element method (FEM) to analyze the electromagnetic characteristics of 3D objects. The basic process of solving the problem by FEM includes three parts, which are the mesh discretization of the object, the solution of the simultaneous matrix equations related the mesh and the postprocessing calculation of the problem.

It can be seen that the whole structure is symmetrical with the center point, so the center point is modeled as the origin point and the mirror operation is applied. The physical excitation of the filter is by the coaxial line with the TEM wave. In order to use the wave-guide port in the simulation code, the port surface must cover more than ninety-five percent of the TEM field. It is assumed that the width of the excitation microstrip is w and the thickness of the dielectric layer is h. The height of the wave port is generally set to 6~10h. When w>h, the width of the wave port is set to about 10w; when w<h, the width of the wave port is set to about 5w. Finally, the height and width of the wave port are 10h and 10w in this paper.

According to the standard which is set up by user, HFSS simulation code uses adaptive mesh generation technology. The solution frequency of the meshing is generally set at the center frequency of the filter. After each new mesh subdivision, HFSS will compare the results of the S parameters with the old one. If the error is less than the set criterion, it is shown that the result is convergent and the adaptive process will end. The dimensions are optimized by a full-wave simulation to take all the discontinuities into consideration.

Figure 3 depicts the simulated electric field vector between the metal strip and ground plane at the resonance frequency. The electric field pattern of the odd mode is illustrated in Fig. 3 (a), where the maxima of the field are located along the left and right arms and no fields on the loaded-element. The field distribution is similar to that of a half-wavelength single-mode resonator. As a consequence, the short-loaded element does not affect the resonant frequency of the odd mode. Figure 3 (b) shows the electric field pattern of the even-mode, where the maxima of the field are also located along the two arms, but part of the fields moved to the loaded-element. Moreover, it is observed from the direction of the electric field vector that the field is symmetric with respect to the symmetry axis. Hence, changing the dimension of the short-loaded element makes the resonant frequency of the even mode shift. The two resonant poles can be adjusted independently.

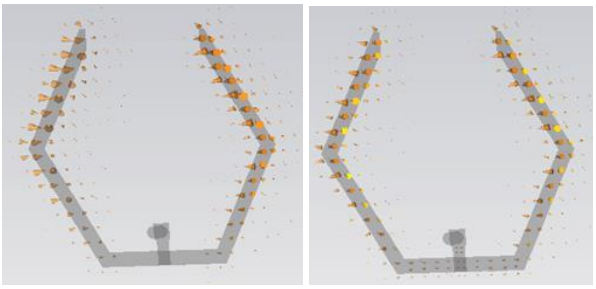

(a) (b)

Fig. 3. Electric field patterns for the pentagonal dual-mode resonator: (a) odd mode and (b) even mode.

To observe the mode splitting, the pentagonal dual-mode resonators have been simulated using a full-wave EM eigen-mode solver with different loaded element size. The simulated resonant frequencies of the two modes are plotted in Fig. 4 as a function of the size l_1 and l_2.

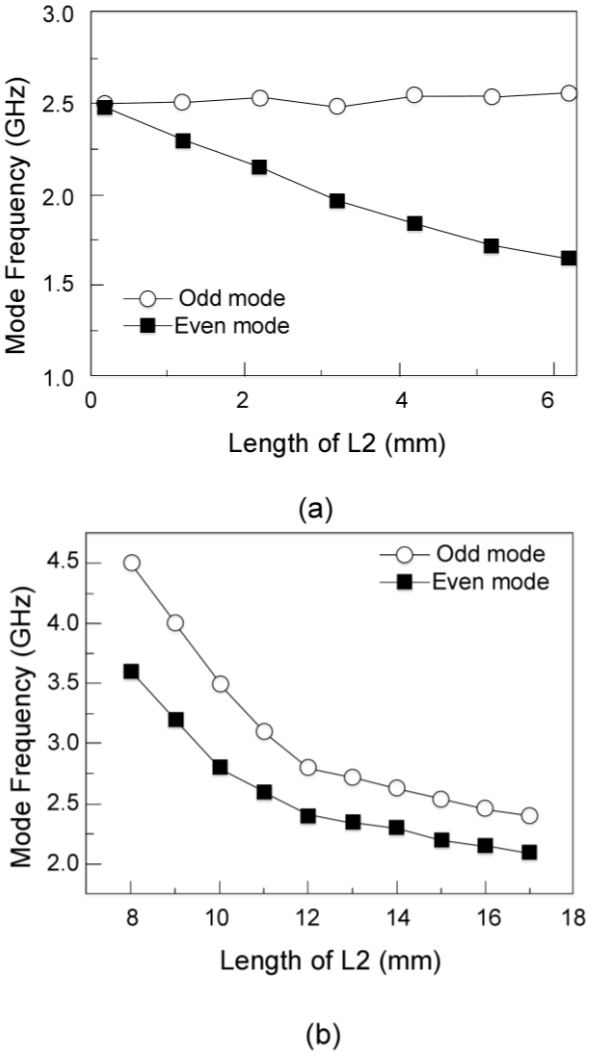

Fig. 4. Resonance frequencies of the two modes against: (a) l_1, where l_2 = 15 mm, (b) l_2, where l_1 = 0.8 mm for short-loaded resonator.

When l_1 increases from 0.2 to 6.2 mm, the resonant frequency of the even mode decreases from 2.48 to 1.7 GHz, while that of the odd mode hardly change. l_2 will affect both the even and odd mode.

III. BANDPASS FILTERS USING PENTAGONAL DUAL-MODE RESONATOR

Figure 1 shows the layout of the proposed pentagonal dual-mode bandpass filter. It consists of the capacitive source-load coupling filter and inductive one. The gap between the resonator and feed line was selected in consideration of strong coupling and etching tolerance. The length of the source-load coupling line is l_P. The characteristic impedance of the input/output feed line is taken as 50 ohm.

By investigation, the dual-model filter has an interesting property. There is an inherent finite-frequency transmission zero when the two modes split. If the frequency of even mode is less than that of odd mode, the inherent transmission zero would be in the lower stopband. If the frequency of even mode is greater than that of odd mode, the inherent transmission zero would be in the upper stopband. As shown in Fig. 4, the frequency of the even mode is always less than that of the odd mode for the short-loaded resonator, so the inherent transmission zero would be in the lower stopband.

For further improving the filters' performance, the source-load coupling is introduced to generate an additional transmission zero. By our research, the locations of the additional transmission zeros can be controlled by transforming the amount and type of the source-load cross-coupling. For the inductive coupling, the additional transmission zero will be in the lower stopband. While, for the capacitive coupling, the additional transmission zero will be in the upper stopband. So, the response with two adjustable transmission zeros can be obtained for the proposed filters. Two sample filters verify the feasibility of the new technique.

A. Dual-mode filter with capacitive S-L coupling

Filter A demonstrates a filtering characteristic with the finite transmission zeros in the both lower and upper stopband. As it has been noted, for the short-loaded dual-mode filter, the inherent transmission zero would be in the lower stopband. So, the capacitive source-load coupling is introduced to generate the additional zero in the upper stopband. The transmission zeros can be controlled by changing the amount of the source-load coupling. As shown in Fig. 5, when s2 decreases from 0.8 to 0.2 mm, the transmission zeros move toward the passband edge with better stopband rejection. Also, the selectivity can be improved when l_P increases as shown in Fig. 6. Therefore, the amount of cross-coupling can be selected to meet the required filter selectivity.

Figure 7 shows the photograph of the fabricated filter A. The simulated and measured results are shown in Fig. 8. As shown in Fig. 8, the filter A operated at 2.75 GHz and a 3 dB fractional bandwidth of 9.5%. The minimum insertion loss is about 1.4 dB, and the return loss is greater than 15 dB in the passband. Two transmission zeros are located at 2.27 GHz and 3.44 GHz respectively, which provide a better cutoff rate in the stopband.

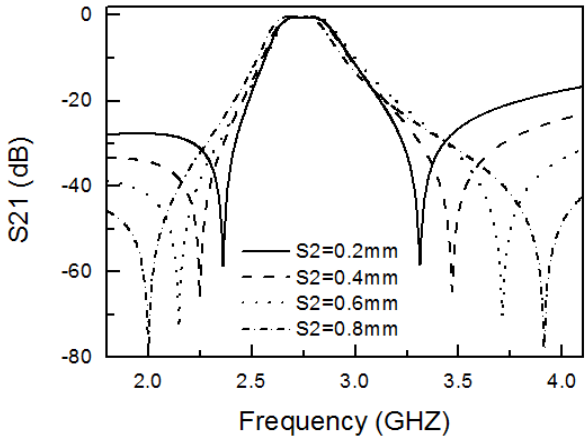

Fig. 5. Simulated scattering parameters of the filter A against s_2.

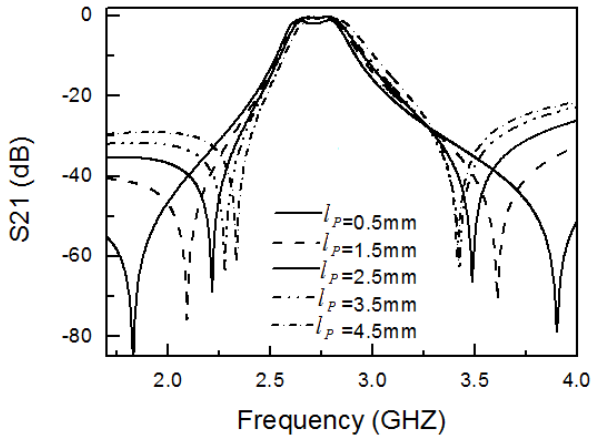

Fig. 6. Simulated scattering parameters of the filter A against l_p.

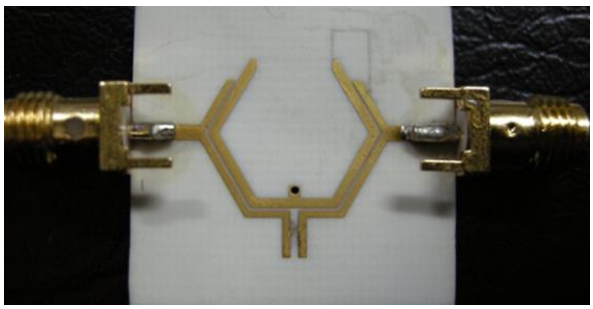

Fig. 7. Photograph of the fabricated filter A.

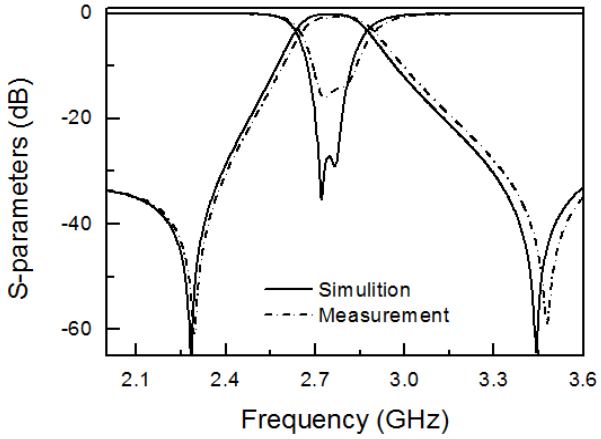

Fig. 8. Simulated and measured results of the filter A.

B. Dual-mode filter with inductive S-L coupling

Filter B demonstrates a filtering characteristic with the both finite transmission zeros in the lower stopband. The inherent transmission zero is in the lower stopband for short-loaded filter. Also, the inductive source-load coupling is introduced to generate the additional zero in the lower stopband. Figure 9 and Fig. 10 show the simulated s_{21} as a function of the s_2 and l_P. The inner transmission zero is the inherent zero, and the outer one is the additional transmission zero. The inherent transmission zero hardly changes, but the additional one can be distinctly controlled by the amount of source-load coupling.

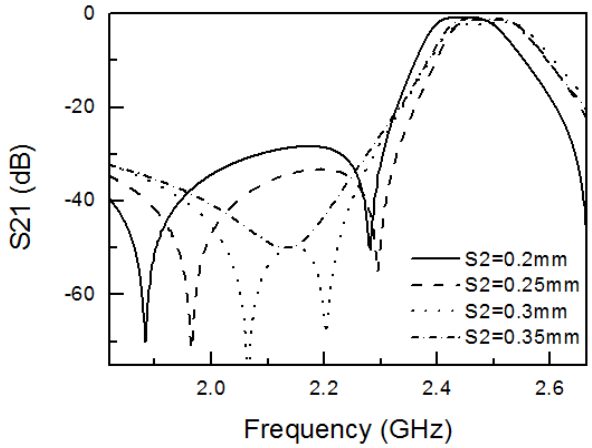

Fig. 9. Simulated scattering parameters of the filter B against s_2.

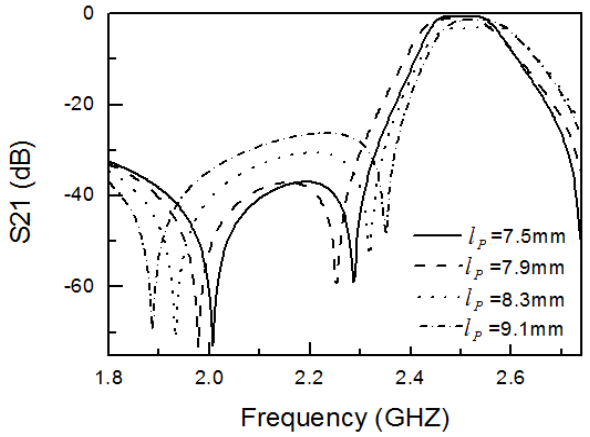

Fig. 10. Simulated scattering parameters of the filter B against l_p.

Figure 11 shows the photograph of the fabricated filter B. The measured and simulated results are shown in Fig. 12. The measured center frequency is at 2.45 GHz, and the 3 dB bandwidth is 4.6%. The minimum measured insertion loss is 1.8 dB, and the return loss is greater than 15 dB in the passband. Two transmission zeros are located at 2.04 and 2.15 GHz. The measured results have a good agreement with the full-wave simulations.

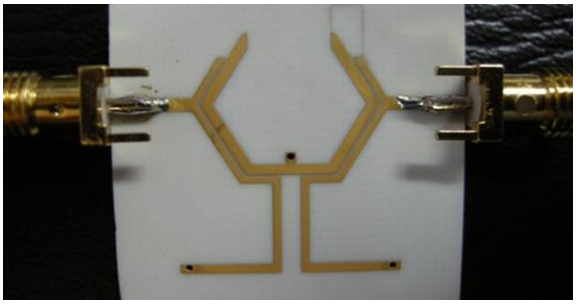

Fig. 11. Photograph of the fabricated filter B.

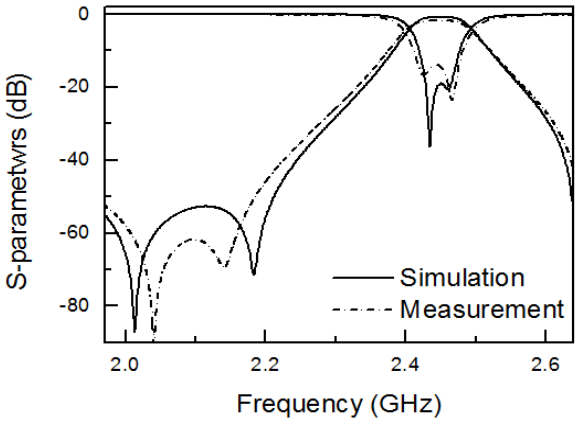

Fig. 12. Simulated and measured results of the filter B.

For the comparison with the previous investigations, Table 1 summarizes some dual-mode BPF performance characteristics. In the Table 1, the λg is the guided wavelength at the center frequency. It can be seen that the presented two dual-mode BPF shows miniature size when compared with the previous works.

Table 1: Comparison between the reference filters and the proposed filter

Reference	Center Frequency (GHz)	Insertion Loss (dB)	Return Loss (dB)	Filter Size
Ref.3	6.95	1.8	11.5	0.3λg×0.15λg
Ref. 5	2.4	2.0	15.5	0.25λg×0.16λg
Ref. 7	3.5	0.9	20	0.15λg×0.12λg
Ref. 9	4	1	15	0.51λg×0.51λg
This work	2.75	1.4	15	0.1λg×0.1λg
	2.45	1.8	15	0.1λg×0.12λg

IV. CONCLUSION

The novel compact pentagonal dual-mode filter with short-loaded is presented. The application of capacitive and inductive source-load coupling has been studied intensively to improve the performance in this paper. It reveals that a quasi-elliptic response with two adjustable transmission zeros is obtained for high rejection level in the stopband. The proposed structure and design method is verified by two sample filters.

ACKNOWLEDGMENT

This work is supported by "National Natural Science Foundation of China (Grant No. 61101042)".

REFERENCES

[1] I. Wolff, "Microstrip bandpass filter using degenerate modes of a microstrip ring resonator," *Electron. Lett.*, vol. 8, pp. 302-303, June 1972.

[2] B. F. Ganji and M. Samadbeik, "Simple configuration low-pass filter with very wide stop band," *ACES Express Journal*, vol. 1, no. 1, pp. 4-7, 2016.

[3] X. Deng, Z. Wang, K. D. Xu, and B. Yan, "Novel microstrip ultra-wideband bandpass filter using radial-stub-loaded structure," *ACES Express Journal*, vol. 1, no. 1, pp. 20-23, 2016.

[4] J. R. Lee and J. H. Cho, "New compact bandpass filter using microstrip λ/4 resonator with open stub inverter," *IEEE Microw. Guided Wave Lett.*, vol. 10, no. 12, pp. 526-527, Dec. 2000.

[5] T. Yan, X. H. Tang, and J. Wang, "A novel quad-band bandpass filter using short stub loaded E-shaped resonators," *IEEE Microwave & Wireless Components Letters*, vol. 25, no. 8, pp. 508-510, Aug. 2015.

[6] W.-H. Wu, "Compact double-mode cross-coupled microstrip bandpass filter with tunable transmission zeros," *IET Microw. Antennas Propag.*, vol. 2, no. 4, pp. 373-377, Dec. 2008.

[7] L. Gao and X. Y. Zhang, "High-selectivity dual-band bandpass filter using a quad-mode resonator with source-load coupling," *IEEE Microwave & Wireless Components Letters*, vol. 23, no. 9, pp. 474-476, Sept. 2013.

[8] J.-S. Hong and H. Shaman, "Dual-mode microstrip open-loop resonators and filters," *IEEE Trans. Microw. Theory Tech*., vol. 55, no. 8, pp. 1764-1770, Aug. 2007.

[9] W. Feng, X. Gao, and W. Che, "Bandpass filters with multiple transmission zeros using open/ shorted stubs," *IET Microw., Antennas Propag*.,vol. 9, no. 8, pp. 769-774, June 2015.

[10] B. Yu, B. Jia, and Z. Zhu, "Compact tri-band bandpass filter with stub-loaded stepped-impedance resonator," *Electron. Lett*., vol. 51, no. 9, pp. 701-703, Apr. 2015.

[11] Z. Zhu, S. Liang, and C. Wei，"Novel pentagonal dual-mode filters with adjustable transmission zeros," *ACES Express Journal*, vol. 31, no. 10, pp. 1238-1243, 2016.

Zhaojun Zhu was born in Sichuan, China, in 1978. He received the B.S. degree and the Ph.D. degree in Physical Electronics in UESTC, Chengdu, in 2002 and 2007 respectively. Since 2012, he has been an Associate Professor with the UESTC. His research interests include the design of microwave and millimeter-wave circuits.

Lu Cao was born in Jiangxi Province, China, in 1993. She received the B.S. degree in Physics from Gannan Normal University, in 2015, and is currently working toward the M.D. degree in UESTC. Her research interests include the design of microwave and millimeter-wave circuits.

Chaolei Wei was born in Shandong Province, China, in 1981. He received the B.S. degree from the Liaocheng University, in 2006, and the M.D. degree from the Institute of Southwest Physics, in 2009, respectively, and is currently working toward the Ph.D. degree in UESTC. His research interests include the design of microwave and millimeter-wave circuits.

Performance of Multiple-Feed Metasurface Antennas with Different Numbers of Patch Cells and Different Substrate Thicknesses

Niamat Hussain and Ikmo Park

Department of Electrical and Computer Engineering
Ajou University, Suwon 16499, Republic of Korea
ipark@ajou.ac.kr

Abstract ─ The design and performance of low-profile, multiple-feed metasurface antennas with different numbers of patch cells and different substrate thicknesses at a terahertz frequency are presented in this paper. The utilized antenna designs consist of a periodic array ($N \times M$) metallic square-patch metasurface and a planar feeding structure, which are both patterned on an electrically thin, high-permittivity GaAs substrate. The antenna gain increased in a linear fashion with an increasing number of patch cells, which were directly fed by the slit feedline. A 3-dB gain increment was observed irrespective of the substrate thickness when the number of patch cells was doubled. However, the 3-dB gain bandwidth as well as the radiation efficiency changed significantly with varying substrate thicknesses. The described antenna structure offers useful characteristics by means of a combination of different substrate thicknesses and patch numbers. In addition, the proposed antenna design features a number of benefits, including a low profile, mechanical robustness, easy integration into circuit boards, and excellent suitability for low-cost mass production.

Index Terms ─ Antenna array, metamaterials, metasurface, terahertz antennas, wide gain bandwidth.

I. INTRODUCTION

In recent years, metasurfaces have facilitated new approaches for manipulating the wavefronts of electromagnetic waves [1]. A metasurface is a two-dimensional structure that is composed of a periodic array of small scattering elements whose dimensions and periods are small when compared with the operating wavelength [2]. Due to their succinct planar structure, easy fabrication, and low cost, metasurfaces are widely used in the design of planar antennas. The main benefits of metasurface antennas are their ability to provide enhanced performance in terms of gain, radiation pattern, and bandwidth with an ultra-low profile design [3], [4]. The extraordinary properties of such antennas, which render them suitable for the application at hand, from the microwave to the terahertz band, have previously been presented [5]–[15].

In particular, researchers have focused on terahertz (THz) metasurface antennas, since the THz band has exhibited significant potential in relation to emerging applications in the fields of imaging, sensing, and astronomy, as well as defense and security [16]. This band offers many additional advantages, including an extremely high data transmission rate, wide bandwidth, high resolution, and improved spatial directivity with system compactness in wireless communication systems. Recently, a wide-gain-bandwidth metasurface antenna fed by a single open-ended, leaky-wave slit at terahertz frequencies was reported [17]. However, the higher atmospheric losses and attenuation of the THz band may restrict its usage due to its low gain. Therefore, low-profile antennas featuring high gain characteristics are highly recommended for terahertz applications.

Typically, planar antennas are coupled with lenses in order to realize high gain and wide bandwidth characteristics in the THz frequency range. Yet, lens-coupled antennas have a number of limitations, including their bulky size and low radiation efficiency [18]. Fabry-Perot antennas are designed to obtain a high gain, although such antennas face the design challenges associated with a low 3-dB gain bandwidth, especially when coupled with high-permittivity substrates [19]–[21]. THz antennas fed by slot waveguides also present high gain properties due to their low feeding losses. However, the manufacturing cost of such antennas is generally very high, since they usually consist of a complicated three-dimensional structure built with metallic walls [22], [23].

In this paper, we present the design of planar, low-profile, multiple-feed metasurface antennas with different numbers of patch cells and different substrate thicknesses in the THz frequency band in order to obtain high gain characteristics.

The remainder of this paper is organized as follows. Section II describes the geometry of the proposed antennas. Section III characterizes the detailed simulation setup as well as the conditions adopted during the numerical analysis of the antennas. Section IV presents

Submitted On: July 21, 2017
Accepted On: January 1, 2018

the antenna characteristics for different numbers of patch cells at different substrate thickness values. Finally, our conclusions are drawn in Section V.

II. SIMULATION SETUP

The majority of antenna analysis techniques can be categorized into two methods, namely a full-wave analysis method and an approximation method based on simplifying assumptions. The term "full-wave" generally refers to electromagnetic solutions that include all the applicable wave mechanisms. Such solutions allow for the implications of the boundary conditions to an accuracy limit, while the approximation methods do not enforce boundary conditions and thus do not consider surface wave effects, mutual coupling, or perhaps even radiation. Different analysis techniques and their respective limitations in terms of analyzing metasurfaces have previously been presented [24]. For high-frequency electromagnetic applications, full-wave time-domain simulation methods are highly desirable, especially when broadband results are required [25].

In our simulations, the full three-dimensional structures of the antennas were modeled, while the characteristics were investigated using the finite-integration time-domain commercial simulator CST Microwave Studio [26]. The antennas were excited by means of a discrete port located at the gap in the short dipole, which results in a default Gaussian-shaped excitation signal being passed into the gap in the slit line at its center. This setup guarantees the stability of the simulation regardless of the simulation time. A transient time-domain solver with a hexahedral mesh type was selected, while the accuracy level was set at -40 dB. This solver allows the complete characterization of the performance of antennas at multiple frequencies during one simulation run. The simulation time is inversely proportional to the size of the smallest mesh cell, which needs to be sufficiently fine to capture all the detail of the unit cell of the metasurface. In the simulation setup, the maximum mesh size was set at approximately 2.5 μm, which is one-twentieth of a free space wavelength at 0.3 THz. CST simulates each port independently, which means that the simulation time for each antenna is linearly proportional to its number of ports. Far-field monitors were set up for frequencies ranging from 0.3 THz to 0.42 THz. Moreover, open boundaries with some added space ($\lambda_o/4$) were used for the accurate calculation of the far-field results. The number of mesh cells in the computational domain for the antenna at H = 40 μm with a patch number of 5 × 5 was approximately 1.53×10^6, occupying 1.0 GB of memory. It took about 50 minutes when using 20 threads of parallelization in the Xeon E5-2660-V2 server with a clock speed of 2.2 GHz.

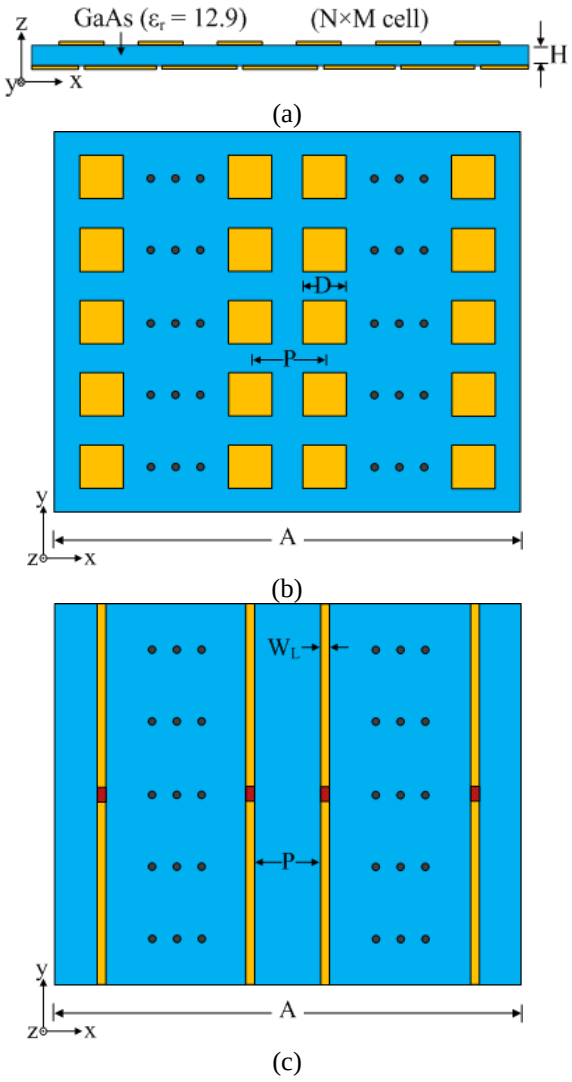

Fig. 1. Antenna geometry: (a) side view, (b) front view of top surface, and (c) front view of bottom surface.

Table 1: Common antenna design parameters

Parameter	Dimension (μm)
A	$5 \times P + D/2$
W_L	15
L_D	10
g	10

Table 2: Design parameters for different substrate thickness (H) values

Substrate thickness (H)	Periodicity (P)	Patch Length (D)
80 μm	330 μm	195 μm
40 μm	340 μm	200 μm
20 μm	360 μm	210 μm

III. ANTENNA GEOMETRY

The geometry of the proposed metasurface antenna with a multiple-feeding structure is shown in Fig. 1. The antenna was patterned on both sides of a GaAs substrate with a dielectric constant of ε_r = 12.9 and a loss tangent of $tan\delta$ = 0.006. The metasurface, which comprised an array of periodic $M \times N$ symmetrical metallic square patches, was patterned on the upper side of the substrate. The number of patches along the vertical axis (y-axis) was designated as M, while N represents the patches along the horizontal axis (x-axis). The periodicity and patch length of the square patch array were defined as P and D, respectively. The feeding structure, which comprised an array of open-ended, leaky-wave slits with a width of W_L, was etched on the lower side of the substrate. The number of feeding slits was equal to M, while the distance between the slits was P, which is equal to the periodicity (P) of the patch array. The chosen structure ensures the excitation of every patch column of the metasurface. The thickness and conductivity of the metal layer used in the ground plane and the patches were 0.35 μm and 1.6×10^7 S/m, respectively. The overall dimensions of the antenna were $A \times A \times H$ μm^3. Each feeding slit was fed by a short dipole at its center, which had a gap and a width of g and L_D, respectively. A discrete port was placed at the center of the feed gap of each slit in order to excite the antenna. The antenna was optimized at each substrate thickness value (H = 20 μm, H = 40 μm, and H = 80 μm) for different numbers of patch cells ($M \times N$) by changing only the periodicity and the patch size. The design parameters of the antennas that result in the optimum broadside gain and 3-dB gain bandwidth are summarized in Tables 1 and 2. The designed antenna can be realized by feeding it with a femtosecond laser pump. The laser pulses could be simultaneously focused on the short dipole gap of each slit of the antenna so as to achieve the advantages of a low profile, high gain, and wide bandwidth characteristics.

IV. ANTENNA CHARACTERISTICS

Figure 2 shows the performance of the multiple-feed metasurface antennas in terms of the boresight gain for different numbers of patch cells and various substrate thickness values. We fixed the number of patch cells along the vertical axis because the leaky-wave slit can effectively excite up to five patch cells. Increasing the number of patch cells in the vertical direction had no significant effect on the enhancement of antenna gain [27]. Thus, we fixed the number of patch cells in the vertical direction and only increased the number of patch cells in the horizontal direction. When the number of patch cells was increased from 5 × 3 to 5 × 6 to 5 × 12 for different substrate thickness values (H = 20 μm, H = 40 μm, and H = 80 μm), the antenna gain increased in a linear fashion. The gain increased in 3-dB increments regardless of the substrate thickness when the total number of patches was increased twice. The gain observed for 5 × 3 patch cells at H = 20 μm was 12.5 dBi, which increased to 15.5 dBi and 18.5 dBi when the number of patch cells was increased to 5 × 6 and 5 × 12, respectively. Similarly, at substrate thicknesses of H = 40 μm and H = 80 μm, the antenna gain increased from 13.5 to 19.5 dBi in a 3-dB increment when the number of patch cells increased from 5 × 3 to 5 × 6 and 5 × 12, respectively. These results showed that a peak gain occurs for each substrate thickness value, while the antenna gain increases with an increasing number of patch cells. Moreover, the central frequency shifted downwards for thicker substrates due to the increase in the effective dielectric constant. It was approximately 0.385 THz at H = 20 μm, although it shifted to 0.375 and 0.33 THz for H = 40 μm and H = 80 μm, respectively. It was interesting to observe that the 3-dB gain bandwidth and central frequency changed significantly with varying substrate thicknesses, whereas the patch number had a negligible influence on both. The 3-dB gain bandwidth was low, being approximately 8% and 10% for H = 20 μm and H = 80 μm, respectively, although it was wide, being almost 17.3% for H = 40 μm regardless of the patch number. In fact, the antennas with thick substrates faced the design challenges associated with a low 3-dB gain bandwidth at terahertz frequencies due to the substrate resonance. This problem can be solved by reducing the substrate thickness to $\lambda_o/20$, where λ_o, is the free-space wavelength [28]. A substrate thickness of 40 μm is approximately $\lambda_o/20$ with respect to its central operating frequency. Hence, it exhibited the wide gain bandwidth.

Figure 3 presents the radiation efficiency of the multiple-feed metasurface antennas with different numbers of patch cells at various substrate thickness values. The radiation efficiency increased with an increasing substrate thickness, although it was not affected by different patch numbers (5 × 3, 5 × 6, and 5×12), especially within the 3-dB gain bandwidth. The radiation efficiency calculated for H = 20 μm was 57%, which increased to 73% and 85% for H = 40 μm and H = 80 μm, respectively. It was observed that the number of patch cells only influenced the gain enhancement, without significantly changing the other antenna characteristics, whereas the substrate thickness determined both the 3-dB gain bandwidth and the radiation efficiency. This therefore provides a simple method for determining the specific antenna characteristics in terms of both gain and bandwidth by choosing a specific combination of patch number (M×N) and substrate thickness.

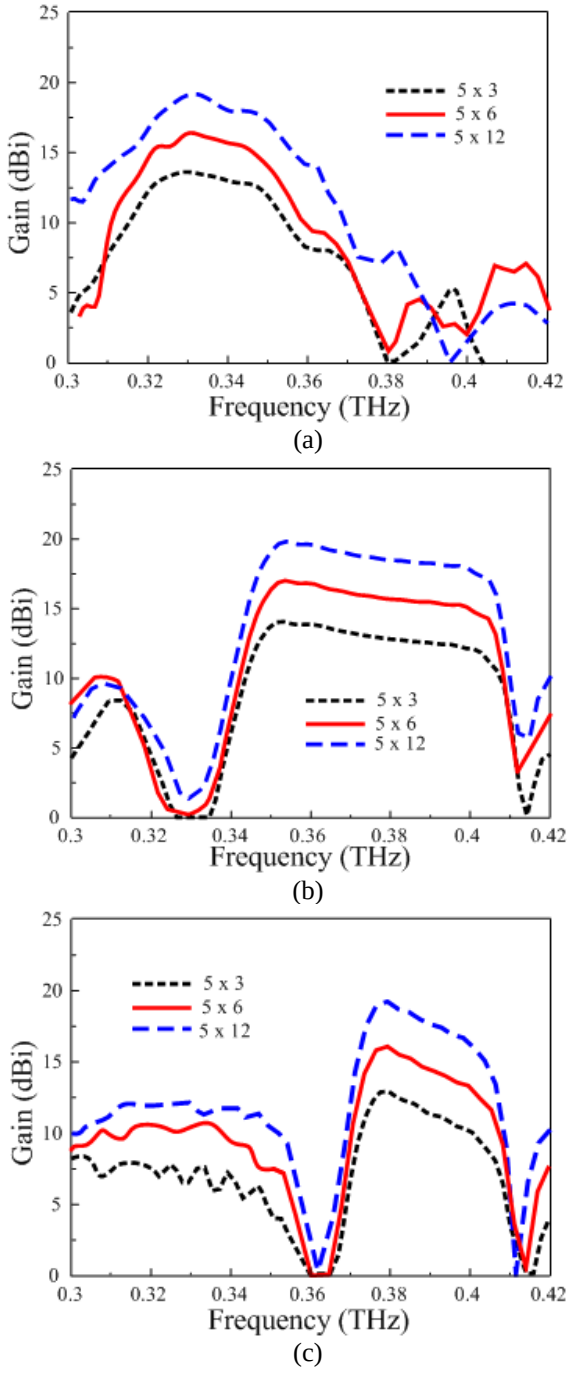

Fig. 2. Antenna gain with different numbers of patch cells and different substrate thicknesses: (a) H = 80 μm, (b) H = 40 μm, and (c) H = 20 μm.

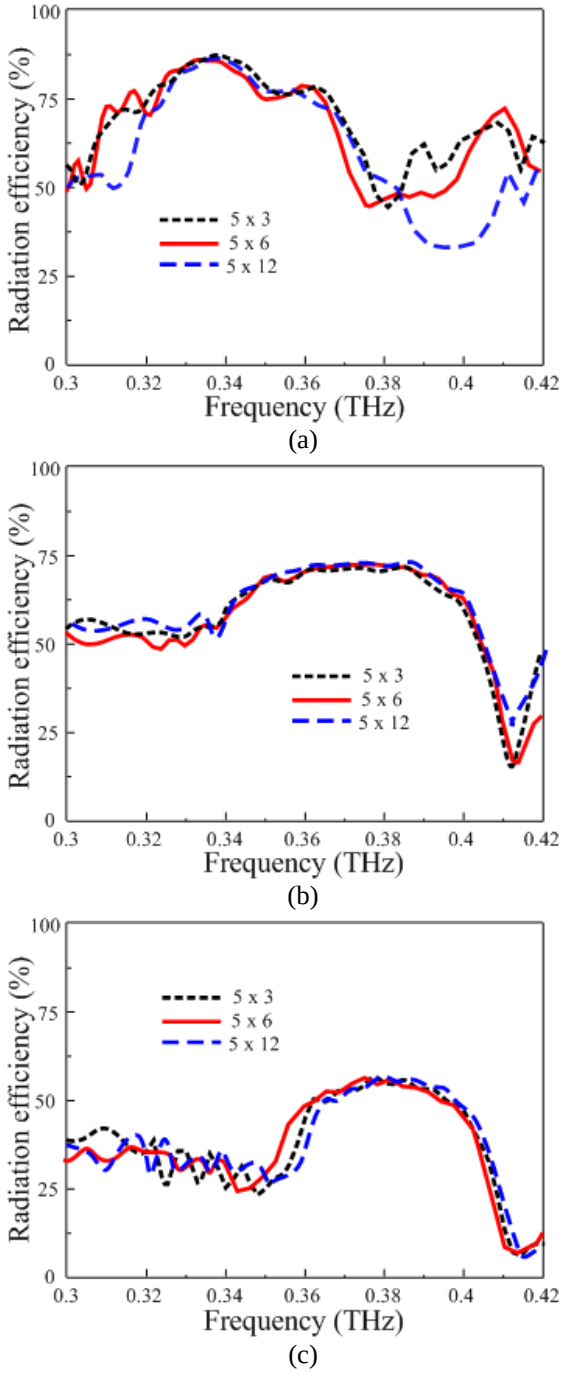

Fig. 3. Antenna radiation efficiency with different numbers of patch cells and different substrate thicknesses: (a) H = 80 μm, (b) H = 40 μm, and (c) H = 20 μm.

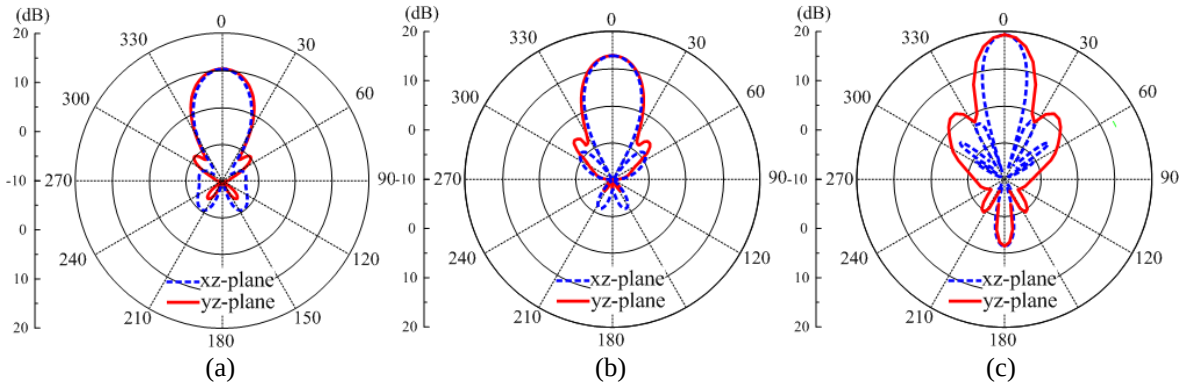

Fig. 4. Antenna radiation patterns for different numbers of patch cells at H = 80 μm: (a) 5×3, (b) 5×6, and (c) 5×12.

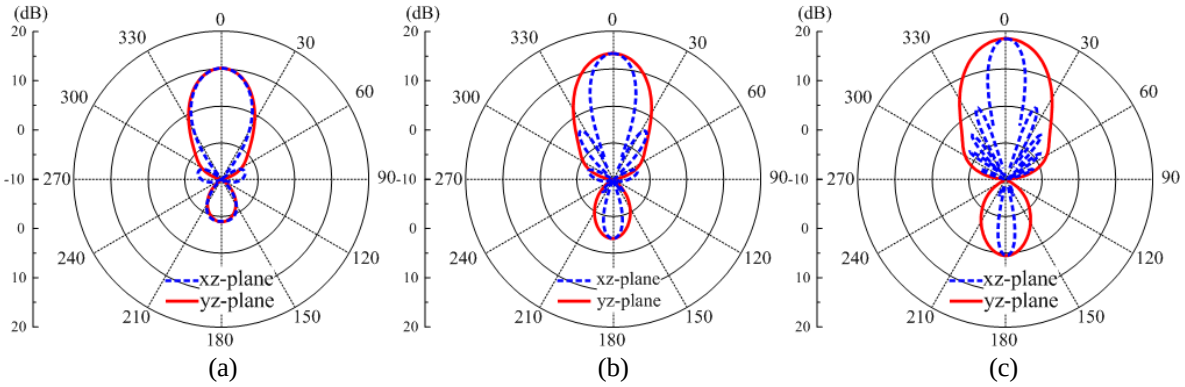

Fig. 5. Antenna radiation patterns for different numbers of patch cells at H = 40 μm: (a) 5×3, (b) 5×6, and (c) 5×12.

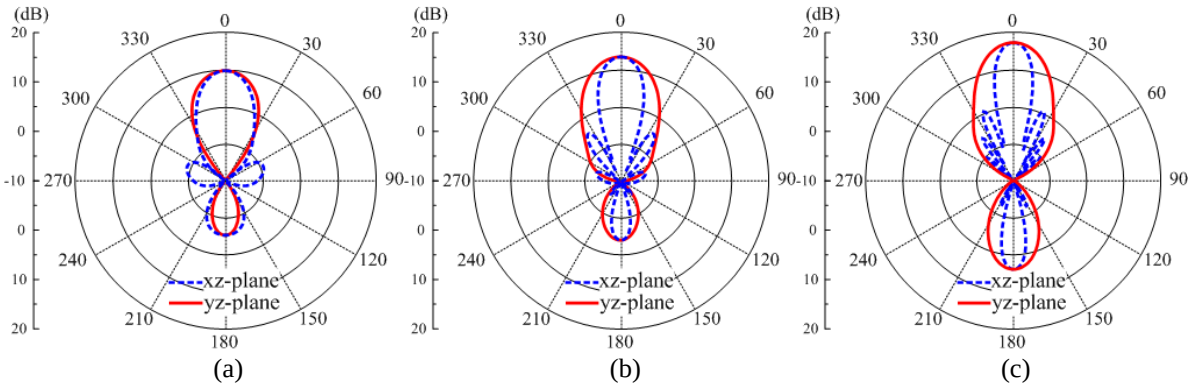

Fig. 6. Antenna radiation patterns for different numbers of patch cells at H = 20 μm: (a) 5×3, (b) 5×6, and (c) 5×12.

The radiation patterns of the metasurface antennas with different substrate thicknesses and different patch numbers were plotted at their central frequencies as shown in Figs. 4–6. All the antennas exhibited directive radiation patterns with low sidelobe and backlobe levels in both the *xz*- and *yz*-planes. Generally, the *yz*-plane showed clean profile patterns with lower sidelobe levels when compared to the *xz*-plane. Furthermore, the number of sidelobe levels in the *xz*-plane increased with an increasing number of patch cells. The antennas yielded low back radiation throughout the entire gain bandwidth due to the successful implementation of the metasurface, even though the leaky-wave slit is open to free space. However, the gain value associated with both

back radiations increased with an increase in the number of patch cells. Interestingly, the back radiation decreased when the substrate thickness increased.

V. CONCLUSION

The design of multiple-feed metasurface antennas with different numbers of patch cells and different substrate thicknesses, as well as the associated radiation characteristics, were studied over the THz frequency band. The antennas were composed of a patch array and multiple feeding structures, both of which were patterned on a high-permittivity, electrically thin GaAs substrate. Regardless of the substrate thickness, the antenna gain increased linearly in increments of 3 dB when the number of patches was increased twice. The radiation efficiency and 3-dB gain bandwidth were mainly determined by the substrate thickness. The 3-dB gain bandwidth was 7%, 17.3%, and 10% for the substrate thicknesses of H = 20 μm, H = 40 μm, and H = 80 μm, respectively. The radiation efficiency increased with increasing substrate thickness. The efficiency was calculated as 57% at H = 20 μm, and it increased to 73% for H = 40 μm and 85% for H = 80 μm. The different combinations of patch numbers and substrate thicknesses provide freedom in terms of choosing the desired gain values and 3-dB gain bandwidth for various antenna applications, which increases their value for THz applications. Furthermore, these antennas offer a number of other promising features, including a low profile, mechanical robustness, suitability for low-cost mass production, and easy integration into circuit boards.

ACKNOWLEDGMENTS

This work was supported in part by Institute for Information & Communications Technology Promotion (IITP) grant funded by the Korea government (MSIP) (No. 2017-0-00959, University ICT Basic Research Lab), in part by "Human Resources Program in Energy Technology" of the Korea Institute of Energy Technology Evaluation and Planning (KETEP), granted financial resource from the Ministry of Trade, Industry & Energy, Republic of Korea (No. 20164030201380), and in part by the National Research Foundation of Korea (NRF) grant funded by the Korea government (MEST) (2016R1A2B100932).

REFERENCES

[1] N. Yu and F. Capasso, "Flat optics with designer metasurfaces," *Nat. Mater.*, vol. 13, no. 2, pp. 139-150, 2014.

[2] J. P. Turpin, J. A. Bossard, K. L. Morgan, D. H. Werner, and P. L. Werner, "Reconfigurable and tunable metamaterials: A review of the theory and applications," *Int. J. Antennas Propag.*, vol. 2014, 429837, pp. 1-18, 2014.

[3] Y. Dong and T. Itoh, "Metamaterial-based antennas," *Proc. IEEE*, vol. 100, no. 7, pp. 2271-2285, 2012.

[4] C. L. Holloway, E. F. Kuester, J. A. Gordon, J. O'Hara, J. Booth, and D. R. Smith, "An overview of the theory and applications of metasurfaces: The two-dimensional equivalents of metamaterials," *IEEE Antennas Propag. Mag.*, vol. 54, no. 2, pp. 10-35, 2012.

[5] M. Koutsoupidou, I. S. Karanasiou, and N. Uzunoglu, "Rectangular patch antenna on split-ring resonators substrate for THz brain imaging: Modeling and testing," *IEEE Int. Conf. on Bio-informatics and Bioengineering*, Chania, Greece, pp. 1-4, Nov. 2013.

[6] M. E. Badawe, T. S. Almoneef, and O. M. Ramahi, "A true metasurface antenna," *Sci. Rep.*, vol. 6, 19268, pp. 1-8, 2016.

[7] H. Zhou, J. Dong, S. Yan, Y. Zhou, and X. Zhang, "Generation of terahertz vortices using metasurface with circular slits," *IEEE Photon. J.*, vol. 6, no. 6, 5900107, pp. 1-7, 2014.

[8] Q. Zhang, L. Si, Y. Huang, X. Lv, and W. Zhu "Low-index-metamaterial for gain enhancement of planar terahertz antenna," *AIP Adv.*, vol. 4, no. 3, 037103, pp. 1-7, 2014.

[9] Y. Huang, L. Yang, J. Li, Y. Wang, and G. Wen, "Polarization conversing of metasurface for the application of wide band low-profile circular polarization slot antenna," *Appl. Phy. Lett.*, vol. 109, 054101, pp. 1-5, 2016.

[10] N. Nasimuddin, Z. N. Chen, and X. Qing, "Bandwidth enhancement of a single-feed circularly polarized antenna using a metasurface: Metamaterial-based wideband CP rectangular microstrip antenna," *IEEE Antennas Propag. Mag.*, vol. 58, no. 2, pp. 39-46, 2016.

[11] X. Gao, X. Han, W. P. Cao, H. F. Ma, H. O. Li, and T. J. Cui, "Ultrawideband and high-efficiency linear polarization converter based on double v-shaped metasurface," *IEEE Trans. Antennas Propag.*, vol. 63, no. 8, pp. 3522-3530, 2015.

[12] A. Mahmood, G. O. Yetkin, and C. Sabah, "Wideband negative permittivity and double negative fishnet-mushroom-like metamaterial in x-band waveguide," *Int. J. Antennas Propag.*, vol. 2017, 2439518, pp. 1-7, 2017.

[13] S. I. Rosaline and S. Raghavan, "Metamaterial inspired square ring monopole antenna for WLAN applications," *ACES Express J.*, vol. 1, no. 1, pp. 32-35, 2016.

[14] A. Shater and D. Zarifi, "Radar cross section reduction of microstrip antenna using dual-band metamaterial absorber," *ACES J.*, vol. 32, no. 2, pp. 135-140, 2017.

[15] P. Rocca and A. F. Morabito, "Optimal synthesis of reconfigurable planar arrays with simplified architectures for monopulse radar applications," *IEEE Trans. Antennas Propag*., vol. 63, no. 3, pp. 1048-1058, 2015.
[16] P. H. Siegel, "Terahertz technology," *IEEE Trans. Microw. Theory Tech*., vol. 50, no. 3, pp. 910-928, 2002.
[17] N. Hussain and I. Park, "Terahertz planar wide-gain-bandwidth metasurface antenna," *Int. Workshop on Metamaterials-by-Design*, Riva del Garda, Italy, pp. 1-2, Dec. 2016.
[18] N. Hussain, T. K. Nguyen, H. Han, and I. Park, "Minimum lens size supporting the leaky-wave nature of slit dipole antenna at terahertz frequency," *Int. J. Antennas Propag.*, vol. 2016, 5826957, pp. 1-8, 2016.
[19] N. Hussain, K. E. Kam, and I. Park, "Performance of a planar leaky-wave slit antenna for different values of substrate thickness," *J. Electromagn. Eng. Sci*., vol. 17, no. 4, pp. 202-207, Oct. 2017.
[20] T. K. Nguyen, B. Q. Ta, and I. Park, "Design of a planar, high-gain, substrate-integrated Fabry-Perot cavity antenna at terahertz frequency," *Curr. Appl. Phys.*, vol. 15, no. 9, pp. 1047-1053, 2015.
[21] N. Hussain, T. K. Nguyen, and I. Park, "Performance comparison of a planar substrate-integrated Fabry-Perot cavity antenna with different unit cells at terahertz frequency," in *IEEE European Conf. on Antennas and Propagation*, Davos, Switzerland, pp. 1-4, Apr. 2016.
[22] K. M. Luk, S. F. Zhou, Y. J. Li, F. Wu, K. B. Ng, C. H. Chan, and S. W. Pang, "A microfabricated low-profile wideband antenna array for terahertz communications," *Sci. Rep*., vol. 7, 1268, pp. 1-11, 2017.
[23] C. Gu, S. Gao, and B. Sanz-Izquierdo, "Low-cost wideband low-THz antennas for wireless communications and sensing," in *UK-Europe-China Workshop on Millimetre Waves and Terahertz Technologies*, Liverpool, UK, pp. 1-4, Sep. 2017.
[24] F. Costa, A. Monorchio, and G. Manara, "An overview of equivalent circuit modeling techniques of frequency selective surfaces and metasurfaces," *ACES J*., vol. 29, no. 12, pp. 960-976, Dec. 2014.
[25] A. Taflove and S. C. Hagness, *Computational Electromagnetics: The Finite-Difference Time-Domain (FDTD) Method*. Artech House, 3rd ed., 2005.
[26] CST Microwave Studio, https://www.cst.com/
[27] N. Hussain and I. Park, "Design of a wide-gain-bandwidth metasurface antenna at terahertz frequency," *AIP Adv*., vol. 7, no. 5, 055313, pp. 1-8, 2017.
[28] B. A. Munk, *Frequency Selective Surfaces: Theory and Design*. Wiley, New York, 2000.

Niamat Hussain received his B.S. degree in Electronics Engineering from Dawood University of Engineering and Technology, Karachi, Pakistan, in 2014. He is currently studying for his M.S. degree at the Department of Electrical and Computer Engineering at Ajou University, Suwon, Republic of Korea. His research is mainly focused on lens-coupled antennas, metasurface antennas, and terahertz antennas.

Ikmo Park received his B.S. degree in Electrical Engineering from the State University of New York at Stony Brook and his M.S. and Ph.D. degrees in Electrical Engineering from the University of Illinois at Urbana-Champaign. He joined the Department of Electrical and Computer Engineering at Ajou University in 1996. Prior to joining Ajou University, he was with the Device and Materials Laboratory, LG Corporate Institute of Technology, Seoul, Republic of Korea, where he was engaged in research and development of various antennas for personal communication systems, wireless local area networks, and direct broadcasting systems. He has authored and co-authored over 300 technical journal and conference papers. He also holds over 30 patents. His current research interests include the design and analysis of microwave, millimeter-wave, terahertz wave, and nano-structured antennas.

Characterization of Spatial Reflection Co-efficient for Ground-to-Aircraft and Satellite-to-Aircraft Communication

Muhammad-Yasir Masood Mirza [1], Noor M. Khan [1], Abid Jamal [1], and Rodica Ramer [2]

[1] Department of Electrical Engineering
Capital University of Science and Technology, Islamabad, 44000, Pakistan
yasir@arwic.com, abidjamal010@gmail.com, noor@ieee.org

[2] School of Electrical Engineering and Telecommunications
University of New South Wales (UNSW), Sydney, Australia
ror@unsw.edu.au

Abstract ─ Because of high sensitivity and long range capability in modern radars, Radar Cross-Section (RCS) is considered to be one of the most important factors in the performance evaluation of stealth technology and for defense applications, especially those that deal with airborne weapon system. In this paper, a concrete relationship is established between RCS and spatial reflection coefficient (SRC) for the two proposed scenarios, i.e., Satellite-to-Aircraft and Ground-to-Aircraft. Geometrical models of the two proposed scenarios are presented for the evaluation of correct incident angles of impinging waves on the surface of aircraft and their corresponding RCS observations. For numerical computation of RCS, a simulation tool POFACET® [1] based upon the methodology of Physical Optics (PO) and a FACET-based aircraft A380 model is used for the designed scenarios. In both the scenarios, the result shows that the aircraft has strong signal reflecting properties which results in the form of RCS to radar receiver or neighboring aircrafts. Further, the RCS results are used to evaluate the spatial reflection coefficients of scattered signal received at any neighboring signal receiving unit. Comparison between RCS and SRC validates that these terms have similar scattering behavior and can be used interchangeably for performance evaluation of communication system models. From the result, it is evident to mention that flying aircrafts are one prominent source of interference which may provide interference to its neighboring aircrafts and as a result degrades their communication performance.

Index Terms ─ Bistatic radar cross-section, ground-to-aircraft, physical optics, radar cross-section, satellite-to-aircraft.

I. INTRODUCTION

RADAR (RAdio Detecting And Ranging) is a device that reveals the presence of a target within its range of coverage. The post-processing capability of a RADAR on the received reflected Electromagnetic (EM) waves (echos or radar returns) extracts the information of the target's direction, range, velocity, orientation and other classifying characteristics. When the radar's transmitted EM waves impinge on target's surface, the reflecting surface of the object radiates EM energy in all directions. The radiated energy depends upon the target size, physical shape, orientation and reflecting properties of the surface. These all can be put together to specify target's identification parameter known as Radar Cross Section (RCS). Quantitatively, it can be termed as a fictitious surface area which explains the intensity of EM wave reflected back to the radar's receiver antenna. The RCS is a measure of an object's reflecting ability which exploits the visibility of the intended target towards the RADAR. Due to high sensitivity and long range capability in modern RADARs, RCS is considered as one of the most important factors in the performance evaluation of stealth technology and for airborne weapon systems [2,3]. In the designing of modern fighter aircraft, the performance of stealth technology and the visibility of an aircraft highly depend on the results and measurements of RCS. In order to accurately predict the RCS of a target, it is necessary to analyze the factors that affect its behavior, such as material, incident angle, radar signals wavelength, size of the target, radar operating frequency and target's orientation.

The correct evaluation of the RCS and its prediction is imperative in designing of high-performance radars as well as for aircrafts having low visibility (stealth) towards the radar. Such problems deal with the

Submitted On: May 31, 2017
Accepted On: October 4, 2017

techniques available in electromagnetic computational theory. It is well established from the literature that the behavior of electric and magnetic fields is governed by Maxwell's equations. In the literature, two main computational electromagnetic methods have been developed to deal with the electromagnetic problems: time-domain methods and frequency-domain methods. As both of the domains interrelate with each other by the Fourier transform which makes them different in solution procedure, therefore, both possess different strengths and applicabilities. In the problems, when it is required to observe the electromagnetic scattering from objects larger than the wavelength, the weak convergence properties of solutions based on Rayleigh's method make it desirable to use high-frequency asymptotic methods [4]. Moreover, the approximation procedure of high-frequency asymptotic (HFA) techniques make it prevalent to be used for a large group of problems as compared to those which can be handled with low-frequency methods. Applying computational electromagnetic method in frequency-domain requires a solution of system of linear equations for each frequency and once the solution matrix is inverted or factorized, it can be used repeatedly to obtain the solutions of all excitations. This makes frequency-domain methods attractive for problems in which it is required to consider many excitations [4]. HFA techniques [5,6] such as Physical Optics (PO), Geometric Optics (GO), Physical Theory of Diffraction (PTD) and the Geometrical Theory of Diffraction (GTD) require correct modeling of the object geometry. These approaches incorporate scattering mechanisms to estimate the reflectivity of the target in both qualitative and quantitative manner. Since, it is not possible to acquire the exact dimensions of the intended object always, therefore, in such cases the requirement of geometry limits the applicability of HFA techniques. On the other hand, numerical approaches include Method of Moments (MoM) [7], the Fast Multipole Method (FMM) [8], the Finite Difference Time-Domain (FDTD) [9,10] Method and Transmission-line Matrix (TLM) [11]. In comparison to HFA techniques, numerical approaches are geometry-independent and of a general nature which can be applied to any object within the limitations of computer processing capability.

In [12], the authors fitted the Chi-square distribution on aircraft's RCS measurements by evaluating its statistical parameters. From the results, it was concluded that the statistical parameters have a strong dependency on radar operating frequency, the geometry of the aircraft and on aspect angles. On the basis of these statistics, aircraft detection probabilities were also estimated and concluded with the fact that the average value of RCS highly effects the detection probability than the normalized value of RCS. In [13], the authors measured RCS of commercial aircrafts along different flight routes to observe the impact of RCS fluctuations with respect to aspect angles and their dependency on the classification of aircrafts. From the results, it was concluded that the change in aspect angle substantially influence RCS measurements and as a result provides fluctuations in RCS. In situations, when the wavelength of radar's signal is smaller than object's dimension, it will provide higher rate of fluctuations in RCS. Hence, for correct modeling and simulations, spatial RCS variations must be incorporated. In [14], the authors presented an implementation procedure of measuring RCS of aircraft and pointed some essential tradeoffs between its accuracy and computational cost in modeling and simulation of RCS related applications. Seven interpolation schemes were considered for the generation of continuous RCS samples, among them spline interpolation method was proved best for originating new data points with less interpolation error. To accelerate the computation efficiency of monostatic RCS, a number of fast and efficient interpolation techniques have been reported in the literature [15-19] to reduce the time and memory requirement of RCS calculations.

It is evident from the literature that a signal received at the receiver not only contains a direct Line-of-Sight (LoS) signal component but also contains multiple reflected copies of the transmitted signal that arrive at the receiver with different delays [20]. The delayed reflected copies are basically the result of reflections, refraction, diffraction or scattering from terrains, trees, mountain or in fact anything present between the transmitter and receiver ends. The reflectance properties of every object vary depending upon its permittivity and permeability levels. Furthermore, the relation between reflected and incident field is usually described by Fresnel equations, which depends upon the permittivity, conductivity of the surface and frequency, incident angle and polarization of the incident waves. Hence, the reflection coefficient better describes the amount of radiated energy in one term by accumulating all the reflecting properties of the surface and the wave. Being the same signal reflecting phenomenon, the signal transmitted through satellites/ ground stations towards an aircraft of interest may get reflected through its proximate aircrafts. As a result, the aircrafts flying in the proximity of aircraft of interest will act as scatterers and will provide interfering signals which may degrade the communication performance. This concept can be legitimized by analyzing the work performed in [21]. Prior to this work, it was generally assumed that the signal reflection from the taxing aircrafts at airports provides interference to the Instrument Landing System (ILS) localizer which degrades its localization efficiency;however,no measurement campaign was conducted to validate/invalidate this thought. In [21], the authors presented a scaled measurement setup to evaluate the quantitative measure of interference to an ILS-localizer due to reflections from large-size aircrafts like Airbus® A380 and Boeing® B747 aircrafts. The

bistatic RCS results show that both the aircrafts provide interference to ILS-localizer, however, A380 tends to have a slightly larger disturbing influence to ILS-localizer as compared to B747. Thus reflections of signals from the aircraft's body can be interpreted as a main source of interference in satellite-to-aircraft communication and ground-to-aircraft communication, in which the flying aircrafts act as scatters. Since, the RCS and the reflected signals from the aircraft's body gives the same concept, therefore, a relationship can easily be made between these two terms. Both the terms depend on the incidence angle, material properties, signaling frequency, polarization and observation angle. In literature, a lot of work has been proposed to acquire the correct estimation of the RCS of aircrafts; however, no work has yet been proposed to establish relationship between RCS and reflection coefficient for ground-to-aircraft and satellite-to-aircraft communication scenarios. Moreover, no concrete relationship has been established so far between the RCS and SRC for a targeted body.

In this article, a new term named as Spatial Reflection Coefficient (SRC) is defined and then a concrete relationship of the interdependence between RCS and SRC is formulated. The relationship between RCS and SRC relates two different terms which are being used differently in two different fields of research. Both the terms are inter-dependent on each other and utilize the same input parameters like incidence angle, material properties, signaling frequency, polarization and observation angle. The RCS basically describes an effective area of a targeting object that intercepts the incoming signals transmitted through RADAR antenna and isotropically radiates the incident power in all directions. The ability of target's reflecting and its size are described with term RCS. However, on the other hand, the reflection coefficient is a qualitative parameter that describes surface reflecting ability and gives the amount of reflected electromagnetic wave due to impedance discontinuity in the transmission medium between the transmitter and receiver. The proposed relationship interrelates the RCS and the SRC which interchangeably help to extract the reflectivity information of a target's surface on the basis of observed RCS. Moreover, this interchangeability between the RCS and SRC will help researchers of the different fields and will allow them to utilize simulation tools and algorithms of both the domains interchangeably. For example, the researcher from the communication systems will be able to get the reflection properties of the scattering objects with the help of RADAR simulation tools. Aircraft's body reflecting/scattering properties are analyzed by designing geometrical models of two scenarios, satellite-to-aircraft and ground-to-aircraft. The proposed geometrical models help to evaluate the correct incident angles of incoming EM waves impinging on aircraft's surface. Bistatic RCS results are obtained by incorporating a facet-based model of aircraft A380 and a simulation tool POFACET® [1]. For proposed geometrical models, bistatic RCS results are obtained and analyzed with respect to observation angles. Furthermore, the spatial reflection coefficients behavior is analyzed as a function of bistatic RCS and propagation distances of incoming and reflecting signals.

The rest of the paper is organized as follows. Section 2 presents methodology to develop a relationship between the RCS and SRC. The proposed geometry for two scenarios satellite-to-aircraft and ground-to-aircraft is presented in Section 3, to evaluate correct incident angles of impinging EM waves on the aircraft's body. In Section 4, the details of simulation tool and aircraft's facet-based model are given. In Section 5, simulation results of each incident angles evaluated in Section 3 are presented and analyzed in detail. Moreover, the behavior of the relationship between the RCS and SRC is also analyzed in Section 5. Finally, Section 6 concludes the paper.

II. RELATIONSHIP OF SPATIAL REFLECTION COEFFICIENT AND RCS

A. Radar cross section

In radar systems, RCS is a measure which defines the amount of scattered or reflected energy from the surface of a target towards the receiver antenna. If the locations of both the transmitter and receiver are identical then it is referred as monostatic RCS; however, in the cases when the locations are non-identical it is interpreted as Bistatic RCS (BRCS). Both the terms are identical in scattering methodology except the inclusion of bistatic angle in BRCS which makes it more complex than monostatic RCS. In terms of complex electric field amplitudes, the RCS ($\boldsymbol{\sigma_B}$) is defined as follows [22,23]:

$$\boldsymbol{\sigma_B}(\boldsymbol{\phi_i}, \boldsymbol{\theta_i}, \boldsymbol{\phi}, \boldsymbol{\theta}) = \lim_{\boldsymbol{R}\to\infty} 4\pi \mathbf{R}^2 \frac{|\boldsymbol{E_s}|^2}{|\boldsymbol{E_i}|^2}, \quad (1)$$

where, $\boldsymbol{R}$ is the distance between the target and the receiver antenna, and $\boldsymbol{E_s}$ and $\boldsymbol{E_i}$ are the complex amplitudes of the incident and the scattered electric fields respectively. Spherical angle coordinates $(\boldsymbol{\phi_i}, \boldsymbol{\theta_i})$ and $(\boldsymbol{\phi}, \boldsymbol{\theta})$ represents incident angles of incoming wave and reflected wave respectively.

B. Spatial reflection coefficient

In electromagnetic wave theory, reflection of a signal is one important phenomenon which occurs when the wave impinges on a reflective surface having a large dimension compared to its wavelength. When a signal reaches the receiver through different propagation paths, such environment is known as multipath environment. The relation between reflected and incident field is usually described by Fresnel equations, which depends upon the permittivity, conductivity of the surface and frequency, incident angle, polarization of the incident

wave. Reflection of a radio wave possesses directional property which can be further categorized into two types of reflections, specular reflection and diffuse reflection. In specular reflections, the angle of the reflected path is relatively constant to the angle of the incident wave; however, the diffuse reflections have random phase relative to the angle of the incident wave due to irregularities of the surface. In both the cases, the induced path loss varies on the basis of reflection coefficients which depends upon the dielectric characteristics of the reflective surface. For specular reflections, the path loss is obtained by using Fresnel equations while for diffused/scattered reflections a diffused scattering coefficient is multiplied with specular reflection coefficient [24-26]. The scattered reflections possess a unique spatial properties based upon reflecting angles of the wave from the scattering surface. Based upon the spatial characteristics of the scattered waves, we introduce a new parameter SRC as an addition to earlier terms elaborating reflection phenomenon of radio waves. SRC is defined as the ratio of the complex electric field intensity of the incident wave to that of the reflected wave electric field intensity in a specific direction:

$$\boldsymbol{\Gamma = \frac{E_s}{E_i}}. \tag{2}$$

This can also be represented as:

$$\boldsymbol{\Gamma = \rho_0 e^{-j\theta}}, \tag{3}$$

where, $\boldsymbol{\rho_0 = |\Gamma|}$ represents magnitude of the spatial reflection coefficient and varies between $\boldsymbol{0 \leq \rho \leq 1}$, $\boldsymbol{\theta}$ is the phase angle of the reflection which presents phase change of the reflection and varies between.$\boldsymbol{-\pi \leq \theta \leq \pi}$. The amplitude value of the reflection coefficient is considered as a composite representation of three independent factors i.e reflection coefficient of smooth surface, roughness coefficient and diffusion factor. These three terms highly influence on the scattering properties of a surface and compositely defines the nature of a reflection coefficient [27].

C. Relationship of spatial reflection coefficient and RCS

Since Radar Cross Section and the spatial reflection coefficient are interdependent on each other; therefore, a relationship can be easily made between these two terms. Both RCS and SRC depend on the incidence angle, material properties, signaling frequency, polarization and observation angle. In order to develop a relation between RCS and SRC, we have assumed a typical bistatic geometry of signal reflection from the surface of an aircraft towards another aircraft present in the surroundings. As illustrated in Fig. 1, the aircraft (A_1) located at radial distance d_1 from radar transmitting antenna reflects the intercepted signal towards an aircraft (A_2) present at distance d_2. Referring Fig. 1, the received power density at distance d_1 is calculated as:

$$P_d = \frac{P_t G_t}{4\pi d_1^2}, \tag{4}$$

where P_t denotes peak transmitted power and G_t is the gain of the radar transmitting antenna. Considering the methodology of bistatic radar cross section, the total reflected/scattered power received at aircraft (A_2) can be calculated as [28]:

$$(P_r)_{ref} = \frac{P_t G_t A_e \sigma_B(\phi_i, \theta_i, \phi, \theta)}{(4\pi)^2 d_1^2 d_2^2}, \tag{5}$$

where A_e is the effective aperture of the receiver antenna, $\sigma_B$is the bistatic RCS of the aircraft A_1 and d_2 is the distance/range of aircraft A_2 from A_1. In terms of spatial reflection coefficient denoted by Γ, the total reflected/scattered power received at aircraft A_2 can be written as [24,25]:

$$\boldsymbol{(P_r)_{ref} = \frac{P_t G_t A_e \Gamma^2}{4\pi(d_1 + d_2)^2}}. \tag{6}$$

Both the expressions presented in Eq. (5) and Eq. (6) are equivalent in nature and thus can be compared to formulate a relation between the RCS and SRC. Solving both expressions yields a final look of the relationship between the magnitude of spatial reflection coefficient (SRC) and RCS:

$$\boldsymbol{|\Gamma| = \frac{(d_1 + d_2)}{d_1 d_2} \sqrt{\frac{\sigma_B(\phi_i, \theta_i, \phi, \theta)}{4\pi}}}. \tag{7}$$

From the expression, it is notable that SRC is directly proportional to the square root of the RCS multiplied by a constant multiple based upon the path lengths of incident and reflected path.

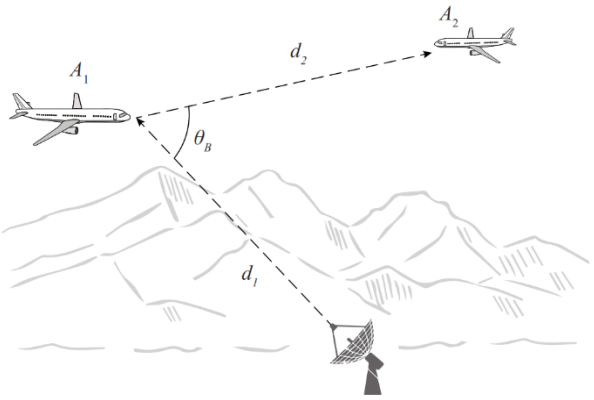

Fig. 1. An illustrative geometry of bistatic signal reflection from the surface of aircraft A_1 on to aircraft A_2.

III. SYSTEM MODEL

A. Satellite-to-aircraft scenario

Communication through satellites is one effective resource of relaying radio signals between two different points on the earth, whether on the ground, at oceans or in the air. In recent years, satellites have become a

vital part in many fields with a variety of applications like navigation, communication, weather and earth observation, etc. Moreover, satellite communication plays an important role to fulfill human needs of requiring in-flight TV and internet access during their on-the-air spare time. A signal transmitted through satellite to an aircraft may get reflected/scattered from the aircraft's surface with a fractional decrease in incident signal's power depending upon the properties of aircrafts surface. The reflected signal may reach to aircraft's neighboring signal receivers (i.e. satellites, radars or aircrafts), which may degrade their communication performance due to interfering reflected signals. In order to evaluate RCS/SRC of EM signals, a satellite-to-aircraft scenario is assumed. Due to high bandwidth and coverage over a large geographical area, geostationary satellites are considered which usually travel at an altitude of approximately 35,800 Km /sec.

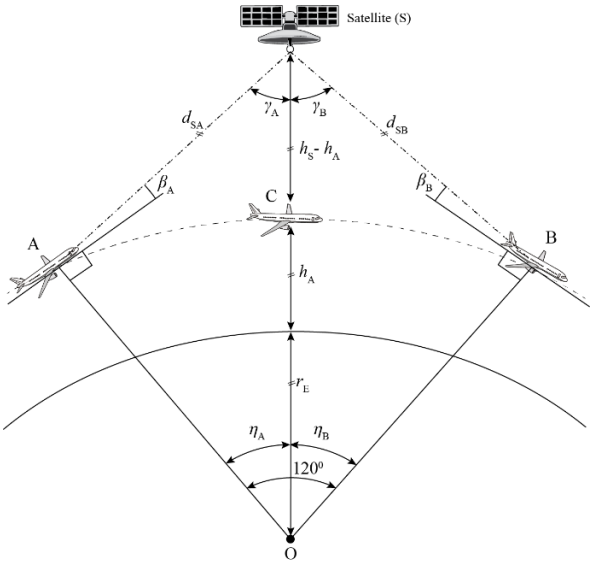

Fig. 2. An illustrative geometry of signal incidence on aircraft through satellite link.

In order to obtain incident angle of the striking wave on the aircraft, a geometrical model of Satellite-to-aircraft scenario is presented in the Fig. 2. Depending upon application's requirement, the number of satellites may vary; however, for simplicity, three satellites are assumed at latitudes separated by 120 degrees of a central angle to cover the whole geographical region of the earth. Consider a satellite S at the equator with an altitude h_S from the surface of the earth making angle γ_A and γ_B with aircrafts at position A and B respectively. Let h_A, r_E, d_{SA}, d_{SB} denotes the altitude of the flying aircrafts, the radius of the earth, propagation distance from satellite to aircraft at position A and B respectively. The incident waves make angles β_A and β_B with the axis of aircrafts A and B respectively. By using cosine rule, the lengths of propagation paths d_{SA} and d_{SB} can be calculated as follows:

$$d_{SA} = \sqrt{(h_S + r_E)^2 + (h_A + r_E)^2 - 2(h_S + r_E)(h_A + r_E)\cos\eta_A}, \quad (8)$$

$$d_{SB} = \sqrt{(h_S + r_E)^2 + (h_A + r_E)^2 - 2(h_S + r_E)(h_A + r_E)\cos\eta_B}, \quad (9)$$

by using sine rule, the angles γ_A and γ_B in reference to the equator can be obtained as:

$$\gamma_A = \sin^{-1}\left(\frac{(r_E + h_A)\sin\eta_A}{d_{SA}}\right), \quad (10)$$

$$\gamma_B = \sin^{-1}\left(\frac{(r_E + h_A)\sin\eta_B}{d_{SB}}\right), \quad (11)$$

by utilizing the geometry of the triangle SOA and SOB, the incident angles are obtained as follows:

$$\beta_A = \frac{\pi}{2} - \eta_A - \gamma_A, \quad (12)$$

$$\beta_B = \frac{\pi}{2} - \eta_B - \gamma_B. \quad (13)$$

Hence, by setting $h_A = 10$km, $h_S = 35796$km, $r_E = 6378.137$km, $\eta_A = 60^o$, $\eta_B = -60^o$, the incident angles of striking waves on aircrafts at position A and B are obtained as 21.921^o and 158.079^o respectively. It is worth noting that the incident angle of incoming waves will experience variable angle depending upon the location of the aircraft. The EM waves will strike perpendicularly to the surface of aircraft located on the equator and will form an incident angle $\beta_C = 90^o$ with aircraft's horizontal axis.

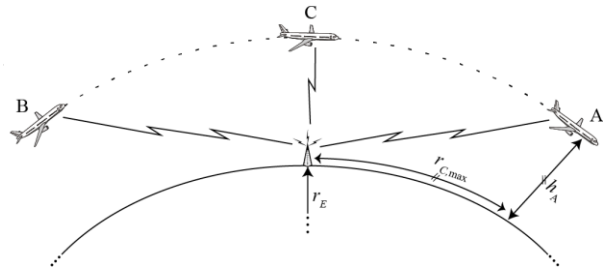

(a) LoS G2A communication geometry on earth sphere

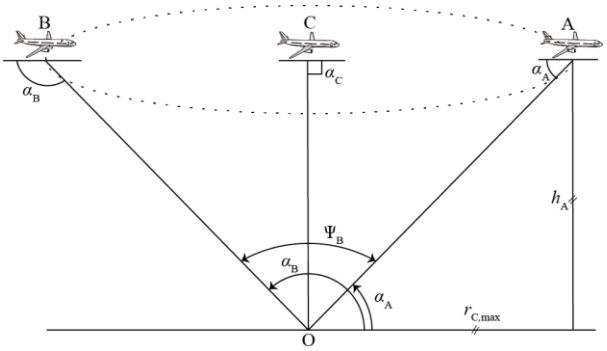

(b) A zoomed-in look of signal incidence on aircrafts

Fig. 3. An illustrative geometry of signal incidence on aircraft through ground link.

B. Ground-to-aircraft scenario

In order to observe scattering properties of a signal transmitted towards aircraft through ground wireless terminal/radar, a ground-to-aircraft scenario is assumed and presented in the Fig. 3. The Fig. 3 (a) explains the limitation of a LoS communication link due to spherical geometry of the Earth's surface. For clarity, a zoomed-in look of signal incidence and their corresponding angles with aircraft surface is illustrated in Fig. 3 (b). In this scenario, a wireless transmitter with three aircrafts having the same altitude (h_{A}) present at three different positions are considered. The coverage range of a transmitter is denoted with a dotted circular ring in which an aircraft is considered to be detectable or could receive communication signals from ground transmitter. The aircrafts at position A and B are located at extreme/edge of the coverage range of the radar or the ground transmitter while the aircraft at position C is assumed to be located at the middle of the coverage range which is exactly above the transmitter. The maximum spread of the beamwidth can be obtained by knowing the altitude of the aircraft and the maximum radius $r_{\mathrm{C,max}}$ of the coverage region. The angular spread of the beamwidth can be evaluated as follows [29]:

$$\Psi_{\mathrm{B}} = 2\tan^{-1}\left(\frac{r_{\mathrm{C,max}}}{h_{\mathrm{A}}}\right). \tag{14}$$

Where

$$r_{\mathrm{C,max}} = \cos^{-1}\left(\frac{r_{\mathrm{E}}}{r_{\mathrm{E}}+h_{\mathrm{A}}}\right). \tag{15}$$

The maximum angular span Ψ_{B} of beamwidth can then be evaluated as 176.8951^{o}, by substituting $r_{\mathrm{E}} = 6378.137^{\mathrm{o}}$ km and $h_{\mathrm{A}} = 10$ km in Eqs.(15) and (14). By utilizing the geometry presented in Fig. 3 (a), the incident angles α_{A} and α_{B} of EM waves impinging on aircraft A and B respectively are obtained as 1.5525^{o} and 178.45^{o}. Since, the aircraft A is located on the edge of the maximum coverage region; therefore, the angle α_{A} formed with the aircraft's surface is the minimum threshold angle below which the ground transmitter could not maintain a line of sight with the aircraft.

IV DESCRIPTION OF SIMULATION TOOL AND FACET-BASED MODEL OF AIRCRAFT A380

Physical Optics (PO) is one commonly used RCS prediction approach which provides best possible RCS results in the specular direction for electrically large complex bodies. It is a high-frequency simulation approach which is applicable in the situations when the wavelength of the incident wave is much smaller than the dimension of targeted body. In order to analyze scattering properties of incident EM waves on the surface of aircrafts, MATLAB-based Physical optics simulation tool POFACET® 4.2 is used. In this tool, the RCS of a complex object is usually approximated by utilizing a large number of triangular meshes (facets) that collectively represents the continuous surface of the complex object. The total RCS of the object is then evaluated by the superposition of the square root of the magnitude of each individual facet's RCS. For our modeling, we choose A380 [27] the world's largest commercial aircraft as an example. For the designing of aircraft A380, AutoCAD® model (.dwg file) of aircraft A380 is obtained [30,31] within an accuracy of 10cm. The AutoCAD® software provides an opportunity to create a blueprint of any design to view it realistically before the continuation of the design process. A detailed description of aircraft A380 dimensions are shown in Fig. 4. Since, the POFACET® [1] simulation tool requires a facet-based model to predict RCS, therefore, AnyCAD software is used to generate facet-based model of aircraft A380. The facet-based representations of aircraft A380 are demonstrated in Fig. 5. Fig. 5 (a) and Fig. 5 (b) show top and bottom look of facet-based aircraft A380, which is the main requirement of our proposed model, while Fig. 5 (c) presents a side view of the aircraft. The steps of the gradational procedure involved in the calculation of the scattering properties of the aircraft are listed in Table 1.

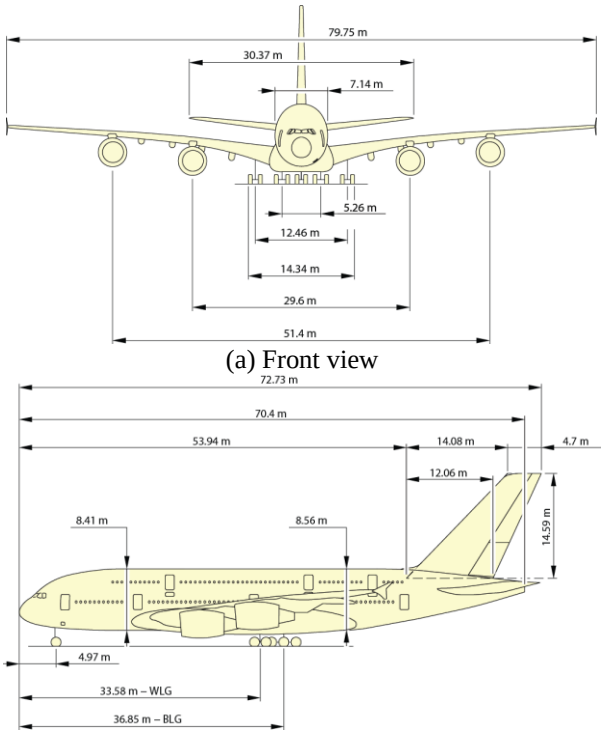

(a) Front view

(b) Side view.

Fig. 4. Aircraft A380 detailed dimensions [27].

Table 1: Gradational procedure for the calculation of bistatic RCS

Gradational Algorithmic Procedure:
1. Create an arbitrary aircraft model (aircraft.stl file format)
2. Run pofacet.m \\ GUI of POFACET® [1] will be shown
3. Select "Calculate Bistatic RCS" \\ Options: Design Model Manually, \\ Design Model Graphically, \\ Calculate Monostatic RCS, \\ Calculate Bistatic RCS, Utilities
4. Select "Angle" for the calculation of bistatic RCS \\ Options: Angle & Frequency
5. Load file (airplane.stl) \\ Set view point if needed
6. Adjust incident angles range \\ $(\theta_i, \emptyset_i)$
7. Set observation angles range \\ $0^o \leq \theta_r^o \leq 360^o, 0^o \leq \emptyset_r^o \leq 360^o$
8. Adjust computational parameters \\ Taylor series parameters, incident polarization \\ and frequency
9. Adjust surface roughness \\ If required
10. Press the button "Calculate RCS"
11. Select material type "R_s" \\ Options: Surface resistivity values (R_s) or Material data
12. Get the output

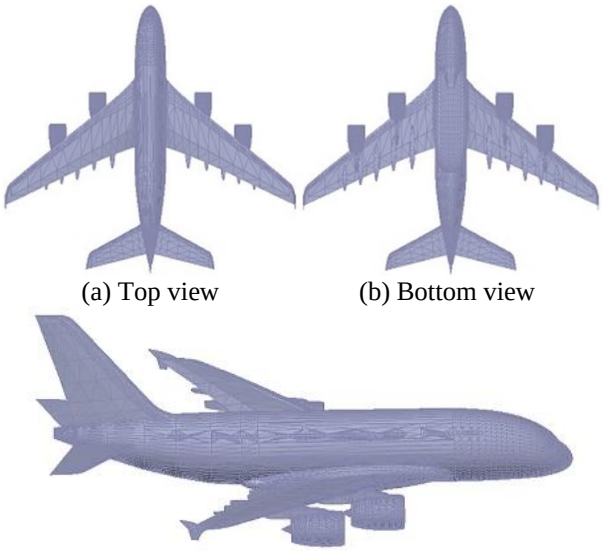

(a) Top view (b) Bottom view

(c) Side view

Fig. 5. Facet-based representation of aircraft A380.

V. SIMULATION RESULTS AND DISCUSSION

In this section, the RCS of aircraft A380 facet-based model is evaluated and analyzed for two scenarios: Satellite-to-aircraft and Ground-to-aircraft. For simulation process, three positions of aircrafts in both the scenarios are considered to compute bistatic RCS for specific incident angles as explained in Fig. 2 and Fig. 3 of Sec. III. The simulations of bistatic RCS are performed in spherical coordinate systems with incident angles (θ_i, ϕ_i) and observation angles (θ, ϕ). The incident angle is considered to be fixed because in bistatic RCS cases the radar/transmitter is located at fixed angle to the targeting aircraft while the observation angle may vary. Therefore, it is not necessary to calculate bistatic RCS for each incident angle. Although, the bistatic RCS can be observed in a wide range of observation angles equivalent to spherical geometry in the range $0 \leq \theta \leq \pi$ and $0 \leq \phi \leq 2\pi$; however, for simplicity only zero-azimuth plane (i.e., $\phi_i = 0, \phi = 0$) is considered to approximate bistatic RCS for the range of observation angle $0 \leq \theta \leq \pi$. The measured values can be represented easily in terms of bistatic angles by keeping the incident angles as a reference instead of an aircraft horizontal axis. In the scenario of Satellite-to-aircraft, only upper surface of the aircraft is considered for the evaluation of bistatic RCS, because a signal transmitted through satellite will encounter with only upper surface of the aircraft. The upper surface of the aircraft would be the main source of reflection and scattering of the signal towards the satellite or any other signal receiving entity. Similarly, in the scenario of ground-to-aircraft communication, the bottom surface of aircraft would be the main source of signal reflection/scattering at different observation angles towards the signal receiving units on the earth. In both the scenarios, the aircraft axis of motion (reflection plane) is considered as a reference for observation angles of bistatic RCS. The observation angles are measured in counter-clock wise rotation with reference to the reflection plane on the signal arrival side. For simulation, the number of Taylor series based polynomial is taken as 3, incident wave polarization mode is set at linear-vertical polarization, and the aircraft surface roughness is assumed as a smooth surface.

In satellite-to-aircraft communication link scenario, when both satellite and aircraft are present at the equator, the signal transmitted through satellite will make a 90 degrees angle with the aircraft upper body. In this case, the bistatic RCS fluctuations are obtained and plotted in Fig. 6 with respect to observation angle (θ). The results are measured in counter-clock direction by keeping the horizontal axis of aircraft motion as a reference axis.

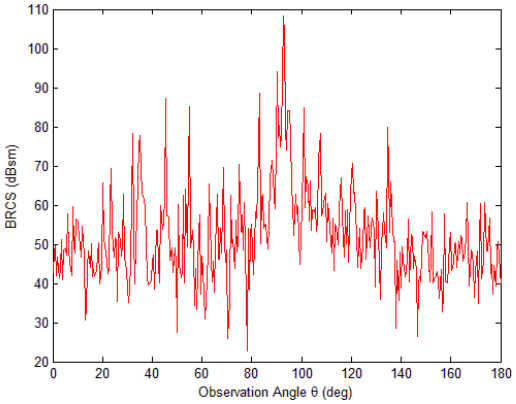

(a) Linear plot

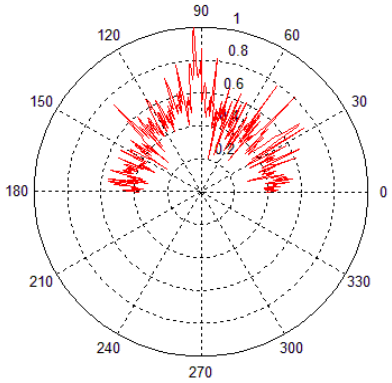

(b) Polar plot

Fig. 6. RCS observation of signal incidence at $\beta_c = 90^o$ in satellite-to-aircraft communication scenario.

The RCS values are observed only at upper half region ($0 \leq \theta \leq 180$) of the observation angels because in this region the reflections would be prominent with high power gain. In the figure, a high peak is envisioned at angle 92.5^o which is basically a specular reflection from the aircraft surface. Hence, at observation angles on which the BRCS is high, the reflecting surface of the aircraft will possibly provide strong interference to satellites or aircrafts located at these observation angles.

In Fig. 7, the angular bistatic scattering response of aircraft at incident angle $\beta_a = 21.921^o$ is shown with both linear and normalized poler plots in Fig.7 (a) and Fig. 7 (b) respectively. The impact of signal incidence at angle β_a shows that the aircraft upper body scatters signal power in all directions with different power amplitudes. The specular reflection of aircraft is obtained at angle 158.079^o with a power gain of 104.7 dBsm. Figure 8 presents scattering behavior of the aircraft surface for an incident angle of 158.079^o with both inear and normalized polar graphs in Fig. 8 (a) and Fig. 8 (b) respectively.

The results show that at this particular incident angle the aircraft metallic surface and its curved structure scatters signal power in all directions with different amplitude levels according to the observed angles θ. Specular reflection of the signal is observed at an angle of 22^o with a power gain of 98.29 dBsm. From the simulation results, it can be concluded that in Satellite-to-aircraft communication links the aircraft metallic surface and its curved shape may provide interference to its surrounding receivers (satellite/aircrafts) due to signal reflections from its surface. In this situation, the performance of the surrounding receivers may get degraded based upon the interfering signal power level received at the receiver end. Hence, these simulation results provide a way to observe interfering signal reflections from flying aircrafts during the communication between satellites and aircrafts.

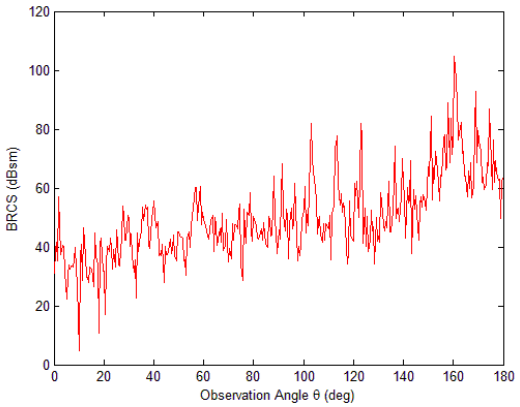

(a) Linear plot

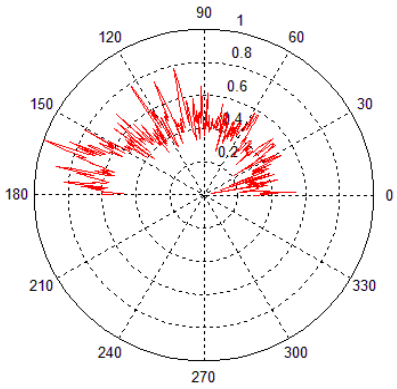

(b) Polar plot

Fig. 7. RCS observation of signal incidence at $\beta_a = 21.921^o$ in satellite-to-aircraft communication scenario.

In Fig. 9, bistatic RCS of an aircraft by impinging a signal at incident angle $\alpha_C = 90^o$ to its lower body is evaluated and shown in both linear and polar plots. In the scenario of ground-to-aircraft, angular bistatic RCS observation are calculated by considering only the lower surface of aircraft. This is due to the fact that in this case the lower body of the aircraft would be the main source of signal reflection with high amplitude of scattering power as compared to the aircraft's upper surface.

Moreover, it is quite realistic to assume that in this scenario, the transmitted signals will not strike on the upper surface of the aircraft. By keeping the aircraft's axis of motion as a reference, angular bistatic RCS values are evaluated with respect to observation angles of range 0^o to 180^o in $\phi = 0$ plane, which is the lower half region of the aircraft in which the signal will scatter and carry the high scattering power. The observation angles are measured in the counter clock direction by keeping the aircraft's axis of motion as a reference axis, as shown in Fig. 9 (b). From the figure, it is worth notable that the lower part of the complex structure of aircraft constitutes good reflecting properties and generates signal reflection at every observation angle which are considered in this simulation. In the figure, the highest peak of bistatic RCS is observed at 131.5^o with 90.29 dBsm amplitude, however, the specularly reflected RCS amplitude value is obtained as 87.72 dBsm at angle 87.5^o. The high peaks other than the specularly reflected power occur due to the complex curved structure of the aircraft's metallic body which reflects/scatters incident wave towards these particular observation angles and as a result gives rise to bistatic RCS.

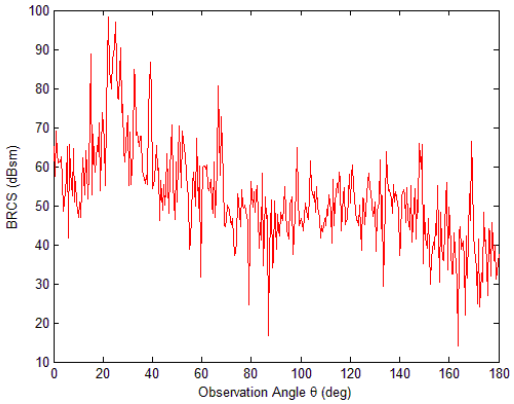

(a) Linear plot

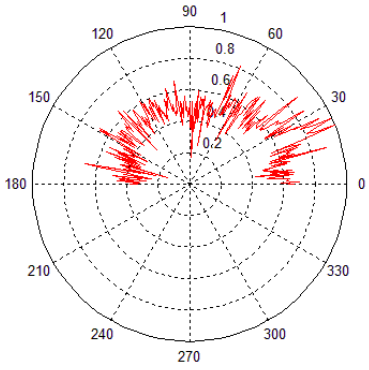

(b) Polar plot

Fig. 8. RCS observation of signal incidence at $\beta_B = 158.079^o$ in satellite-to-aircraft communication scenario.

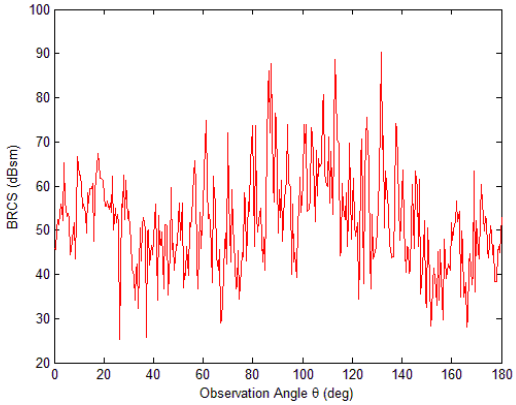

(a) Linear plot

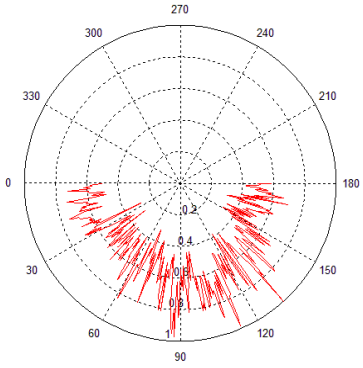

(b) Polar plot

Fig. 9. RCS observation of signal incidence at $\alpha_C = 90^o$ in ground-to-aircraft communication scenario.

In Fig. 10, bistatic RCS of aircraft at incident angle $\alpha_A = 1.5525^o$ is presented with both linear and polar graphs in Fig. 10 (a) and Fig. 10 (b) respectively. The bistatic RCS shows specularly reflected behavior at an angle 179.5^o with amplitude 87.21 dBsm. In Fig. 11, bistatic RCS of the impinging wave having incident angle $\alpha_B = 178.45^o$ with respect to observation angles θ is presented. The maximum value of bistatic RCS is observed at angle 2^o with amplitude 81.59 dBsm. Bistatic RCS observations of these incident angles give a way to envision the interfering reflected power from the aircraft's surface which degrades the performance of neighboring receivers whether aircrafts or ground terminals. By keeping the knowledge of interfering signal power, counter-measures can be made for better performance and error avoidance.

Figure 12 presents the behavior of spatial reflection coefficient as a function of RCS, line-of-sight (LOS) distance (d_1) and reflected signal distance (d_2). For simulation, bistatic RCS results obtained in satellite-to-aircraft scenario with 90^o signal incidence are only used. Whereas, the LOS distance (d_1) and reflected signal distance (d_2) are taken as 35786 km and 10 km

respectively. The result explains that how much power is reflected from the surface of the aircraft and as a result providing interfering signal reflection to its neighboring receivers. At 90^{o} signal incidence from the satellite, the aircraft surface will provide a strong reflection to aircrafts/satellites which are present at 90^{o} observation angle, however, it will provide quite ignorable interference at rest of the observation angle. Varying the distances of LOS (d_1) and reflected signal paths (d_2), the behavior of spatial reflection coefficient can be envisioned in Fig. 13.

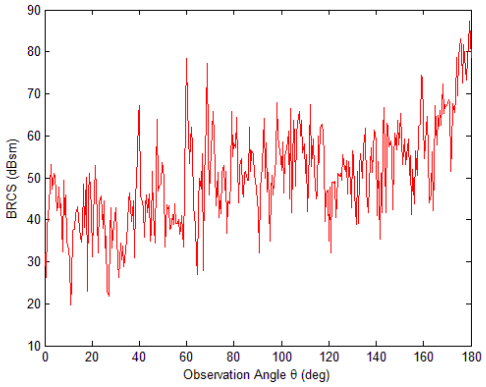

(a) Linear plot

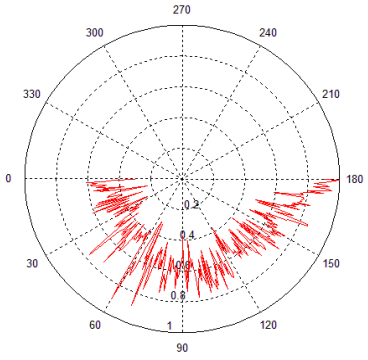

(b) Polar plot

Fig. 10. RCS observation of signal incidence at $\alpha_{\mathrm{A}} = 1.5525^{o}$ in ground-to-aircraft communication scenario.

From the figure, it is observable that the amplitude of SRC decreases as the distance increases and increases when the distances decrease. The results show a way to observe the scattering mechanism of a signal from flying aircrafts and strength of reflected interfering signal. A comparison between SRC and RCS is shown in the Fig. 14. Comparison between SRC and RCS shows that both the terms follows the same trend with a constant scaling factor based upon the propagation distances. From the analysis, it is observed that SRC and RCS follow the same scattering behavior and can be used interchangeably to analyze a communication system model. In wireless communication systems, multipath environment is a propagation phenomenon which occurs due to reflection, diffraction, refraction or scattering of a signal through objects (scatters) present between the transmitter and receiver. In such environments, the receiver receives multiple versions of phase shifted and attenuated signals, which when combined results a faded signal of much less power. Thus, the RCS can be used interchangeably instead of reflection coefficient to validate and analyze any communication system model. From the design and simulation point of view, as POFACET [1] simulation tool works by utilizing a facet-based representation of a model, therefore, inaccurate facet-based modeling of a model may induce facetization error which may lead to inaccurate observation of the RCS. The facetization error usually occurs when a smooth continuous surface is represented by discrete facets having inappropriate size (i.e., large facets) as compared to the smoothness of the surface. Hence, to decrease the facetization error, an appropriate mesh size must be used to generate a tight fitting mesh representation of the model. On one hand, accurate calculations of bistatic RCS require a smooth facet-based model with small facet size, while on the other hand, this leads to high computations which is not always possible to perform on normal computers. Therefore, a machine having a high-processing capability may get more accurate RCS results with less facetization error.

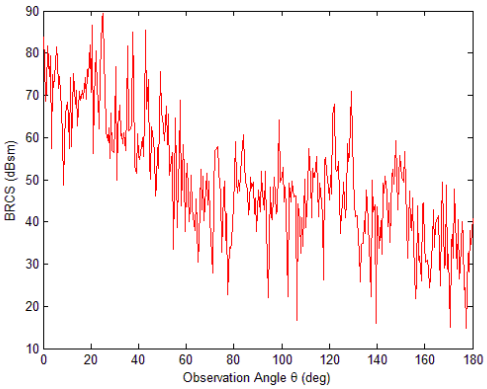

(a) Linear plot

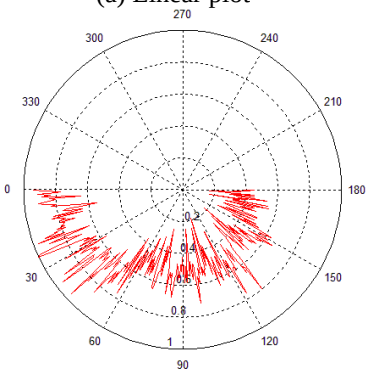

(b) Polar plot

Fig. 11. RCS observation of signal incidence at $\alpha_{\mathrm{B}} = 178.45^{o}$ in ground-to-aircraft communication scenario.

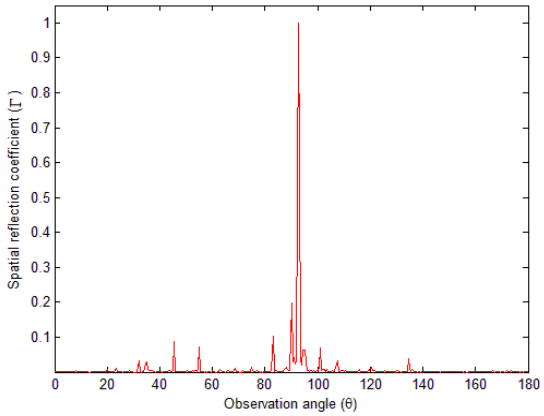

Fig. 12. Plot of spatial reflection coefficient as a function of bistatic RCS formulated with 90º signal incidence in satellite-to-aircraft scenario.

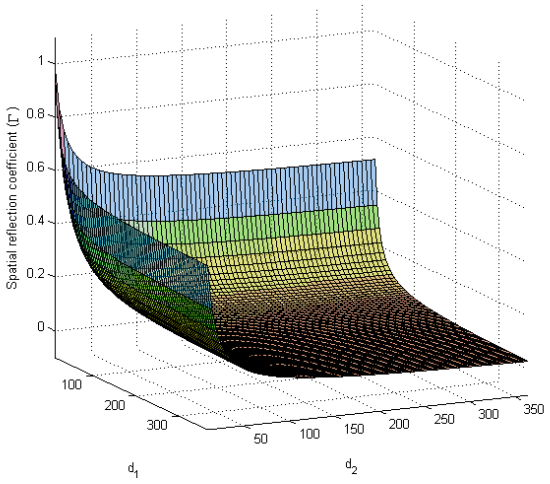

Fig. 13. Reflection coefficient as a function of RCS, d_1 and d_2.

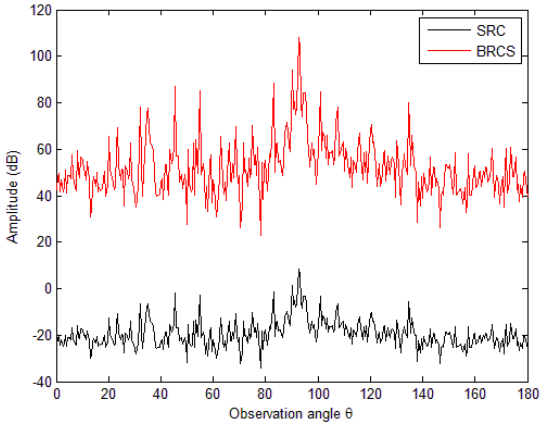

Fig. 14. Comparison between SRC and BRCS.

VI. CONCLUSION

Correct evaluation of the RADAR Cross Section (RCS) and its prediction is imperative in designing of high performance radars as well as for aircrafts having low visibility towards the radar. In this article, interdependence of the RCS and Spatial Reflection Coefficient (SRC) has been highlighted to formulate a compact relationship between the two terms. Scattering mechanism of aircraft surface has been analyzed by developing geometrical models of two scenarios, i.e., satellite-to-aircraft and ground-to-aircraft. The proposed geometrical models were developed to obtain incident angles of impinging EM waves on the surface of the aircraft. In order to observe the bistatic RCS of aircraft, POFACET® [1] simulation tool has been incorporated with a facet-based model of aircraft A380. From the simulations, it was observed that complex structure of aircraft model constitutes good reflecting properties which in turn may provide interfering signals to its neighboring aircrafts which may degrades their communication performance. From the results, it was concluded that accurate geometrical modeling of aircraft communication environment may help to understand the nature of interfering signals and to increase the communication performance in satellite-to-aircraft and ground-to-aircraft communication systems. Analysis shows that SRC and RCS can be used interchangeably which may help to analyze and validate the communication system models for better performance. The conceptual relationship between SRC and RCS is analyzed on the basis of the data taken from simulations. Since no measurements are incorporated; hence, the conclusive observations are just indicative but not definitive. In future, a more generalized aircraft scattering geometrical model should be established to observe the scattering behavior of signals from aircraft surface in 3D space.

REFERENCES

[1] F. Chatzigeorgiadis and D. C. Jenn, "A matlab physical-optics rcs prediction code," *IEEE Antennas and Propagation Magazine*, vol. 46, no. 4, pp. 137-139, 2004.

[2] X. Fan, Y. Qin, S. Shang, D. Song, W. Sun, D. Li, and X. Luo, "Research on the bastatic rcs characteristics of stealth aircraft," *Asia-Pacific Microwave Conference (APMC)*, vol. 3, pp. 1-3, Dec. 2015.

[3] L. Zhu, X. Liang, J. Li, and R. Li, "Simulation analysis on static scattering characteristics of stealth aircraft," *IEEE Advanced Information Management, Communicates, Electronic and Automatic Control Conference (IMCEC)*, pp. 1774-1778, Oct. 2016.

[4] J. M. Jin, *Theory and Computation of Electro-magnetic Fields*. John Wile & Sons, 2011.

[5] E. Mach, *The Principles of Physical Optics: An Historical and Philosophical Treatment*. Dover, NY, USA, 1953.
[6] D. Jenn and C. Ton, "Wind turbine radar cross section," *International Journal of Antennas and Propagation*, vol. 2012, p. 14, 2012.
[7] A. Ishimaru, *Electromagnetic Wave Propagation, Radiation and Scattering*. Englewood Cliffs, New Jersey, Prentice Hall, 1991.
[8] J. Song, C.-C. Lu, and W.C. Chew, "Multilevel fast multipole algorithm for electromagnetic scattering by large complex objects," *IEEE Transaction on Antennas and Propagation*, vol. 45, no. 10, pp. 1488-1493, Oct. 1997.
[9] G. Cakir, M. Cakir and L. Sevgi, "Radar cross section (rcs) modeling and simulation, part 2: A novel fdtd-based rcs prediction virtual tool for the resonance regime," *IEEE Antennas and Propagation Magazine*, vol. 50, no. 2, pp. 81-94, Apr. 2008.
[10] G. Cakir, M. Cakir, and L. Sevgi, "An FDTD-based parallel virtual too for rcs calculations of complex targets," *IEEE Antennas and Propagation Magazine*, vol. 56, no. 5, pp. 74-90, Oct. 2014.
[11] L. Sevgi, "Target reflectivity and rcs interactions in integrated maritime surveillance systems based on surface-wave high-frequency radars," *IEEE Antennas and Propagation Magazine*, vol. 43, no. 1, pp. 36-51, Feb. 2001.
[12] J. D. Wilson, "Probability of detecting aircraft targets," *IEEE Transactions on Aerospace and Electronic Systems*, no. 6, pp. 757-761, 1972.
[13] A. David, C. Brousseau, and A. Bourdillon, "Simulations and measurements of a radar cross section of a Boeing 747-200 in the 20-60 mhz frequency band," *Radio Science*, vol. 38, no. 4, pp. 3-1-3-4, 2003.
[14] B. Persson and M. Norsell, "On modeling rcs of aircraft for flight simulation," *IEEE Antennas and Propagation Magazine*, vol. 56, no. 4, pp. 34-43, 2014.
[15] Z. W. Liu, D. Z. Ding, Z. F. Fan, and R. S. Chen, "Adaptive sampling bicubic spline interpolation method for fast calculation of monostatic rcs," *Microwave and Optical Technology Letters*, vol. 50, no. 7, pp. 1851-1857, 2008. [Online]. Available: http://dx.doi.org/10.1002/mop.23540
[16] Z. W. Liu, R. S. Chen, and J. Q. Chen, "Adaptive sampling cubic-spline interpolation method for efficient calculation of monostatic rcs," *Microwave and Optical Technology Letters*, vol. 50, no. 3, pp. 751-755, 2008.
[17] W.-D. Li, J.-X. Miao, J. Hu, Z. Song, and H.-X. Zhou, "An improved cubic polynomial method for interpolating/extrapolating mom matrices over a frequency band," *Progress in Electromagnetics Research*, vol. 117, pp. 267-281, 2011.
[18] W.-D. Li, H.-X. Zhou, J. Hu, Z. Song, and W. Hong, "Accuracy improvement of cubic polynomial inter/extrapolation of mom matrices by optimizing frequency samples," *IEEE Antennas and Wireless Propagation Letters*, vol. 10, pp. 888-891, 2011.
[19] Y. An, D. Wang, and R. Chen, "Improved multilevel physical optics algorithm for fast computation of monostatic radar cross section," *IET Microwaves, Antennas & Propagation*, vol. 8, no. 2, pp. 93-98, 2014.
[20] T. S. Rappaport, *Wireless Communications: Principles and Practice*. Prentice Hall PTR New Jersey, vol. 2, 1996.
[21] R. Geise, A. Enders, H. Vahle, and H. Spieker, "Scaled measurements of instrument-landing-system disturbances due to large taxiing aircraft," *IEEE Transactions on Electromagnetic Compatibility*, vol. 50, no. 3, pp. 485-490, 2008.
[22] E. F. Knott, *Radar Cross Section Measurements*. Springer US, 1993.
[23] M. Cherniakov, *Bistatic Radar: Principles and Practice*. John Wiley & Sons Ltd, 2007.
[24] O. Landron, M. J. Feuerstein, and T. S. Rappaport, "In situ microwave reflection coefficient measurements for smooth and rough exterior wall surfaces," *43rd IEEE Vehicular Technology Conference*, pp. 77-80, 1993.
[25] O. Landron, M. J. Feuerstein, and T.S. Rappaport, "A comparison of theoretical and empirical reflection coefficients for typical exterior wall surfaces in a mobile radio environment," *IEEE Transactions on Antennas and Propagation*, vol. 44, no. 3, pp. 341-351, 1996.
[26] S. R. Bullock, *Transceiver and System Design for Digital Communications*. SciTech Publishing Inc., 2009.
[27] J. Liu, *Spacecraft TT&C and Information Transmission Theory and Technologies*. Springer-Verlag Berlin Heidelberg, 2015.
[28] B. Mahafza, *Introduction to Radar Analysis*, ser. Advances in Applied Mathematics Series. Taylor & Francis, 1998. [Online]. Available: https://books.google.com.pk/books?id=HnbERpllrX0C
[29] S. J. Nawaz, N. M. Khan, M. I. Tiwana, N. Hassan, and S. I. Shah, "Airborne internet access through submarine optical fiber cables," *IEEE Transactions on Aerospace and Electronic Systems*, vol. 51, no. 1, pp. 167-177, 2015.
[30] Airbus S.A.S, "Aircraft characteristics airport and maintenance planning," 01 Dec 2016. [Online]. Available: http://www.airbus.com/support-services/support/technical-data/aircraft-characteristics/
[31] Airbus S.A.S, "Autocad 3-view aircraft drawings," 10 May 2012. [Online]. Available: http://www.airbus.com/support-services/support/technical-

data/autocad-3view-aircraft-drawings/

Muhammad-Yasir Masood Mirza received his M.Sc. Mathematics degree from International Islamic University, Islamabad, Pakistan in 2006 and the M.S. Electronics Engineering degree with specialization in Communication Systems from Mohammad Ali Jinnah University, Islamabad, Pakistan in 2011. At present, he is pursuing his Doctoral Degree from Capital University of Science and Technology (CUST), Islamabad, Pakistan. His research interests include channel modeling and characterization, channel estimation, smart antenna systems, localization and ground-to-air communication systems.

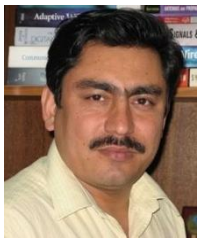

Noor M. Khan received his B.Sc. degree in Electrical Engineering from the University of Engineering and Technology (UET), Lahore, Pakistan, in 1998 and Ph.D. degree in Electrical Engineering from the University of New South Wales (UNSW), Sydney, Australia in 2006. He held several positions in WorldCall, NISTE, PTCL, UNSW, GIK Institute of Engineering Sciences and Technology, and Mohammad Ali Jinnah University, Pakistan from 1998 to 2015. Currently, he is working as Professor with the Capital University of Science & Technology (CUST), Islamabad, Pakistan. He has served as Chair and Co-Chair of the Technical Program Committees of IEEE International Conference on Emerging Technologies (ICET2012) in 2012 and IEEE International Multi-topic Conference (INMIC-2009) in 2009, respectively. He has been awarded Research Productivity Award (RPA) by the Pakistan Council for Science and Technology (PCST) for the years 2011 and 2012. His research interests include channel modeling and characterization, wireless sensor networks, cellular mobile communication networks and ground-to-air communication systems.

Abid Jamal was born in Pakistan in 1991. He received the B.Sc. degree in Electronic Engineering from the University of Lahore, Islamabad, Pakistan and M.S. in Electrical Engineering from Capital University of Science and Technology, Islamabad, Pakistan in 2016. His research interests include Radar cross section measurements, smart grid communication, cellular and mobile communication systems.

Rodica Ramer received a B.Sc. degree in Engineering Physics, M.E. in Electrical Engineering and Ph.D. in the Solid State Physics in 1989, all from the University of Bucharest. Ramer joined the University of New South Wales (UNSW), in 1993, where she is a Professor in the School of Electrical Engineering and Telecommunications, leading the micro-wave, millimeter-wave and electromagnetics group. She has held guest and visiting professorship positions at many Universities around the world. Her research activities have been in the area of microwave devices and materials and EM techniques. She has authored and co-authored over 250 refereed papers and a number of book/chapters and patents. Her current research involves advancements in RF MEMS and SIW technologies. Ramer is a Senior Member of IEEE MTT-S, AP-S and Com.Soc., and a Fellow of Electromagnetics Academy. She has held key positions and has served on various panels and international committees and international conferences/symposia. She has served on editorial/review boards of several journals and conferences.

Synthetic Asymptote Formulas of Square Coaxial Line

Jinqun Ge [1], Jianping Zhu [3], Zhengyong Yu [1], Haiyong Zhang [1], and Wanchun Tang [1,2]

[1] Jiangsu Key Laboratory on Optoelectronic Technology, Nanjing Normal University, Nanjing, 210023, China
932682934@qq.com, yonglly@sina.com, 872299562@qq.com, eewctang@njnu.edu.cn

[2] Jiangsu Center for Collaborative Innovation in Geographical Information Resource Development and Application
Nanjing, 210023, China

[3] School of Electronic and Optical Engineering, Nanjing University of Science and Technology
Nanjing, 210023, China
169148076@qq.com

Abstract ─ This paper derives simple computer-aided design (CAD) formulas of characteristic impedance and open-ended capacitance of square coaxial line by synthetic asymptote and moment method. These formulas can be used for the design of the 3-D frequency selective surface (FSS) with square coaxial line as unit cells. Both of the formulas can give good physical insights and have only one or two arbitrary constants to be matched with numerical results. A good agreement was found between the results by the formulas and numerical method.

Index Terms ─ CAD formulas, frequency selective surface (FSS), square coaxial line, synthetic asymptote.

I. INTRODUCTION

Frequency-selective surfaces (FSSs) have been studied over the past decades. A conventional FSS consists of two-dimensional (2-D) periodic unit cells, which are either printed on a dielectric layer or etched out of a conductive surface [1-2]. Recently, thanks to the significant improvements in computational electromagnetic methods and fabrication technology, three-dimensional (3-D) FSSs [3-5] have been proposed and studied.

Compared with 2-D FSSs, 3-D FSSs have one more design freedom and therefore more paths for electromagnetic wave propagating. The propagation paths may produce multiple transmission zeros and poles under proper design. For the 3-D FSS unit cell design, waveguide is good choice and studied in many references. In [3], 3-D FSS based on substrate integrated waveguide (SIW) structures is proposed and produce transmission zeros through the couplings between different resonant modes in these SIW cavities. In [4], Shen etc. proposed a 3-D FSS with the unit cell consists of vertical and horizontal double-sided parallel-strip lines and a thin metallic plate, which formed substrate and air paths to produce transmission poles and zeros. This unit cell in [4] can also be considered as a rectangular waveguide loaded with a planar circuit.

Another kind of waveguide, coaxial line, can also be used as the unit cell of 3-D FSS. To produce the propagation paths easily, square coaxial line is chosen as the unit cell of 3-D FSS [6] by the authors. Square coaxial line not only has one "coaxial path", but also introduces a "parallel plate path" between the adjacent unit cells to ease the analysis and design. And these two paths can provide multiple transmission poles and zeros under proper design.

In the FSS analysis and design, equivalent circuit model is a very useful tool and should be established. For the square coaxial line 3-D FSS, the equivalent circuit model has two important parameters, in particular, the characteristic impedance and the open-ended capacitance of the square coaxial line.

There are several references for calculating the characteristic impedance [7-9] and the open-ended capacitance [10-11] of square coaxial line, generally in analytical or numerical approach. All the closed form expressions in [7-11] have more than two constants to be curve-fitted. Synthetic asymptote technique is useful in deriving simple CAD formulas and such synthetic asymptote formulas have been obtained by the authors in a series papers [12-14]. Generally, synthetic asymptote is the sum of two regular asymptotes at the two limits of one parameter, with one or two arbitrary constants to be matched with numerical results. And the synthetic asymptote formula has good physical insights, and is useful in practical initial design.

In this paper, the formulas of the characteristic impedance and the open-ended capacitance of the square coaxial line are derived by synthetic asymptote. Unlike reference [6] by the authors, more detailed derivation will be given in this paper. Compared with numerical

Submitted On: April 21, 2017
Accepted On: October 24, 2017

results by moment method [15] under quasi-static condition and full-wave EM commercial software HFSS [16], the average error of the formulas is less than 2% with the maximum error of 6.5%.

II. DERIVATION OF THE FORMULA OF CHARACTERISTIC IMPEDANCE

For the derivation of the formula of characteristic impedance, only TEM mode is considered in this paper. In the cross section view of the square coaxial line shown in Fig. 1, c is the side length of the inner conductor and a-b is the thickness of the outer conductor. The dielectric with dielectric constant ε_r is filled in between the inner and outer conductors. From the transmission line theory, the characteristic impedance Z_0 of the square coaxial line is:

$$Z_0 = \frac{1}{v_0\sqrt{C_0 C_{total}}}, \tag{1}$$

where v_0 is the light speed in free space. C_0 and C_{total} are the capacitances per unit length of the square coaxial line when the dielectric between the inner and outer conductors is free space and dielectric, respectively, and they can be derived by synthetic asymptote which is constructed by two regular asymptotes (near and far asymptotes) of one parameter. In this paper, this parameter is chosen as $S=b/c$.

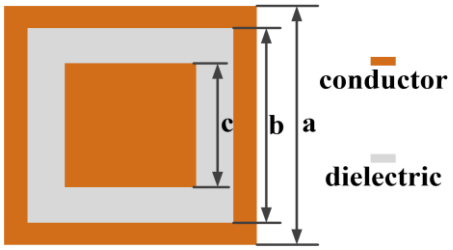

Fig. 1. Cross section of square coaxial line.

A. Near asymptote ($S\to 1$)

When $S\to 1$, the dielectric between the inner and outer conductors is very thin. This means that the near asymptote of the capacitance is that of the parallel plate with 4 sides of the inner conductor. Hence, we have:

$$C_{near} \overset{Asym}{=\!=}_{S\to 1} C = 4\varepsilon_0\varepsilon_r \frac{c}{\frac{b-c}{2}} = 4\varepsilon_0\varepsilon_r \frac{2}{S-1}. \tag{2}$$

B. Far asymptote ($S\to\infty$)

When $S\to\infty$, the inner conductor is very far from the outer conductor and then the square coaxial line can be considered as a circular coaxial line. Therefore, the far asymptote is:

$$C_{far} \overset{Asym}{=\!=}_{S\to\infty} C = \frac{2\pi\varepsilon_0\varepsilon_r}{\ln(\frac{b}{c})} = \frac{2\pi\varepsilon_0\varepsilon_r}{\ln(S)}. \tag{3}$$

Usually, synthetic asymptote is constructed by summing the regular asymptotes at the two limits of the parameter under the "asymptote consistency condition". The condition is that the far asymptote will approach zero or a pretty small number at the near parameter limit and vice versa for the near asymptote. From Eq. (3), one can see that when $S\to 1$, the far asymptote tends to infinity and will have effects on the near asymptote. Therefore, like the far asymptote formula in [12], Eq. (3) can be modified as following:

$$C_{far} \overset{Asym}{=\!=}_{S\to\infty} C \approx \frac{2\pi\varepsilon_0\varepsilon_r}{\ln(S)} - \frac{2\pi\varepsilon_0\varepsilon_r}{S-1}. \tag{4}$$

C. Synthetic asymptote

By adding the Eqs. (2) and (4) together, we obtain the synthetic asymptote:

$$C_{total} = \left\{ \begin{array}{l} (4\varepsilon_0\varepsilon_r \frac{2}{S-1})^m \\ +\left[\frac{2\pi\varepsilon_0\varepsilon_r}{\ln(S)} - \frac{2\pi\varepsilon_0\varepsilon_r}{S-1}\right]^m \end{array} \right\}^{\frac{1}{m}}, \tag{5}$$

with the power of m. Matching with one data point with numerical computation at an arbitrary C_{total}, the power m is obtained as 1.08, the same as that of synthetic asymptote formula for microstrip in [12], which can make the average error of Eq. (5) less than 2%.

III. DERIVATION OF THE FORMULA OF OPEN-ENDED CAPACITANCE

To obtain the formula of the open-ended capacitance $C_{open\text{-}end}$ for the open-end of square coaxial line, Fig. 2 (a) gives the distribution of the fringe field at the open-end of square coaxial line. One can see that $C_{open\text{-}end}$ is half of the capacitance C_a of the metal plate and metal loop, a two conductors system in free space, as shown in Fig. 2 (b). We may use the synthetic asymptote and analytical moment method to derive the formula of C_a.

One should note that in this two conductors system, the voltages on metal plate and metal loop are different since they form a two-conductor transmission line. Assuming the voltage and charge on the metal plate of Fig. 2 (b) are V_1 and Q_1, while V_2 and Q_2 on metal loop, we then have:

$$V_1 = P_{11}Q_1 + P_{12}Q_2, \tag{6}$$

$$V_2 = P_{21}Q_1 + P_{22}Q_2, \tag{7}$$

with $P_{12}=P_{21}$, the mutual-potentials between the metal plate and the metal loop. P_{11} and P_{22} are, respectively, the self-potentials on metal plate and loop.

By setting V_1=1V and V_2=0V in Eqs. (6) and (7), the

capacitance of the metal plate and loop C_a is then:

$$C_a = \frac{Q_1}{V_2} = \frac{P_{22}}{P_{11}P_{22} - P_{12}^{\ 2}}. \tag{8}$$

And the open-ended capacitance ($C_{open\text{-}end}$) of square coaxial line in Fig. 2 (a) is:

$$C_{open-end} = \frac{1}{2}C_a = \frac{1}{2}\frac{P_{22}}{P_{11}P_{22} - P_{12}^{\ 2}}. \tag{9}$$

To obtain the capacitance C_a, one can see that the self and mutual-potential in the above Eq. (8) should be obtained firstly.

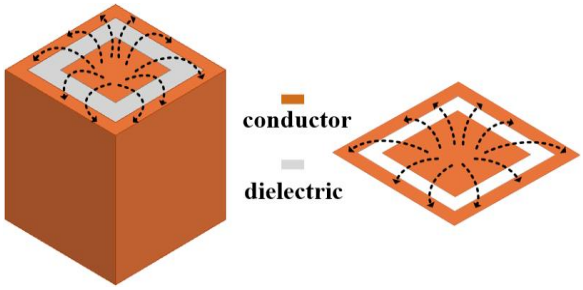

(a) (b)

Fig. 2. Schematic diagram of electric field distribution. (a) The open end of square coaxial line. (b) Metal plate and loop in free space.

A. Self-potentials P_{11} and P_{22}

The self-potential P_{11} of the metal plate as depicted in Fig. 3 (a) can be calculated by the "root of area" formula in [13], that is:

$$P_{11} = \frac{1}{C_{11}} = \frac{1}{c_{f1}\varepsilon_0\sqrt{8\pi c^2}}, \tag{10}$$

with the "shape factor" c_{f1}= 0.9.

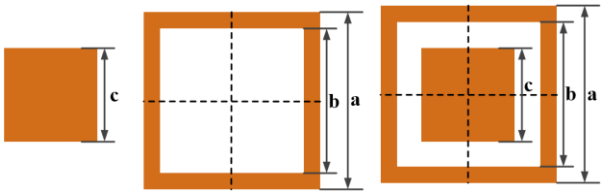

(a) (b) (c)

Fig. 3. Three kinds of structures: (a) metal plate, (b) metal loop, and (c) metal plate and metal loop, for the self and mutual potentials calculation in free space.

For the self-potential P_{22}, the metal loop can be divided into 4 segments, as shown in Fig. 3 (b). Using the analytical moment method and synthetic asymptote formulas in [13], P_{22} can be expressed as:

$$P_{22} = \frac{1}{c_{f1}\varepsilon_0\sqrt{8\pi a^2}} + \frac{1}{4}\frac{1}{c_{f2}\varepsilon_0\sqrt{8\pi}}\left(\frac{1}{\sqrt{\frac{a^2-b^2}{4}}} - \frac{1}{\sqrt{\frac{a^2}{4}}}\right), \tag{11}$$

where the $c_{f2} = \frac{3.5a}{b}$ is the "shape factor" of the metal loop obtained by matching with numerical results.

B. Mutual-potential P_{12}

For the mutual potential P_{12}, we may first obtain the capacitance C_b of the metal plate and metal loop in Fig. 3 (c) with the *same* potential on them, in other words, V_2=V_1=1V for example. In this case, the metal plate and loop can be considered as a large solid metal plate with a square slot etched on it. Therefore, the capacitance C_b has the same form as that of Eq. (11), i.e.,

$$\frac{1}{C_b} = \frac{1}{c_{f1}\varepsilon_0\sqrt{8\pi a^2}} + \frac{1}{4}\frac{1}{c_{f3}\varepsilon_0\sqrt{8\pi}}\left(\frac{1}{\sqrt{\frac{a^2}{4} - \frac{b^2-c^2}{4}}} - \frac{1}{\sqrt{\frac{a^2}{4}}}\right), \tag{12}$$

with $c_{f3} = \frac{3.5a}{\sqrt{b^2-c^2}}$ by substituting $\sqrt{b^2-c^2}$ for b of c_{f2}.

On the other hand, by setting V_2= V_1=1V in Eqs. (6) and (7), C_b can be expressed as:

$$C_b = \frac{Q_1 + Q_2}{V_1} = \frac{P_{11} + P_{22} - 2P_{12}}{P_{11}P_{22} - P_{12}^{\ 2}}. \tag{13}$$

After some manipulations, the mutual-potential P_{12} can be derived from Eq. (13):

$$P_{12} = \frac{1}{C_b} \pm \sqrt{\frac{1}{C_b^{\ 2}} - \frac{P_{11}+P_{22}}{C_b} + P_{11}P_{22}}. \tag{14}$$

In Eq. (14), the mutual-potential P_{12} has two possible results due to the sign of "±". However, the mutual-potential should be less than the self-potential from the physical insight. Figure 4 shows the P_{12} with sign of "+"and "-" for different c/b of the square coaxial line, where a=10mm and b=9mm. As can be seen, negative sign "-" in Eq. (14) is suitable for the calculation of P_{12}. Many computations have been done for other different values of the structure parameters a, b, and c, and we find that "-" in Eq. (14) should be taken for P_{12} calculation.

Substituting the potentials P_{11}, P_{22}, and P_{12} by Eqs. (10), (11), and (14) with negative sign of "-", respectively, into Eq. (9), the open-ended capacitance of

the square coaxial line can be obtained.

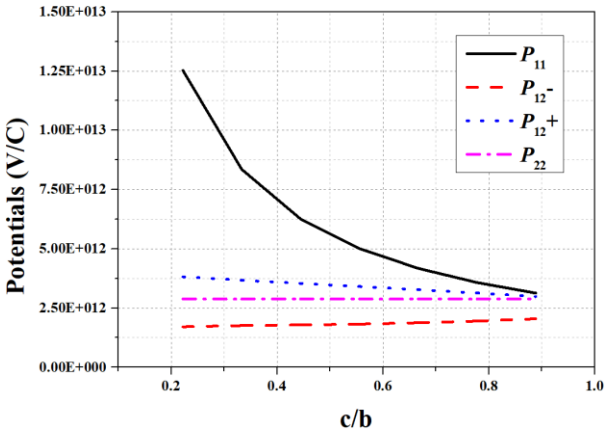

Fig. 4. The P_{12} with sign of "+"and "-" for different c/b of the square coaxial line, where a=10mm and b=9mm.

IV. RESULTS

To verify the accuracy of the formulas derived in this paper, the moment method [15] are used for comparison. As shown in Fig. 5 (a), good agreement can be observed between the results by moment method and synthetic asymptote formula for the per unit length capacitance of square coaxial line. The average error is less than 2% with the maximum error of 2.5%. Moreover, the results by the formula of circular coaxial line are also added in Fig. 5. One can see that the formula of circular coaxial line can be used for the calculation of the per unit length capacitance of the square coaxial line when c/b is very small. However, when c/b increases, the discrepancy becomes larger, which means the formula of circular coaxial line will not be suitable. Figure 5 (b) shows the calculation error of Fig. 5 (a), and it's apparent that the formula derived by synthetic asymptote has a better performance.

As shown in Fig. 6 (a=10mm), the results of the open-ended capacitance of square coaxial line by synthetic asymptote formula and moment method [15] are given for different b/a and c/b. The results by synthetic asymptote formula are of good accuracy comparing with those by moment method. The average error is less than 2% with the maximum error of 6.5%.

In practice, the characteristic impedance and propagation constant are two important parameters for the transmission line, and the comparisons with HFSS are shown in Fig. 7 (a), where the dimensions of the square coaxial line are, respectively, a=10mm, b=8mm, c=6mm with the length l=50mm. One can see that good agreements are achieved with the average error of 2%. The verification of open-ended capacitance is realized by the S_{11} comparisons of the square coaxial line with an open end as illustrated in Figs. 7 (b) and (c) with average error less than 2%.

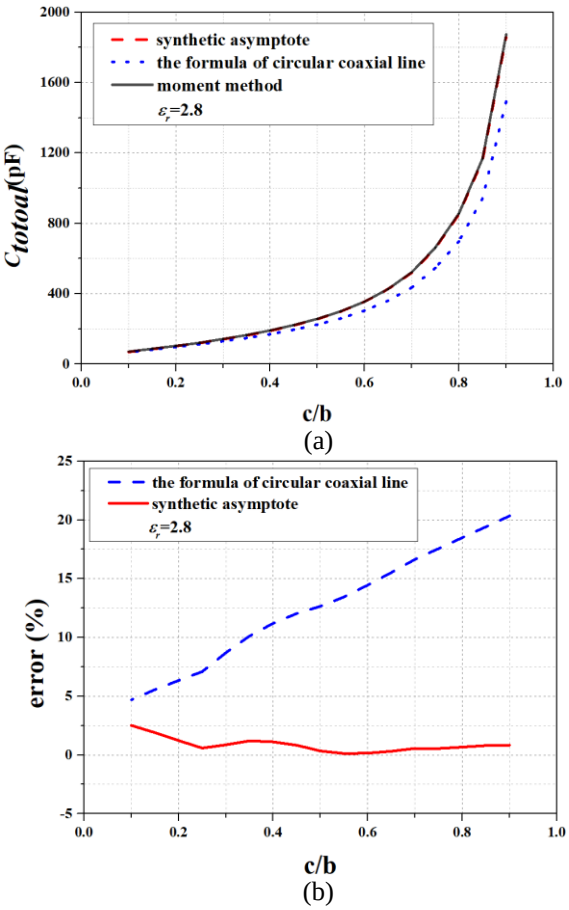

Fig. 5. (a) Comparison of the capacitance C_{total} obtained by the formulas and moment method with ε_r=2.8. (b) The errors of the formula of circular coaxial line and synthetic asymptote, compared with moment method.

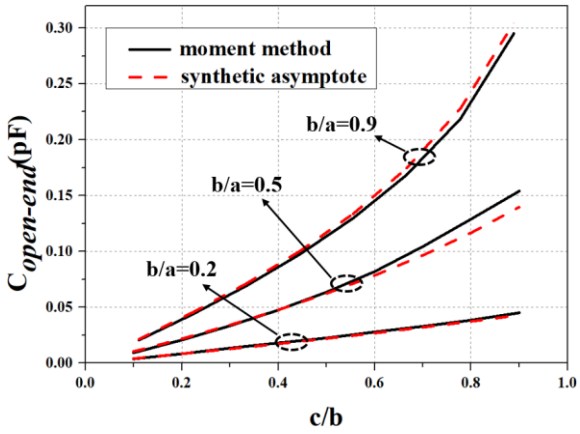

Fig. 6. Comparison of the square coaxial line open-ended capacitance by the synthetic asymptote formulas and moment method, where a=10mm.

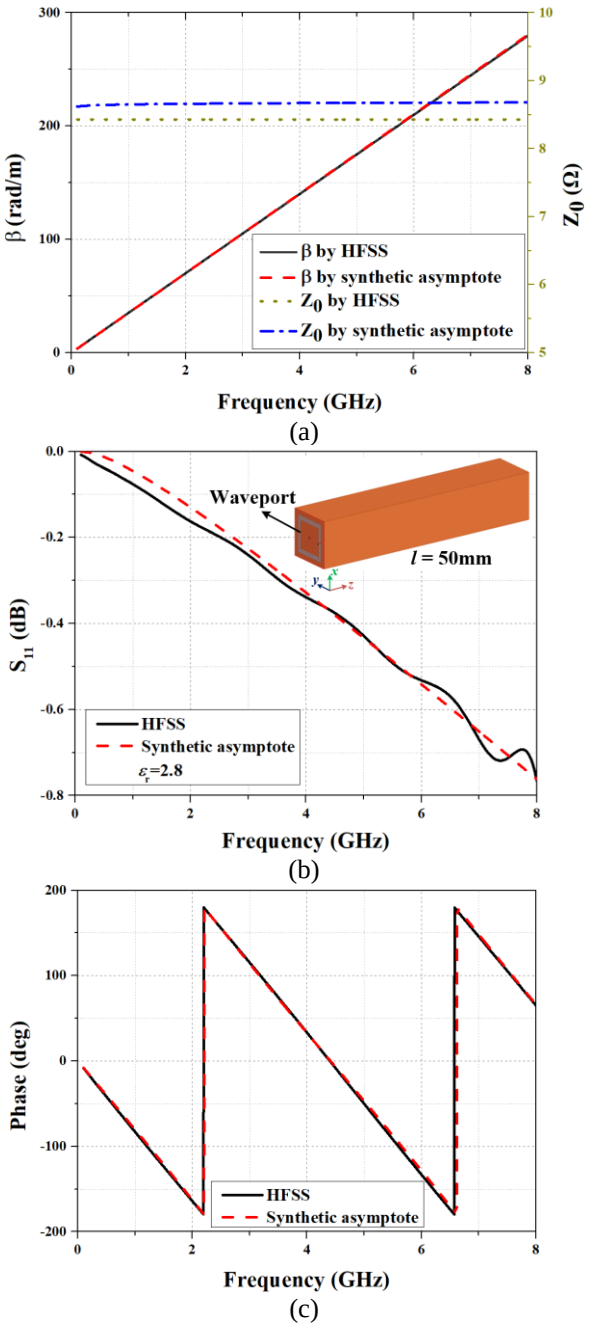

Fig. 7. Comparison of (a) the characteristic impedance and propagation constant, (b) magnitude, and (c) phase of S_{11} of the square coaxial line with an open end.

V. CONCLUSIONS

In this paper, the formulas of characteristic impedance and open-ended capacitance of square coaxial line are derived by synthetic asymptote. All of the formulas are depend on the structure parameters of square coaxial line and have good physical insights. The results of these formulas are compared with numerical methods and good agreement can be found between them.

ACKNOWLEDGMENT

This work is supported by the National Natural Science Foundation of China (Grant No. 61571232) and the Research Innovation Program for College Graduates of Jiangsu Province (Grant No. KYLX16_1291).

REFERENCES

[1] B. A. Munk, *Frequency Selective Surface: Theory and Design*. New York, John Wiley & Sons Inc., 2000.

[2] J. Ginn, B. Lail, D. Shelton, et al., "Characterizing infrared frequency selective surfaces on dispersive media," *Applied Computational Electromagnetics Society Journal*, vol. 22, no. 1, pp. 184-188, 2007.

[3] G. Q. Luo, et al., "Theory and experiment of novel frequency selective surface based on substrate integrated waveguide technology," *IEEE Transactions on Antennas and Propagation*, vol. 53, no. 12, pp. 4035-4043, 2005.

[4] B. Li and Z. Shen, "Three-dimensional dual-polarized frequency selective structure with wide out-of-band rejection," *IEEE Transactions on Antennas and Propagation*, vol. 62, no. 1, pp. 130-137, 2014.

[5] A. A. Omar and Z. Shen, "Multiband high-order band-stop 3-D frequency-selective structures," *IEEE Transactions on Antennas and Propagation*, vol. 64, no. 6, pp. 2217-2226, 2016.

[6] J. Ge, J. Zhu, H. Zhang, W. Zhuang, and W. Tang, "3-D square coaxial waveguide FSS and equivalent circuit model," *Progress in Electromagnetics Research Symposium (PIERS)*, vol. 10, no. 1109, pp. 1110-1114, 2016.

[7] T. S. Chen, "Determination of the capacitance, inductance, and characteristic impedance of rectangular lines," *IRE Transactions on Microwave Theory and Techniques*, vol. 8, no. 5, pp. 510-519, 1960.

[8] H. J. Riblet, "Expansions for the capacitance of a square in a square with a comparison," *IEEE Transactions on Microwave Theory and Techniques*, vol. 44, no. 2, pp. 338-340, 1996.

[9] A. Milovanovic, B. Koprivica, A. Peulic, et al., "Analysis of square coaxial line family," *Applied Computational Electromagnetics Society Journal*, vol. 30, no. 1, pp. 99-108, 2015.

[10] G. B. Gajda and S. S. Stuchly, "Numerical analysis of open-ended coaxial lines," *IEEE Transactions on Microwave Theory and Techniques*, vol. 31, no. 31, pp. 380-384, 1983.

[11] A. Kraszewski and S. S. Stuchly, "Capacitance of open-ended dielectric-filled coaxial lines experimental results," *IEEE transactions on instrumentation and measurement*, vol. 32, no. 4, pp. 517-519,

1983.
[12] Y. L. Chow and W. Tang, "Formulas of microstrip with truncated substrate by synthetic asymptotes—A novel analysis technique," *IEEE Trans. Microwave Theory Tech.*, vol. 49, no. 5, pp. 947-953, 2001.
[13] Y. L. Chow and W. Tang, "Development of CAD formulas of integrated circuit components-fuzzy EM formulation followed by rigorous derivation," *Journal of Electromagnetic Waves and Applications*, vol. 15, no. 8, pp. 1097-1119, 2001.
[14] W. Tang, Z. Yu, and X. Chen, "Synthetic asymptote formulas of asymmetric edge-coupled striplines," *Microwave and Optical Technology Letters*, vol.50, no. 3, pp. 706-708, 2008.
[15] R. F. Harrington and J. L. Harrington, *Field Computation by Moment Methods*. Oxford University Press, 1996.
[16] Ansys Corporation. (2011). High Frequency Structure Simulator (HFSS), Canonsburg, PA, USA. [Online]. Available: http://www.ansys.com/

Jinqun Ge was born in Jiangsu Province, China, in 1993. He received the B.S. degree from Nanjing Normal University, Nanjing, in School of Physics and Technology in 2015. He is currently pursuing the M.S. degree with the School of Physics and Technology, NJNU.

His current research interests include frequency selective surface and CAD of microwave circuits.

Jianping Zhu was born in Anhui Province, China, in 1986. He received the B.S. degree from Anhui University, Hefei, in School of Electronics and Information Engineering in 2010. Currently, he is working towards the Ph.D. degree at Nanjing University of Science and Technology.

His current research interests include RF/microwave circuit, through silicon via and frequency-selective surfaces.

Zhengyong Yu was born in huaian, China, in 1982. He received the B.S. degree in Electronic Information Engineering from the Huaiyin Institute of Technology, Huaian, China, and the M.S. degree in Electromagnetic Field and Microwave Technology from the Nanjing University of Science and Technology, Nanjing, China, in 2006 and 2008, respectively.

He is currently an Associate Professor in Huaian Vocational College of Information Technology and pursuing the Ph.D. degree in Nanjing Normal University. His current research interests include signal integrity and power integrity design in high-speed package and printed circuit boards.

Haiyong Zhang was born in Jiangsu Province, China, in 1993. He received the B.S. degree from Nanjing Normal University, Nanjing, in School of Physics and Technology in 2015. He is currently pursuing the M.S. degree with the School of Physics and Technology, NJNU.

His current research interests include low profile antenna and near-field UHF RFID reader.

Wanchun Tang (M'04) was born in China in 1967. He received the B.S. degree from Tsinghua University, Beijing, China, in 1990, the M.S. degree from the Nanjing University of Science and Technology (NJUST), Nanjing, China, in 1995, and the Ph.D. degree from the City University of Hong Kong, Hong Kong, in 2003, all in Electrical Engineering.

He was a Full Professor with the Department of Communication Engineering, NJUST, and is currently a Specially Invited Full Professor with the Jiangsu Ley Laboratory on Optoelectronic Technology, School of Physics and Technology, Nanjing Normal University, Nanjing. He has authored or coauthored over 100 journal and conference papers. His current research interests include modeling and optimization of RFIC, antennas, signal integrity, and power integrity design in package.